Experiments in Surface Perception using a Fingertip Haptic Display

by
Steven Craig Venema

A thesis submitted in partial fulfillment of the requirements for the degree of

Doctor of Philosophy

University of Washington

1999

Approved by: _____
Chairperson of Supervisory Committee

Program Authorized to Offer Degree: Department of Electrical Engineering

Date: 23 April, 1999

Signature: _____

Date: _____

University of Washington

Abstract

Experiments in Surface Perception using a Fingertip Haptic Display

by Steven Craig Venema

Chairperson of Supervisory Committee: Professor Blake Hannaford
Department of Electrical Engineering

A haptic display provides the mechanical analog of a physical environment for our sense of touch in a virtual reality (VR) simulation system. In this dissertation, we explore the design and implementation of a planar fingertip haptic display (FHD) mechanism. We first present a new technique for analysing the reachable workspace of mechanisms that have stochastic kinematic parameters. This technique is used to develop a stochastic representation of the reachable workspace of the human finger. Using this finger workspace, we present a method for selecting the kinematic parameters of a five-bar linkage mechanism to match the finger workspace while providing high-quality force output capability over the entire mechanism workspace. We then use this haptic display in psychophysical experiments which explore the human perception of geometric surface discontinuities on a haptically rendered virtual surface. Specifically, the experiments examine how the ability to perceive and locate both first-order and second-order surface discontinuities is affected by both the magnitude of the discontinuity and by the particular set of control gains used in haptically rendering the discontinuity. The results of these experiments are relevant to haptic simulation systems which approximate complex curved surfaces with planar facets: the intersection between facets is a form of surface discontinuity and the perceived smoothness of the surface is likely related to the magnitude of the change in surface gradient at these intersections.

TABLE OF CONTENTS

LIST OF FIGURES

LIST OF TABLES

CHAPTER 1: INTRODUCTION

Humans perceive the environment that surrounds them through five sensory channels, popularly labeled ‘‘sight,’’ ‘‘sound,’’ ‘‘taste,’’ ‘‘smell,’’ and ‘‘touch.’’ All of these modalities are fused together in our brains into an apparently seamless perception of our world. A virtual reality (VR) system attempts to ‘‘immerse’’ the user in a simulated environment by providing simulations of one or more these sensory channels. This ability to immerse one’s self in a simulated environment allows a number of interesting applications, including those shown in Table 1.1.

Table 1.1: VR applications

Entertainment	–	Video games, travelogues, etc.
Training	–	Risk-free training for aircraft pilots (or aircraft maintenance workers). Surgical simulations for training medical students
Engineering Design	–	Exploring design alternatives and their effect on manufacturability, maintainability, etc.
Medical Research	–	Drug Design (Molecular Docking)
Scientific Data Analysis	–	Interactive exploration of high-dimensionality datasets

In a typical VR system, a computer program is used to maintain the state of the environment: the locations and velocities of objects in the simulated environment, the location of the user, as well as object-to-object and user-to-object interactions. These states are then presented or rendered to the user via one or more of the five sensory channels in a real-time interactive manner. The primary challenges for VR systems are (1) providing the necessary hardware for presenting rich, realistic ‘‘inputs’’ to one or more of the five sensory channels, and (2) providing the computing power and communications

bandwidth necessary to maintain the states of increasingly complex and realistic simulated environments.

1.1 THE SENSE OF TOUCH

While we typically place the most importance on our visual sense, it is our sense of touch which provides us with much of the information necessary to modify and manipulate the world around us. Physiologically, the sense of touch incorporates two types of information: (1) the sensations of skeletal joint position and forces provided by biological sensors in the muscles and tendons and (2) the sensations of pressure, vibration, temperature, etc. provided over the surface of the body by cutaneous and subcutaneous mechanoreceptors. Both of these sensory inputs are important to our ability to sense and manipulate our surrounding environment, but the relative importance of these types of data is not well understood and has only recently begun to be studied [2].

The words *haptic*, *kinesthetic* and *tactile* are all used in the literature to describe our sense of touch−sometimes with apparently inconsistent usage. Table 1.2 shows the etymology and definitions of these three related words, as defined by the Oxford English Dictionary [1]. While these definitions are quite similar, especially in the case of ‘‘haptic’’ and ‘‘tactile,’’ in this dissertation we will use the word *kinesthetic* to describe sensory information related to joint motion and forces, the word *tactile* to describe skin-

Table 1.2: Words used to describe our sense of touch [1]

Word	Etymology		English Definition
Haptic	Greek	απτικ – Able to come into contact with απτειν –To fasten	Of, pertaining to, or relating to the sense of touch or tactile sensation.
Kinesthetic	Greek	κιν (ειν) – To move αισθησισ – Sensation	The sense of muscular effort that accompanies a voluntary motion of the body.
Tactile	Latin	Tactilis tangible	1. Perceptible to the touch; tangible. 2. Of or pertaining to touch.

surface based sensations, and the word *haptic* to describe the general sense of touch which incorporates both kinesthetic and tactile sensory information.

Both the kinesthetic and tactile portions of the haptic sense have an important distinction relative to the visual and auditory sensory modalities: these latter two modalities are only one-way flows of information from the environment to our sensory apparatus. Specifically, the visual sense involves the collection and analysis of reflected photons generated by existing light sources, while the auditory sense involves the collection and analysis of sound waves from the environment but does not generate significant sounds in this process. In both cases, energy flows in one direction from the environment to the human and thus the visual or aural environment can be recorded and replicated (displayed) by an information system. In contrast, the haptic sense fundamentally involves a *bidirectional* flow of energy between the human and environment. The relevant form of energy here is mechanical energy whose rate of change (power) is determined instantaneously by the product of the contact force and the velocity of the contact point. This energy exchange is most significant for kinesthesia, but is also significant for tactile sensations as we often modify the shape, resonant frequency, temperature, etc. of the objects that we touch even in the most gentle manner.

1.2 HAPTIC VR SIMULATION

For visual VR simulation, an artificial display (e.g., a CRT monitor) is used to present a simulated view the environment for the eye. For a haptic VR simulation, some means must be provided for mechanically generating energetic interactions with a human operator at a variety of locations. One interesting approach for haptic simulation is to have one or more robotic mechanisms which dynamically present small physical pieces of the a full environment to the operator as needed. So, for example, a robot holding a selection of different push-buttons could position a given button in front of the operator’s fingertip to

provide a haptic sensation consistent with some larger-scale haptic (and perhaps visual) model of the environment. This so-called ‘‘robotic graphics’’ approach [3] can present very realistic haptic simulations, but is limited in terms of the environment complexity that can be provided simultaneously.

The more typical approach to haptic simulation is to provide a mechanically actuated device which can interactively move along with some point on the human operator’s body (e.g., the palm of the hand or the fingertip) while impeding motion and/or applying forces as needed to simulate haptic interaction at this human/machine point of contact. This latter approach is also limited in terms of the environment complexity that can be presented simultaneously, but it is by far the more popular approach in current research and commercial applications.

1.3 MODELING HAPTIC INTERACTION

1.3.1 One-Port Haptic Contact Model

The bidirectional nature of haptic interaction implies that an energy flow is present at the point of contact between the human and external environment. The bond-graph method [4] from network theory [5] allows us to model this energetic interaction in terms of a one-port network, using the generalized quantities ‘‘effort’’ and ‘‘flow.’’ This notation, applicable to both electrical and mechanical energy transmission, is very useful when modeling control systems where both forms of energy transmission are present simultaneously. The equivalent variables for both mechanical and electrical systems are shown in Table 1.3. The product of effort and flow is power, which specifies flow of energy across the port.

Table 1.3: Generalized System Variables

Electrical Systems		Generalized System	Mechanical Systems	
Unit	Variables	Variables	Variables	Units
$V = N \cdot m \cdot C^{-1}$	Voltage	Effort	Force	$F = N$
$I = C \cdot s^{-1}$	Current	Flow	Velocity	$V = m \cdot s^{-1}$
$P = N \cdot m \cdot s^{-1}$	Power	Power	Power	$P = N \cdot m \cdot s^{-1}$
$E = N \cdot m$	Energy	Energy	Energy	$E = N \cdot m$

For haptic interaction, the equivalent one-port network is shown on the right side of Figure 1.1 where the power at the port is determined by the force, f_P and the velocity, v_P at the point of contact. Since the energy flow is dependant upon both the human and the external environment, neither side of the port can simultaneously control both variables− in fact, a given side of the port can control only one of the two variables at a given moment. This model suggests two different types of haptic displays: those that control the force being applied to the operator and those that control the velocity of the display. In both cases, the uncontrolled variable is available for the operator to change as a system input.

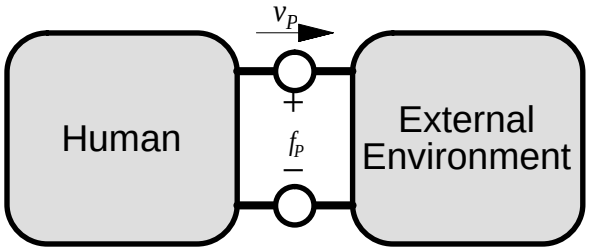

Figure 1.1: One-port network model of haptic contact

1.3.2 Two-port Model of Haptic Simulation

In haptic simulation we wish to simulate the environment side of the contact port shown in Figure 1.1. However, the haptic display system will consist of both a mechanical device and some sort of computer control system−each having its own set of physical constraints which limit the fidelity of the haptic simulation. Figure 1.2 shows a two-port model of a haptic simulation system which includes the haptic device, the computer control system, and a port between them.

The second port represents the interface between the haptic display device and the computer simulation system. Since there is no physical interaction at this port, the port variables, v_D and f_D, are only information flows. One of these two variables is sensed by the simulation system while the other is controlled by it. In Figure 1.2, the velocity, v_D is the sensed variable while the force, f_D is shown as the controlled variable. The converse is also possible with force being sensed and velocity (and position) being controlled. These two modes of control are known as *impedance control* and *admittance control* respectively [6][7][8].

1.3.3 Haptic Simulation Research

Ideally, the haptic display device would exactly reproduce what the computer simulation commanded and feed back perfectly accurate sensor data at all times. However,

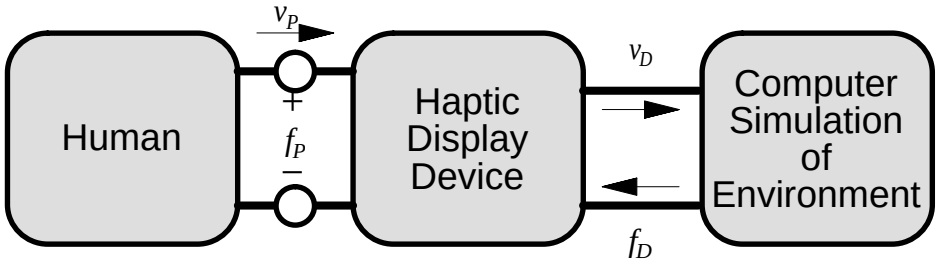

Figure 1.2: Two-port model of haptic simulation system

mechanical limitations of the device such as limited force output, friction, inertia, sensor accuracy limitations, and communications delays will all limit its ability to exactly reproduce these effects. And, since the haptic device is located in series between the human operator and the computer simulation, these limitations may affect the quality of the haptic simulation at the contact port.

The computer simulation may impose further limitations to haptic simulation performance. Typically implemented as a digital control system, it is subject to sampling delays and limitations in available computing power. In addition, the simulated dynamic models of physical interactions are, at best, only approximations of the true complexities of frictional, inertial, and deformation effects present in physical interactions.

Much of haptic simulation research is focused on gaining further understanding of these limitations and attempting to mitigate their effects on the performance of haptic simulation systems. Current research focus areas include:

1. **Dynamic Modeling:** Realistic simulation of physical interactions requires more complex models that include non-linear behaviors such as friction and object shape deformation.
2. **Simulation Computing Architecture:** The desire for more dynamically realistic realtime simulations of increasingly complex environments is motivating the development of novel computing architectures and algorithms .
3. **Haptic Display Devices:** Since the mechanical properties of the haptic display device inherently limit the capabilities of the haptic simulation, improved techniques are needed for optimizing the mechanism design in terms of its mechanical performance and human-machine interface capabilities.
4. **Control Stability**: The physical limitations of the simulation system tend to cause control instabilities for high-performance haptically rendered environments. A

better understanding is needed of the stability properties of haptic display systems and methods of mitigating these instabilities.

5. **Human Haptic Perception:** Human perception limitations impose an upper bound on the necessary performance of haptic simulation systems, since there is no point in haptically rendering an environment to any higher fidelity than the human can perceive. A better understanding of these perceptional limitations is needed to optimize the design and used of haptic simulations systems.

1.4 DISSERTATION OVERVIEW AND GOALS

In this dissertation, we will be considering the development and experimental use of a device for presenting a VR haptic simulation environment to the fingertip, with the goal of exploring some of the research foci listed in the previous section. Specifically, we are interested in developing a fingertip haptic display which is optimized for the reachable workspace of the fingertip and whose form factor allows multiple displays to be used simultaneously for multiple fingers. This display will then be used to perform experiments on the perception of surface features and the effects of control system parameters and feature parameters on the ability to perceive these features.

In Chapter 2, we present a new technique for representing the reachable workspace of mechanisms with stochastic kinematic parameters. This stochastic reachable workspace representation allows a better understanding of how the statistical distribution of these kinematic parameters affects the reachable workspace and allows more informed choices to be made in the design of mechanisms in terms of the suitability of its human-machine interface.

In Chapter 3, we use the stochastic workspace techniques developed in the previous chapter to develop a stochastic reachable workspace representation for the human finger. Anthropometric data from various surveys were used to model the finger as a 3 degree of

freedom planar serial mechanism with stochastically defined link lengths. This model of the finger workspace allows the informed selection of a target reachable workspace in the mechanical design of a fingertip haptic display.

In Chapter 4, we present the design techniques used to optimize the kinematic design of a fingertip haptic display using an extended five-bar planar mechanism. The optimization process searched the kinematic design space (link lengths and joint motion ranges) for the best design according to certain performance criteria while satisfying predefined requirements such as actuator motion ranges.

In Chapter 5, we present the results of experiments which examine the ability of human operators to perceive discontinuities in simple haptically simulated surfaces. The results are important for developing a better understanding of how best to haptically render complex surfaces in terms of minimizing rendering difficulty while maximizing the perceived quality of these surfaces.

Notes to Chapter 1

[1] Oxford English Dictionary, Oxford University Press, 1998.

[2] Lederman, S.J. and R.L. Klatzky, *Designing Haptic Interfaces for Teleoperation and Virtual Environments: Should Spatially Distributed Forces be Displayed to the Fingertip?,* Proceedings ASME Dynamic Systems and Control Division, pp. 11-15, 1997.

[3] Gruenbaum, P.E., W.A. McNeely, H.A. Sowizral, T.L. Overman, and B.W Knutson, *Implementation of Dynamic Robotic Graphics For a Virtual Control Panel*, Presence, Vol. 6(1), pp. 118-126, February, 1997.

[4] Paynter, H.M., *Analysis and Design of Engineering Systems*, MIT Press, Cambridge, 1961.

[5] Chua, L.O., C.A. Desoer, E.S. Kuh, *Linear and Non-linear Circuits*, McGraw-Hill, New York, 1987.

[6] Hogan, N., *Impedance Control: An Approach to Manipulation: Part I - Theory*, Journal of Dynamic Systems, Measurement, and Control, vol. 107, pp. 1-7, 1985.

[7] Hogan, N., *Part II: Impedance Control: An Approach to Manipulation: Implementation*, Journal of Dynamic Systems, Measurement, and Control, vol. 107, pp. 8-16, 1985.

[8] Hogan, N., *Part III: Impedance Control: An Approach to Manipulation: Applications*, Journal of Dynamic Systems, Measurement, and Control, vol. 107, pp. 17-24, 1985.

CHAPTER 2: STOCHASTIC REACHABLE WORKSPACE

2.1 OVERVIEW

Human use of complex tools and machinery has become ubiquitous in our modern environment. From computer keyboards to office desks to the automobiles that we drive, all must be designed to work effectively and safely with the humans for whom they were designed. However, the size and shape of the human body may vary significantly between individuals; to avoid custom design for each operator, it is desirable to accommodate a large number of different people for a given design. Understanding how individual variations impact the design requirements is an important part of the design process for human-operated tools and machinery.

Motivating this work is the development of new mechanisms for haptic displays, which provide the sense of touch in simulated (virtual reality) environments [1]. Typically, the haptic mechanism senses the position of the human operator and applies forces to the operator at some predefined contact point (e.g., the palm of the hand, or the fingertip) based on the operator's interactions with the computer-simulated environment. In order to sense position and apply force, the mechanism must be capable of maintaining contact with the operator during operations; so the mechanism must be capable of sharing the human workspace—or at least some predefined portion of this workspace. An understanding of the human workspace and how it varies across a set of individuals is therefore an important part of the design of haptic mechanisms.

In this chapter, a new method of representing the reachable workspace of a stochastically defined mechanism is presented. No work to our knowledge has addressed the computation of a workspace representative of a population of randomly varying

manipulators−such as the limbs of the human body. This method is applicable to any serial mechanism (redundant or non-redundant) and has direct applications in the design of haptic devices, safety analysis of human-robot systems, and the design of human-robot cooperative systems. As an example, we present a case study applying these techniques to develop a model of the reachable workspace of the human finger, in preparation for the design of a fingertip haptic display.

2.1.1 Anthropocentric Design

In the typical approach to human-centered, or ‘‘anthropocentric’’ design, the relevant anthropometric data is obtained via statistical sampling of the targeted operator population. Models of operators using selected percentile values from the anthropometric data are then used to validate and/or adjust the design. For example, in designing the interior of automobiles, manikins with dimensions of 5th-percentile female and 95th-percentile male have often been used as the statistical extremes that must be accommodated by the design [2]. More recently, animated computer models of humans have begun to be used in the design process. Examples include the SAMMIE system developed at University of Nottingham [3][4] and, more recently, a 3D human model in the IBM/CATIA CAD/CAM system[5].

2.1.2 Reachable Workspace

One important parameter of human-centered, or anthropocentric design is the reachable workspace of the operator. The reachable workspace of a mechanism may be defined as the locus of all points in Cartesian space that may be reached by a given mechanism as determined by its kinematic parameters and joint motion range limits. In the case of a human operator, the reachable workspace defines the region where the operator may be able to physically interact with a device. This concept applies to large scale design tasks like the interior of an automobile as well as smaller scale tasks like the design of hand tools.

If we consider the human operator (or a relevant portion, such as an arm or hand) as a mechanism, then anthropometric data can be used to develop a kinematic model which includes stochastic variables. In this paper, we describe a general technique for mapping a stochastic kinematic model into a stochastic representation of reachable workspace. This stochastic reachable workspace representation can then be used as a tool for workspace design and ergonomics.

2.2 LITERATURE REVIEW

A rigorous definition of workspace was given by Wampler [6] and is shown in Table 2.1. Points in the joint space, S_J, and operational space, S_O are related by the forward and inverse kinematic relations. For a given serial mechanism, methods exist for deriving these kinematic relations [7] although closed form solutions are not possible for all mechanisms. However, there is no known general closed form solution to the problem of mapping the joint workspace, W_J, to the associated reachable workspace, W_R. The remainder of this section reviews some published algorithms for computing the reachable workspace.

Table 2.1: Workspace definitions

Term	Symbol	Definition
Joint Space	S_J	The *n*-dimensional space which spans the set of all possible configurations of a mechanism with *n* joints.
Joint Workspace	W_J	The set of all possible configurations of an *n*-joint mechanism subject to joint motion constraints in the mechanism joint space, S_J.
Operational Space	S_O	The *k*-dimensional Cartesian subspace in which the mechanism tip can move.
Reachable Workspace	W_R	The set of all points in S_O that are images of some point in W_J.

One approach to computing the reachable workspace, W_R, is to discretize the Cartesian operational space, S_O, in the neighborhood of the mechanism and, for each discrete point, compute the corresponding point in joint space using derived inverse kinematic relations for the mechanism. With this ‘‘Direct-IK’’ method, if no solution exists for a particular point, or, if the solution is outside of the mechanism’s joint motion range, then that particular point is marked as being outside of the reachable workspace. An alternative, ‘‘Direct-FK’’ approach is to do the converse: select a set of points in joint workspace, W_J, and compute their Cartesian space mappings using the mechanism’s forward kinematics relations.

Both the Direct-IK and Direct-FK techniques generate a volume of points within the reachable workspace and are often rather computationally intensive, depending on the complexity of the mechanism as well as the granularity by which Cartesian/joint space is discretized. There are several existing publications which describe a variety of approaches to either better understand the structure/shape of W_R or reduce the computational requirements for either general or special case mechanisms. For example, Alameldin, et al. [8] present a variation of the Direct-FK method which extracts points that lie on the boundary of W_R. Rasegar and Perel [9] used Monte Carlo methods to allow a smaller set of points to be used in the Direct-FK method. Other variations on the Direct-FK method may be found in [10] and [11].

Kumar and Waldron [12] published a technique for finding the boundary of W_R using a simulated extension force applied to a model of the mechanism and computing the location of the maximum extension. By choosing a set of different extension forces (equal magnitude with varying directions), a set of points are generated which approximate the boundary surface of W_R. This extension technique applies to general mechanisms, but

does not account for mechanism joint motion limits. Later publications further refine this technique [13][14][15][16].

A recursive method for obtaining a discrete version of W_R for serial mechanisms was introduced by Hansen, et al. [17]. Variations on this technique were later published by Kumar and Patel [18] (general *n*-R serial mechanisms with holes and voids in W_R) and, more recently, by Ebert-Uphoff and Chirikjian [19] for binary manipulators (manipulators with joints that can each have only two positions).

The reachable workspace, W_R may also be represented as a set of continuous swept boundary curves or surfaces. Kwon, et al. [20] introduced this technique for *n*-link planar redundant manipulators (i.e., $n>2$). A very thorough examination of this technique for general *n*-joint mechanism may be found in a Ph.D. dissertation by Korien [21].

2.3 METHODS

All of the above-reviewed techniques generate the reachable workspace, W_R from the joint workspace, W_J using the kinematic parameters, K of the mechanism as shown in Figure 2.1. This workspace is boolean in nature, defining regions (either by boundaries or by discrete values) over the mechanism's operational space, S_O, which are inside of the

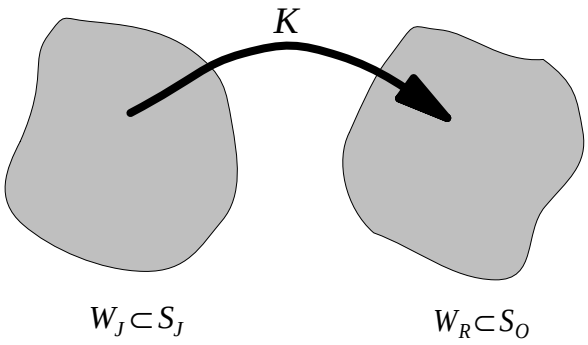

Figure 2.1: Reachable workspace as a mapping from the joint workspace

mechanism's reachable workspace, W_R. However, if any of these kinematic parameters are stochastic—i.e., dependant on one or more random variables with known distributions—then additional work is needed to compute the equivalent stochastic representation of reachable workspace. In the case of human workspace, anthropometric data is usually represented using one or more random variables so that a stochastic representation is needed for reachable workspace.

2.3.1 Stochastic mechanism with one discrete random variable

Let us consider a set of (stochastic) mechanisms whose kinematic parameters are identical except for variations in the geometry of a single component. Let us further assume that there are exactly *m* possible values for the geometry of this part.

We define a discrete random variable, *X*, over the domain of integers with the discrete probability density function,

$$\rho(x) = \sum_{i=1}^{m} P(x_i)\delta(x - x_i) \tag{2.1}$$

where $P(x_i)$ is the probability of the event, $X = x_i$ while $\delta(x - x_i)$ is the Dirac delta function or unit impulse function [22]. We also define the kinematic parameters, *K*, of a given mechanism which will be a function of the random variable, *X*. This stochastically defined mechanism will have m possible sets of kinematic parameters, which we write as $K(x_i)$, and thus m conditional reachable workspaces, one reachable workspace per set of kinematic parameters. Each conditional reachable workspace, $W_R|x_i$, is defined as the set of points in S_O which belong the reachable workspace of the mechanism with kinematics, $K(x_i)$.

For a given point q in S_O, we define $P(q|x_i)$, the probability that q is in the conditional workspace, $W_R|x_i$ as:

$$P(q|x_i) = \begin{cases} 1 & q_i \in W_R|x_i \\ 0 & \text{otherwise} \end{cases} \tag{2.2}$$

Using (2.1) and (2.2), it can be shown [23] that the total probability that the point q is in the stochastic reachable workspace, W_R, is:

$$P(q) = \sum_{i=1}^{m} P(q|x_i)P(x_i) \tag{2.3}$$

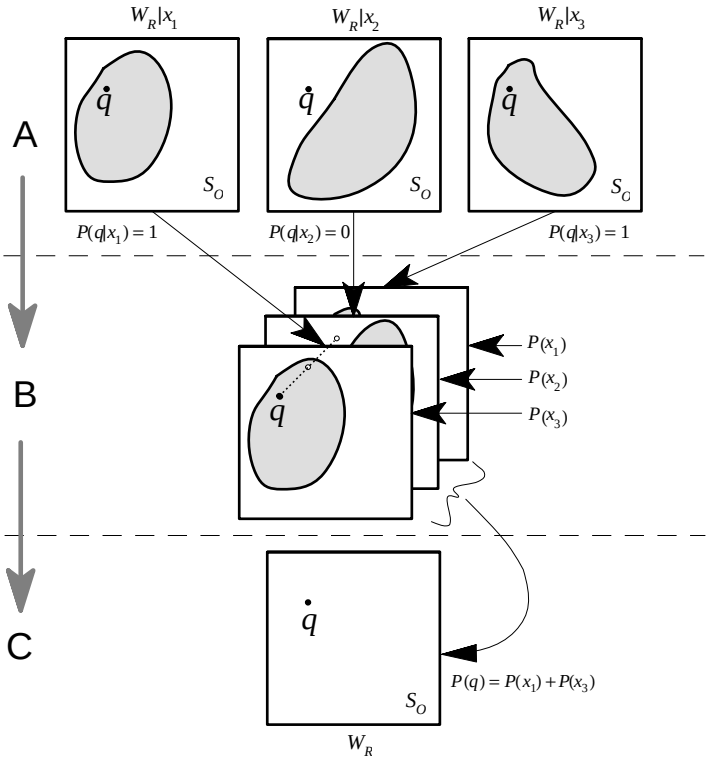

Figure 2.2: Computing the total probability of a point in the operational space of the manipulator

The process for finding $P(q)$ as defined in (2.3) is shown in Figure 2.2 for the case of $m = 3$. In this particular example, the location of the point q is shown as being inside of the conditional workspaces $W_R|x_1$ and $W_R|x_3$ and outside of the conditional workspace $W_R|x_2$−thus generating associated conditional probability values of $P(q|x_1) = P(q|x_3) = 1$ and $P(q|x_2) = 0$ according to (2.2). These three conditional probabilities are multiplied by their respective event probabilities [$P(x_1)$, $P(x_2)$ and $P(x_3)$] and summed together to compute the total probability, $P(q)$ of this point q of being in the reachable workspace of the stochastic mechanism with kinematic parameters, $K(X)$, as defined in (2.3). This process may be repeated for all points q such that the complete stochastic reachable workspace, W_R is found. However, to minimize the amount of computation, it is important to note that the conditional reachable workspaces, $W_R|x_1$, $W_R|x_2$, …, $W_R|x_m$ need only be found once per stochastic mechanism.

Note that the value of $P(q)$ is of the form of a sum of products where each product term is either a 1 or a 0 multiplied by a probability. Since all the probabilities must add to 1, the value of $P(q)$ must be in the range of [0,1]—0 when q is not in *any* of conditional reachable workspaces, and 1 when q is in *all* of them.

2.3.2 Using a continuous random variable

In the previous example, the kinematic parameters depend upon a discrete-valued random variable. We now consider the case of a single continuous random variable whose value is in the range of $(s,t]$ on the set of real numbers, $\Re$. We redefine X as a continuous random variable with some density function, $\rho(x)$, over the range $(s,t]$ as shown in Figure 2.3.

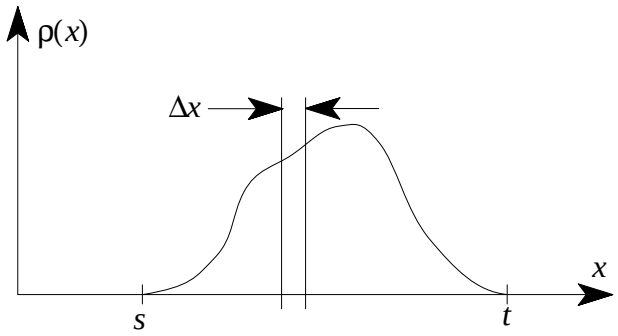

Figure 2.3: Probability density of the continuous random variable

A problem becomes apparent when we change the definition of our random variable, X, from discrete to continuous: the set of possible values of a real number over an interval is an uncountable infinity (i.e., $m \to \infty$) so that an infinite number of stochastic workspaces, $P(q|x_i)$ would be needed in the reformulation of (2.3) for the continuous random variable:

$$P(q) = \int_s^t P(q|x)\rho(x)\mathrm{d}x \tag{2.4}$$

However, if we define a set of mutually exclusive intervals, $<i>$, of width Δx over the domain of X, where the notation, $<i>$ is defined as

$$<i> \leftrightarrow (s+[i-1]\Delta x) < x_i \leq (s+i\Delta x) \tag{2.5}$$

so that

$$m = \frac{t-s}{\Delta x} \tag{2.6}$$

we can approximate the integral in (2.4) as

$$P(q) \cong \sum_{i=1}^{m} P(q|x_i)P(x_i) \tag{2.7}$$

where x_i corresponds to event $<i>$ as defined in (2.5).

From Figure 2.3 and (2.5) we can see that the value for $P(x_i)$ in (2.7) may be computed as

$$P(x_i) = \int_{s+(i-1)\Delta x}^{s+i\Delta x} \rho(x)\mathrm{d}x \tag{2.8}$$

which can be computed in closed form or numerically from the known density function, $\rho(x)$. The conditional probability, $P(q|x_i)$ in (2.7) may be computed as in (2.2) using the median or perhaps the expected value of x_i over the range $<i>$.

Thus with (2.7), we can compute the approximate stochastic reachable workspace of the mechanism with one stochastic random variable affecting the kinematics, $K(x_i)$. The errors introduced by this approximation stem from the fact that $W_R|x_i$ is a step-wise approximation of the continuous case, where $m \to \infty$. However, the magnitude of this error will be directly related to the magnitude of Δx in (2.5); if we assume that a very small step size (Δx) will have a very small effect on the kinematics of the mechanism—and thus a small effect on the conditional reachable workspace, $W_R|x_i$—then, for sufficiently small Δx, an accurate result will be gained at the expense of increased computation requirements due to larger m as related to Δx in (2.6). In the limiting case, as $\Delta X \to 0$, (2.7) is equivalent to the exact integral formulation in (2.4), but at the expense of requiring an infinite number of conditional workspaces to be computed. Therefore, a trade-off between the accuracy of the approximation in (2.7) and the computational requirements is required.

2.3.3 Further Developments

In (2.4)-(2.5) we assume that the density function, $\rho(x)$ has non-zero values only in the range $(s,t]$ which has been divided into m separate regions, $\{<1>, <2>, \ldots, <m>\}$

with each region of equal width, Δx. However, density functions with unbounded range (e.g., Gaussian) are often used. To accommodate these functions, two special events, x_0 and x_{m+1} and their associated regions on the domain of $\rho(x)$ are introduced:

$$\begin{aligned} <0> &\leftrightarrow (-\infty < x_i \le s) \\ <m+1> &\leftrightarrow (t < x_i \le \infty) \end{aligned} \tag{2.9}$$

Thus the set of all events, $\{<0>, <1>, <2>, \ldots, <m>, <m+1>\}$, together span the domain of $\rho(x)$. The values of s and t are chosen so that the area (i.e., probability) of the events x_0 and x_{m+1} are relatively small as shown in Figure 2.3. With this approach, (2.7) is rewritten as

$$P(q) \cong \sum_{i=0}^{m+1} P(q|x_i)P(x_i) \tag{2.10}$$

We can also extend the above analysis to support multiple random variables, say X and Y, with the kinematics, $K(x,y)$ depending on both of these random variables so that (2.4) becomes

$$P(q) = \int_{s_x,s_y}^{t_x,t_y} \int P(q|x,y)\rho(x)\rho(y)\mathrm{d}y\mathrm{d}x \tag{2.11}$$

and the interval notation, $<i>$ in (2.5) becomes

$$<i,j> = \begin{cases} (s_x + [i-1]\Delta x) < x_i \le (s_x + i\Delta x) \\ (s_y + [j-1]\Delta y) < x_j \le (s_y + j\Delta y) \end{cases} \tag{2.12}$$

so that (2.10) may be expressed as

$$P(q) = \sum_{i=0}^{(m_x+1)} \sum_{j=0}^{(m_y+1)} P(q|x_i,y_j)P(x_i,y_j) \tag{2.13}$$

In effect, the above formulation is partitioning the joint domain of the random variables, X and Y into a grid whose elements are sized Δx by Δy and whose probability is computed (as in (2.8)) as

$$P(x_i,y_j) = \int_{s+(i-1)\Delta x}^{s+i\Delta x} \left[\int_{t+(j-1)\Delta y}^{t+j\Delta y} \rho(x,y)\mathrm{d}y \right] \tag{2.14}$$

This two-variable formulation could be extended to even higher ($k>2$) number of variables, but only at the expense of increased computational requirements, which will scale as $O(m^k)$.

2.4 CONCLUSIONS

The reachable workspace of a mechanism is defined as the set of points in its operational space which have corresponding points in the mechanism's joint space, subject to joint motion range limits. Traditionally, the reachable workspace is represented by a boolean function of position in the operational space so that each point q in S_O is either ''inside'' or ''outside'' of the reachable workspace. For mechanisms with unknown but stochastically modeled kinematic properties (e.g., a human population), an extension to this boolean reachable workspace concept has been presented whereby each point q in the operational space, S_O is assigned a value in the range of [0,1] to represent the probability of that point being inside of the reachable workspace. We call this representation of workspace a ''stochastic reachable workspace.''

The stochastic reachable workspace provides an understanding of how stochastically modeled kinematic uncertainties translate into uncertainty in the reachable workspace. This information may be used to improve the design of mechanisms and to improve the design of environments for human use.

Notes to Chapter 2

[1] Hannaford, B.H, and S.C. Venema, *Kinesthetic Displays for Remote and Virtual Environments*, in ‘‘Virtual Environments and Advanced Interface Design,’’ W. Barfield and T. Furness III, Eds., Oxford University Press, 1995.

[2] Roebuck, J.A., *Anthropometric Methods: Designing to Fit the Human Body*, Human Factors and Ergonomics Society, Santa Monica, CA, 1995.

[3] Case, K. and M. Porter, *SAMMIE can cut out the prototypes in ergonomic design*, Control and Instrumentation, vol. 12, no. 1, pp. 28-29, January, 1980.

[4] Kingsley, E.C., N.A. Schofield, and K. Case, *SAMMIE: A Computer Aid for Man Machine Modelling*, Computer Graphics, vol. 15, no. 3, pp. 163-169, August, 1981.

[5] Kayis, B. and P.A. Iskander, *A three-dimensional human model for the IBM/CATIA system*, Applied Ergonomics, vol. 25, no. 6, pp. 395-397, 1994.

[6] Wampler, C.W., *Winding Number Analysis of Invertible Workspaces for Redundant Manipulators*, Proceedings of the 28th Conference on Decision and Control, Vol. 1, pp. 546-569, Los Angeles, CA, USA, December, 1987.

[7] Craig, J..J., *Introduction to Robotics Mechanics and Control*, 2nd Edition, Addison-Wesley, Reading Massachusetts, 1989.

[8] Alameldin, T., N. Badler, and T. Sobh, *An Adaptive and Efficient System for Computing the 3-D Reachable Workspace*, Proceedings of the IEEE International Conference of System Engineering, pp. 503-506, Pittsburgh, PA, USA, August, 1990.

[9] Rastegar, J. and D. Perel, *Generation of Manipulator Workspace Boundary Geometry Using the Monte Carlo Method and Interactive Computer Graphics*, Transactions of the ASME, vol. 112, pp. 452-454, September, 1990.

[10] Tsai, Y.C.and A.H. Soni, *An Algorithm for the Workspace of a General n-R Robot*, Transactions of the ASME, vol, 105, p. 52-57, March, 1983.

[11] Yang, D.C.H. and T.W. Lee, *On the Workspace of Mechanical Manipulators*, Transactions of the ASME, vol. 105, pp. 62-69, March 1983.

[12] Kumar, A., and K.J. Waldron, *The Workspaces of a Mechanical Manipulator*, J. of Mechanical Design, vol. 103, pp. 665-672, July, 1981.

[13] Derby, S., *The Maximum Reach of a Revolute Jointed Manipulator*, Mechanism and Machine Theory, vol. 16, no. 3, pp. 255-261, 1981.

[14] Selfridge, R.G., *The Reachable Workarea of a Manipulator*, Mechanism and machine Theory, vol, 18, no. 2, pp. 131-137, 1983.

[15] Sugimoto, K. and J. Duffy, *Determination of Extreme Distances of a Robot Hand—Part 1: A General Theory*, Journal of Mechanical Design, vol. 103, pp. 631-636, July 1981.

[16] Sugimoto, K. and J. Duffy, *Determination of Extreme Distances of a Robot Hand—Part 2: Robot Arms with Special Geometry*, Journal of Mechanical Design, vol. 103, pp. 776-783, July 1981.

[17] Hansen, J.A., K.C. Gupta and S.M.K. Kazerounian, *Generation and Evaluation of the Workspace of a Manipulator*, International Journal of Robotics Research, vol. 2, no. 3, pp. 22-31, Autumn, 1983.

[18] Kumar, A. and M.S. Patel, *Mapping the Manipulator Workspace Using Interactive Computer Graphics*, International Journal of Robotics Research, vol, 5, no. 2, pp. 122-130, Summer, 1986.

[19] Ebert-Uphoff, E. and G.S. Chirikjian, *Efficient Workspace Generation for Binary Manipulators with Many Actuators*, Journal of Robotic Systems, vol. 12, no. 6, pp. 383-400, 1995.

[20] Kwan, S.J, Y. Youm, and W.K. Chung, *General Algorithm for Automatic Generation of the Workspace for n-link Planar Redundant Manipulators*, Journal of Mechanical Design, vol. 116, pp. 967-969, September, 1994.

[21] Korien, J.U, *A Geometric Investigation of Reach*, Ph.D Dissertation, Department of Computer Science, University of Pennsylvania, 1984. (Republished under the same title by MIT Press, Cambridge, MA, 1984, ISBN 0-262-11104-7).

[22] Kreyszig, E., *Advanced Engineering Mathematics*, 6th Ed., John Wiley & Sons, Inc., p. 266, 1988.

[23] Peebles, P.Z.Jr., *Probability, Random Variables, and Random Signal Principles*, 3rd Ed., McGraw-Hill, New York, NY, 1993.

CHAPTER 3: REACHABLE WORKSPACE OF THE HUMAN FINGER

The previous section details a general method for computing a stochastic representation of reachable workspace for mechanisms with one or more kinematic parameters modeled as stochastic variables. We now apply this technique to compute the reachable workspace of the human finger within the finger flexion/extension plane of motion.

3.1 FINGER KINEMATIC MODEL

Each of the four human fingers have 3 joints, called Metacarpophalangeal (MCP), Proximal-Interphalangeal (PIP), and Distal Interphalangeal (DIP) joints which connect the finger segments (phalages). For this case study, we will limit consideration to only the planar motions of flexion/extension of the finger, ignoring the adduction/abduction and motions of the MCP joints. The skeletal structure and a kinematic model of the finger for flexion/extension motions is shown in Figure 3.1. This kinematic model contains three variables, $(\theta_1,\theta_2,\theta_3)$, three link length parameters (l_1,l_2,l_3) which correspond to the

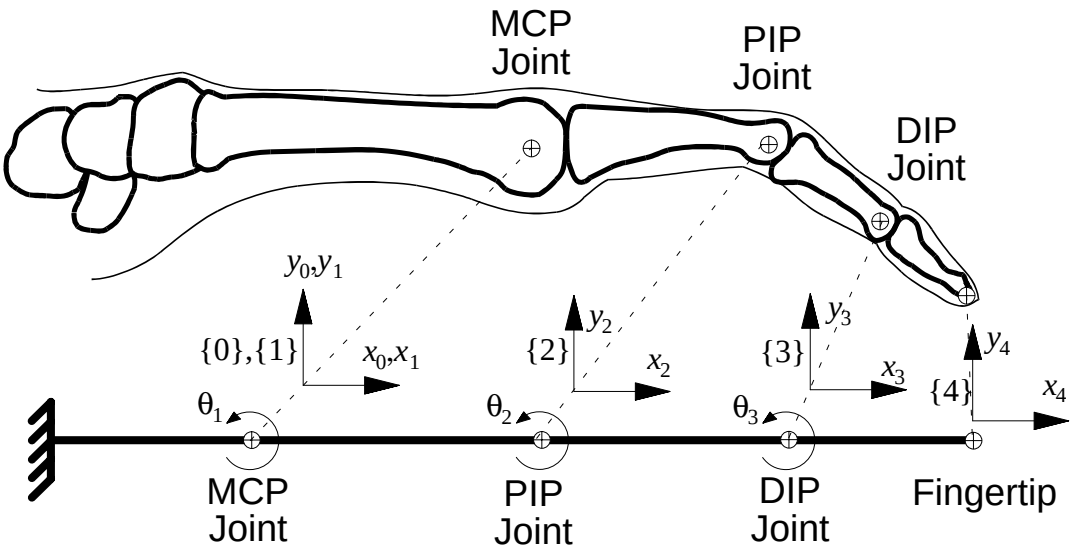

Figure 3.1: Planar skeletal model of the human finger (adapted from [2])

distances between adjacent pairs of link frames, and 6 joint motion limits (a maximum and minimum pair for each joint variable).

3.2 FINGER ANTHROPOMETRY

The identification of kinematic parameters is hampered by the lack of externally visible markers for accurately determining the axes of rotation and link lengths. Only a few existing publications have relevant anthropomorphic data for determining the distribution of finger sizes among the human population. Garret [1] published a 1971 report containing anthropometric data on US Air Force personnel to be used in designing Air Force equipment and manual work areas. The data included measurements of hand length, as defined by the distance between the distal wrist crease to the tip of the middle finger. Table 3.1 shows the published hand length data.

Table 3.1: Garrett [1] Hand Length Data

Hand Length (mm)	Gender	Ranking
165	F	5th percentile
171	F	$\mu - 1\sigma$
179	F	μ
183	M	5th percentile
188	M F	$\mu - 1\sigma$ $\mu + 1\sigma$
193	F	95th percentile
197	M	μ
207	M	$\mu + 1\sigma$
212	M	95th percentile

Unfortunately, no mention is given of the actual distribution of the measured hand length nor is the number of samples given. If we assume that the data for each gender follows a Gaussian distribution, then hand length can be modeled as random variable, *H*, with two defined conditional Gaussian probability distributions,

$$P\{H \le h|M\} = G(197, 9.5) \tag{3.1}$$

$$P\{H \le h|F\} = G(179, 8.5) \tag{3.2}$$

where $G(\mu,\sigma)$ denotes a Gaussian random variable with mean μ and variance σ^2. If we assume that the population is evenly divided by gender then the combined or total probability distribution of H will be

$$\begin{aligned} P\{H \le h\} &= P\{H \le h|M\}P\{M\} + P\{H \le h|F\}P\{F\} \\ &= 0.5 \times [G(197, 9.5) + G(179, 8.5)] \end{aligned} \tag{3.3}$$

Using the definition of the Gaussian distribution, the probability density function, $p(H)$ for the distribution in (3.3) may be expressed as:

$$p(H) = \frac{\exp\left[\dfrac{(h-197)^2}{-2(9.5)^2}\right]}{2\sqrt{2\pi(9.5)^2}} + \frac{\exp\left[\dfrac{(h-179)^2}{-2(8.5)^2}\right]}{2\sqrt{2\pi(8.5)^2}} \tag{3.4}$$

A plot of the probability distribution and probability density of H is shown in Figure 3.2.

Buchholz, et al. [2] published an anthropometric study of the kinematics of the human hand in 1992, using a set of 6 human cadaver hands of a ‘‘broad spectrum of hand sizes’’ to accurately identify the kinematic parameters of fingers of these hands and develop a linear predictive model of finger phalage length from hand length as defined and

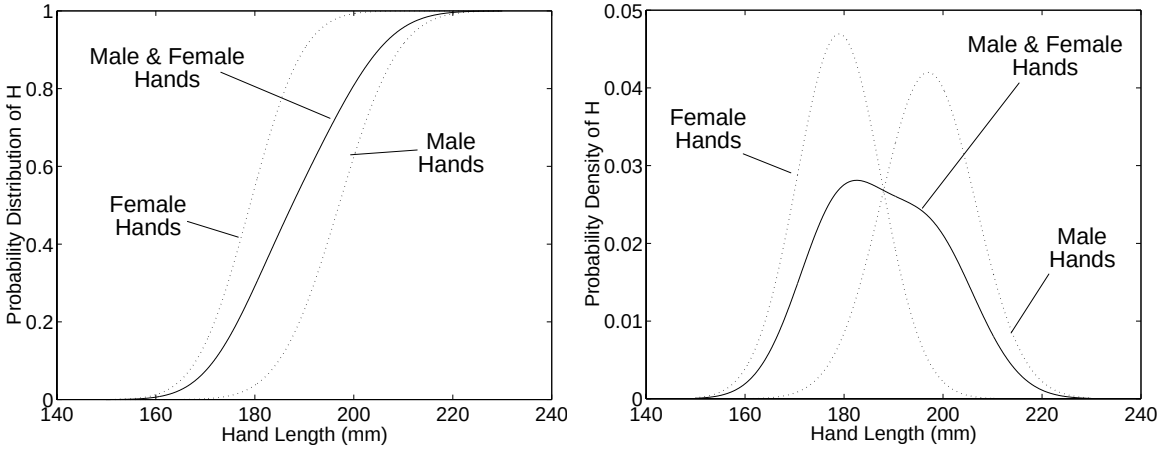

Figure 3.2: Probability distribution and density of hand length (derived from [1])

Table 3.2: Linear Model of Finger Link Length using Hand Length

Finger		Proximal Phalanx		Middle Phalanx		Distal Phalanx	
Name	#	Coeff	Error	Coeff	Error	Coeff	Error
First	1	0.245	0.001	0.143	0.003	0.097	0.002
Middle	2	0.266	0.003	0.170	0.003	0.108	0.003
Ring	3	0.244	0.003	0.165	0.002	0.107	0.004
Little	4	0.204	0.002	0.117	0.002	0.093	0.003

published in Garrett [1] above. The coefficients and standard errors of these models are given in Table 3.2. We can use this data to estimate the link lengths of our kinematic finger model from the hand length which was defined as a random variable, H in (3.3) whose probability distribution is shown in Figure 3.2. So, for example, the link lengths of finger 1 (index finger) of a male with average hand length would be:

$$[l_1, l_2, l_3] = 197\text{mm} \times [0.245\ 0.143\ 0.097]$$
$$= [48.3\ 28.2\ 19.1]\text{mm} \tag{3.5}$$

Unfortunately, no similarly detailed anthropometric study has been published on finger joint motion ranges. Some limited data is available in the medical literature as shown in Table 3.3. For the purposes of this case study, the approximate extreme motion ranges of the author's own fingers were used to compute the reachable workspace. The motions ranges, as defined by the coordinate systems introduced in Figure 3.1, are shown in Table 3.4

Table 3.3: Published Finger Joint Motion Data

Source	Joint Motion Range					
	MCP Joint		PIP Joint		DIP Joint	
	Min.	Max.	Min.	Max.	Min.	Max
American Academy of Orthopaedic Surgeons [3]	-90°	45°	0°	100°	-90°	10°
American Medical Association [4]	-90°	20°	0°	100°	-70°	30°
Occupational Therapy: Practice Skills for Physical Dysfunction [5]	-90°	15° to 45°	0°	110°	-80°	N.A.

Table 3.4: Finger Joint Motion Ranges

Finger Joint	Angular Motion Range
MIP	$-90° \le \theta_1 \le 45°$
PIP	$-120° \le \theta_2 \le 0°$
DIP	$-90° \le \theta_3 \le 50°$

3.3 REACHABLE WORKSPACE FOR KNOWN KINEMATICS

The method of computing the stochastic reachable workspace for the finger requires many individual reachable workspaces to be computed, one for each of the *m* conditional workspaces as detailed in *(2.8)*. A variation on the recursive swept boundary method [21] was chosen for its efficiency. The reachable workspace of an arbitrary planar-revolute 3-DOF mechanism with links {L1,L2,L3} driven respectively by joints {J1,J2,J3} is computed using the following steps:

1. First the reachable workspace of the sub-mechanism comprised only of the outer-most link (L3) is computed relative to the tip of the previous (L2) link as shown in-Figure 3.3A. The reachable workspace of link L3 is the locus of all points on an arc, as bounded by the motion range of the joint J3.
2. Since the ‘‘base’’ of L3 is the ‘‘tip’’ of L2, the reachable workspace of the combined L2/L3 sub-mechanism may be found by sweeping the reachable workspace of the L3 link through the range of motion of link L2 (shown as a dashed arc in Figure 3.3A). As the solid-line arc is swept along the dotted-line arc, the solid-line arc will have a continuous variety of positions, some of which are shown in Figure 3.3B. The sweeping of this arc forms a region whose boundary we would like to extract.

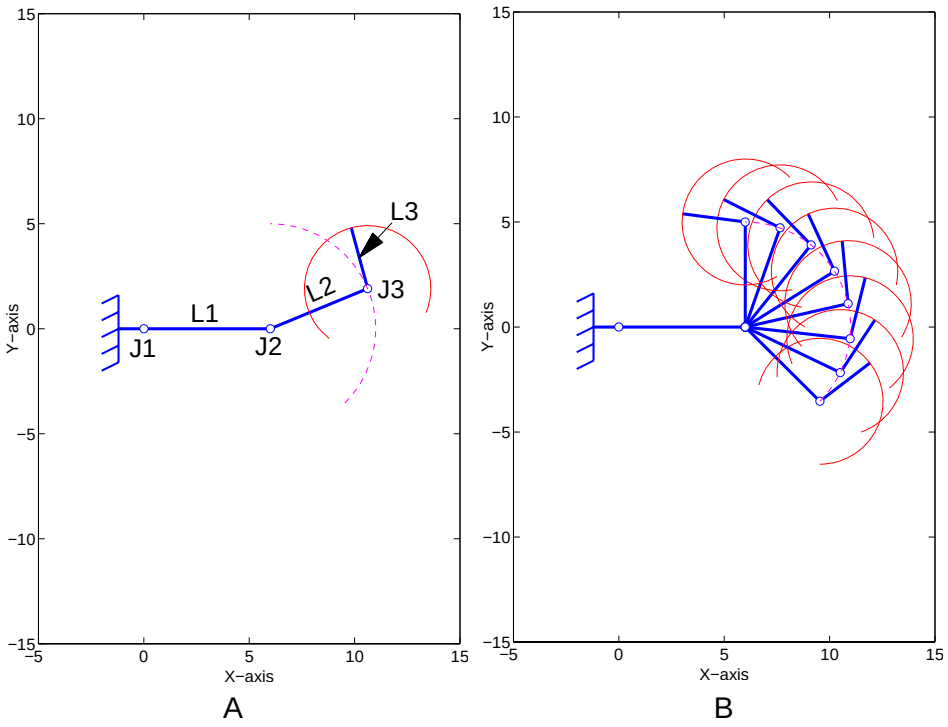

Figure 3.3: Swept workspace of two outermost links of a 3-DOF mechanism

3. The boundary of the swept region shown in Figure 3.3B may be found using the four special ‘‘arc-generating’’ points identified in Figure 3.4A: two points where J3 is at the 0° and 180° positions and two points where J3 is at its joint limits. When swept in an arc-shaped path by the motion of J2, as shown in Figure 3.4B, these four points form a set of arcs which are portions of the reachable workspace boundary. Note that either or both of the 0° and 180° points may not exist for a particular mechanism, depending on the range of motion of J3. The swept paths of these four points are the dashed-lines in Figure 3.4C. The combination of these newly generated arcs, along with the L3 workspace arcs at the two extreme values of the L2 motion range (shown as solid arcs in Figure 3.4C), will bound the resulting reachable workspace region. By tracing the outermost boundary of these arcs, the reachable workspace boundary of the L2/L3 sub-mechanism may be found, as shown in Figure 3.4D.

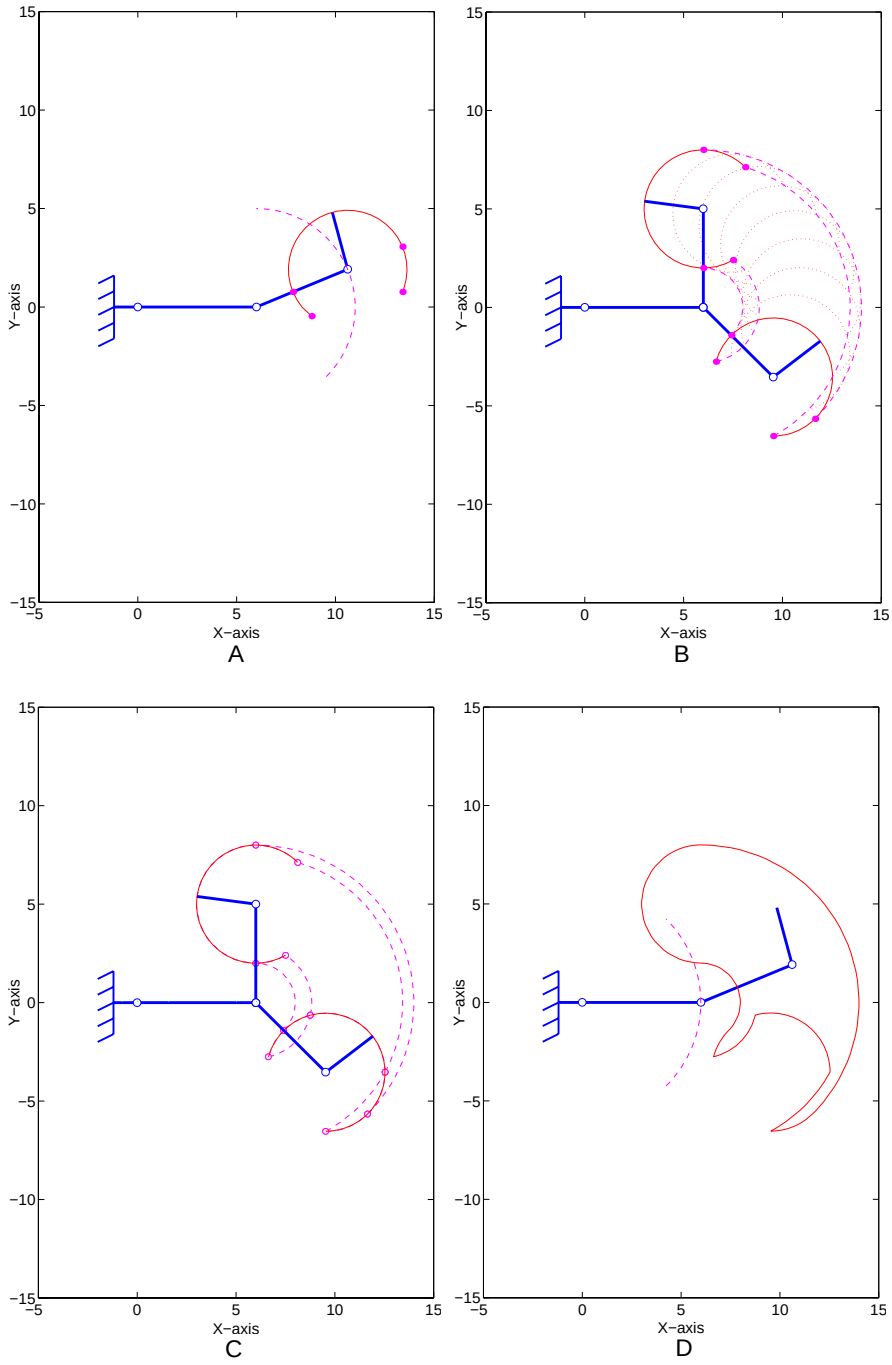

Figure 3.4: 2-DOF Swept workspace computation

4. The reachable workspace of the L2/L3 sub-mechanism is itself swept through the motion range of the L1 link in a fashon similar to that shown in Figure 3.4, with each arc having its own set of two to four arc-generating‘‘ points. By tracing the

outer boundary of these arcs, the resulting reachable workspace for the entire 3-joint mechanism may found.

The method described above may be used to compute the reachable workspace of a human finger with given kinematics. For the case of an male index finger with average dimensions [see equation (3.5)] and assuming a reasonable set of joint motion ranges (see Table 3.4), the reachable workspace will be as shown in Figure 3.5.

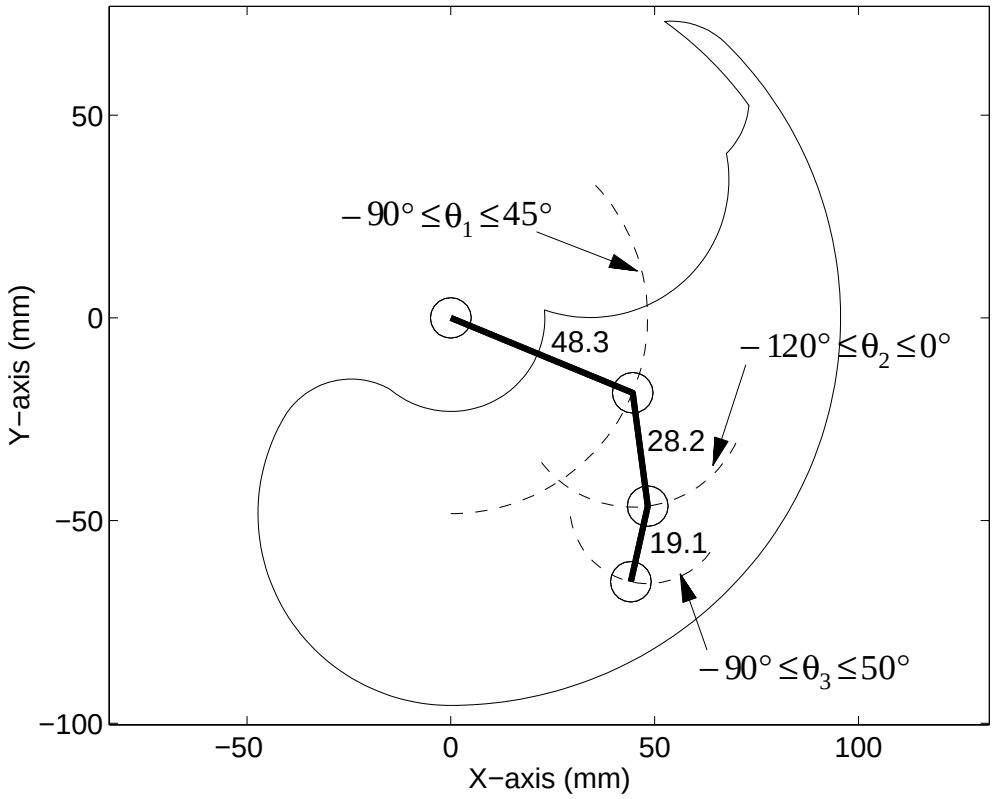

Figure 3.5: Reachable Workspace of an average male's index finger

3.4 STOCHASTIC REACHABLE WORKSPACE

Since we are assuming constant joint motion ranges as defined in Table 3.4, the three kinematic variables of a given finger are the link lengths, $\{l_1,l_2,l_3\}$, as defined in Figure 3.1. Using the Buchholz data [2], these link lengths only depend on hand length, as defined by Garrett [1]; this length may be represented by a continuous random

variable, X whose probability density, $\rho(X)$, is given in (3.4) and shown graphically in Figure 3.2.

Before computing the stochastic reachable workspace, the values of some additional parameters must be selected. First, the bounds of our region of interest for X, $(s,t]$, must be chosen. By inspection of Figure 3.2B, we may see that the probability density is significantly greater than zero only in the range of the 140-240 mm. Thus, the values of

$$s = 140\text{mm}$$
$$t = 240\text{mm} \tag{3.6}$$

may be used to bound the range of our step-wise integration process, as defined by *(2.5)-(2.8)*. The value of Δx affects the accuracy of our approximation *(2.7)* of the exact solution represented by the integral formulation shown in *(2.4)*. The value,

$$\Delta x = 2\text{mm} \tag{3.7}$$

was chosen empirically as a balance between the accuracy of the result and the computational requirements. For the discrete representation of the operational space a sample spacing along both the x and y axes of S_O must be chosen. The choice of this value must be chosen to balance the computational requirements against the desire for an accurate representation of features of each conditional reachable workspace. A value of 4mm was chosen for this case study.

Using these definitions, the conditional workspace may be computed from

$$m = \frac{t-s}{\Delta x} + 2 \tag{3.8}$$

conditional workspaces, $W_R|x_i$ using (3.8).

3.5 RESULTS

Figure 3.6 shows the stochastic reachable workspace, W_R for the index finger. The left plot has values between 0 and 1 for each point q in the operational space, S_O with coordinates (x, y), indicating the probability that q is in the reachable workspace of the stochastic mechanism (the human index finger, in this case). The right plot shows contours of constant probability for probability values, $P(x, y)$ = {0.99, 0.95, 0.90, 0.75, 0.50, 0.20, 0.10, 0.05, 0.01}.

These contours may be used as an aid in designing to accommodate a variety of users. For example the 0.99 contour (the smallest contour in Figure 3.6) bounds the set of points in the operational space which are reachable by 99% of human adult index fingers. Placement of a control button, for example, within this region relative to the MCP joint would insure that the button would be reachable by most (99%) of the population.

When designing haptic devices, the contour data in Figure 3.6 is used somewhat differently. In this case, we wish to insure that the mechanism can track the human operator over the entire motion range. So if we were to design a haptic device for the human index finger, we would want that device to address the reachable workspace of all but a small

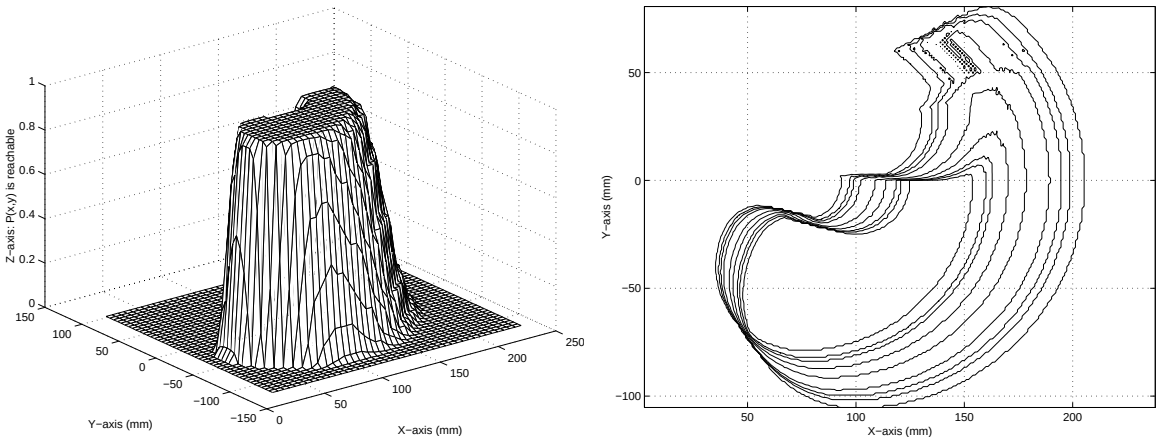

Figure 3.6: Stochastic reachable workspace for the human index finger

number of people, say 0.01%, as bounded in the 0.01 (largest) contour in Figure 3.6. In this way the 0.01% contour accommodates the reachable workspace of $(1-0.01)=99\%$ of the human population. These accommodation contours of $1-P(x,y)$ are shown for each of the four fingers in Figure 3.7 for values of 0.90, 0.95, 0.99 and 0.999 which represent 90%, 95%, 99% and 99.9% respectively of the population.

3.6 CONCLUSIONS

The stochastic reachable workspace provides an understanding of how stochastically modeled kinematic uncertainties translate into uncertainty in the reachable workspace.

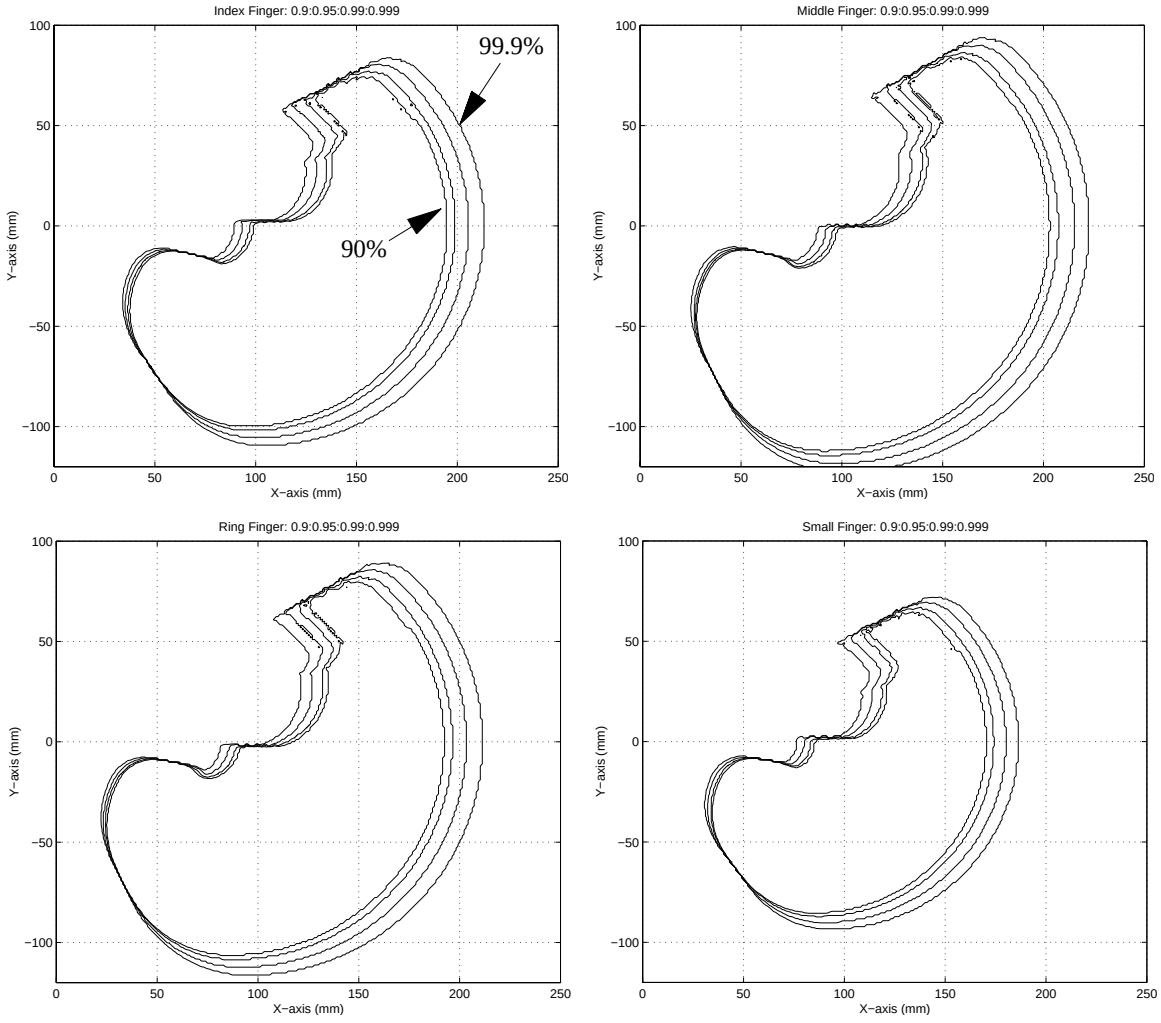

Figure 3.7: Reachable workspace contours for each of the four human fingers.

This information may be used to improve the design of mechanisms and to improve the design of environments for human use. The results of this case study on the stochastic reachable workspace of the human fingers (flexion/extension planar motions) will be used in the development of a haptic display mechanism for the human fingertip.

Notes to Chapter 3

[1] Garrett, J.W., *The Adult Human Hand: Some Anthropometric and Biomechanical Considerations,* Human factors, Vol. 13, No. 2, pp. 117-131, 1971.

[2] Buchholz, B., T.J. Armstrong, and S.A. Goldstein, *Anthropometric data for describing the kinematics of the human hand,* Ergonomics, vol. 35, no. 3, pp. 261-273, 1992

[3] American Academy of Orthopaedic Surgeons, *Joint Motion: Methods of Measuring and Recording*, American Academy of Orthopaedic Surgeons, Chicago, 1965.

[4] American Medical Association, *Guides to the Evaluation of Permanent Impairment*, ed. 3, American Medical Association, Chicago, 1988.

[5] Pedretti, L.W., Zoltan, B., *Occupational Therapy: Practice Skills for Physical Dysfunction*, ed. 3, C.V Mosby Co., St. Louis, 1990.

[6] Korien, J.U, *A Geometric Investigation of Reach*, Ph.D Dissertation, Department of Computer Science, University of Pennsylvania, 1984. (Republished under the same title by MIT Press, Cambridge, MA, 1984, ISBN 0-262-11104-7).

CHAPTER 4: OPTIMIZED KINEMATIC DESIGN OF THE FHD

4.1 HAPTIC DISPLAY REQUIREMENTS

In haptic simulation, a human operator interacts mechanically with an actuated haptic device which is driven by a computer−controlled virtual reality (VR) simulation. Sensors and actuators on the haptic display allow the VR simulation software to measure and respond realistically to human interaction with the virtual environment.

Haptic interaction involves the exchange of mechanical energy between operator and haptic display [1]; the display must be capable of maintaining contact with the human operator at some preselected point of contact (the ‘‘haptic interface’’) while the operator moves through space. For example, in the case of a fingertip haptic interface, the device must be capable of tracking movements of the finger joints, and perhaps the wrist and arm joints as well, depending on how the haptic device is mounted relative to the human operator.

The haptic display must be capable of emulating the environment side of the human-environment haptic interaction for a wide range of simulated objects. However, the physical limitations of the haptic device (non-zero mass, non-infinite stiffness, non-zero friction, actuator saturation, etc.) will cause the device to distort the desired haptic interaction−especially under extreme conditions such as ‘‘free motion’’ (operator motion with no contact forces) and ‘‘hard contact’’ (operator force with no motion while in contact with a rigid virtual object). These non-ideal effects may be minimized through careful design, but ultimately the designer is forced to trade off one limitation against another For example, low mass is desirable for low inertia, but higher mass is needed to stiffen a structure. Overall, minimizing the size of the haptic device will help reduce the effect of

many of these physical limitations. These general design requirements form the basis of optimizing the design.

4.2 UW FINGERTIP HAPTIC DISPLAY

The development of a new fingertip haptic display (FHD) was motivated by our interest in exploring multi-finger haptic interaction, especially as it relates to human perception of surface shapes and features. These goals were translated into the following functional requirements:

- Provide haptic feedback to the human fingertip.
- Allow planar fingertip motion due to flexion and extension motion of the finger joints.
- Have a mechanical form factor that allows multiple FHD's to be used simultaneously−one for each of the four fingers of the hand.

A conceptual design showing four FHD's together is shown in Figure 4.1. The remainder of this chapter describes the optimization methods by which values were chosen for the various kinematic parameters (link lengths and joint motion ranges) of the FHD mechanism to obtain a final design.

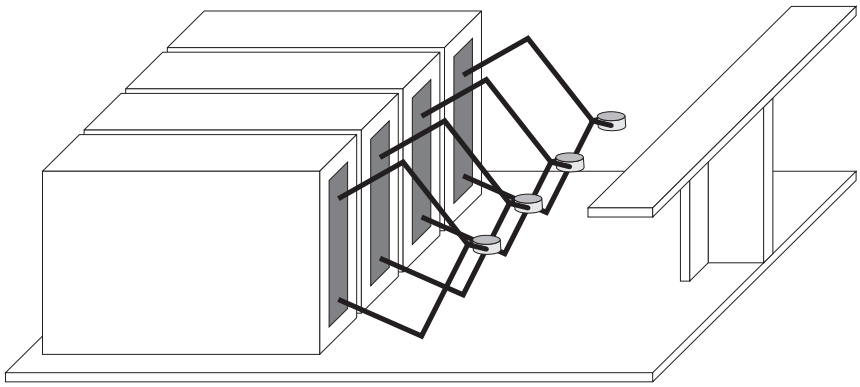

Figure 4.1: Conceptual diagram of multiple FHD's for multiple fingers.

4.3 PREVIOUS WORK

Techniques for haptic mechanism design are drawn primarily from methodologies developed for the design of robotic mechanisms. Formal models of mechanism kinematics

and dynamics have been available for many years (c.f. [3] and [4]). However, the design process is often less well defined. For example, the size and topology of mechanism reachable workspace is usually an important part of the design process, but closed-form expressions of these properties are often difficult to obtain and more general design goals must suffice [5]-[10].

Haptic devices are basically robotic mechanisms with a special set of design requirements. Previous haptic displays for the finger include those which apply separate forces to each segment of the finger such as JPL Dextrous Hand Master [11] as well as those which apply forces to the finger through a tool, such as the UW Pen-Based Force Display [12], Iwata's 6-DOF pen-based display [13], and Immersion's Force Feedback Mouse [14]. Other displays are designed to apply forces to only the fingertip, such as the Sens-Able Technologies' PHANToM [15].

A pneumatic multifinger haptic display has been developed by Burdea, et al. [2] which contains linear actuators connected between the palm of the hand and the tips of each of 3 fingers and a thumb for haptically simulating grasped objects. In its latest configuration, the device has one actuated and two measured degrees of freedom per finger, so that only the distance of the fingertip from the palm of the hand can be controlled while the actual position of the fingertip can be computed.

The performance of a haptic display may be broken down into three categories: kinematic properties such as workspace size, dexterity properties based on the mechanism Jacobian matrix [3], and dynamic properties such as inertia, friction, flexion, and resonant modes.

Kurtz and Hayward [16] presented the dexterity-based optimization of a parallel, actuator-redundant spherical mechanism as a mechanical analog of the human shoulder joint. The optimization was based on three objectives (highest priority first): {1} global

kinematic dexterity (average over the workspace of the ratio of $\sigma_{min}/\sigma_{max}$; {2} maximizing the minimum singular value over the workspace; and {3} maximizing the uniformity of objectives {1} and {2} over the workspace.

Hayward, et al. [17] developed a planar fivebar haptic mechanism called the ‘‘Pantograph’’ using the inertia tensor of the mechanism as the foundation of a multi-objective search that considered inertia as well as dynamic dexterity and dynamic manipulability [4].

Kircanski [18] introduced a methodology by which isotropic configurations of the mechanism Jacobian matrix for 2, 3 and 4-DOF serial planar manipulators as well as a particular 3-DOF spatial manipulator could be identified analytically as a function of joint coordinates and link length ratios.

Stocco, et al. [19] introduced a ‘‘global isotropy index’’ (GII) which is the ratio of $\min_W\{\sigma_{min}\}$and $\max_W\{\sigma_{max}\}$ where W is the mechanism workspace and σ represents the singular values of the mechanism Jacobian or Inertia tensors. They also introduced an efficient culling algorithm for searching the design space.

Lee, et al. [20] used a composite kinematic design index to optimize the design of an anthropomorphic robot arm by combining measures of workspace area, Jacobian isotropy, force transmission ratio, as well as gradients of the latter two measures within the workspace.

4.4 METHODS

4.4.1 FHD Design Constraints

In order to meet the functional requirements listed in Sections 4.1 and 4.2, we first need an understanding of the workspace requirements of the human finger. In Chapter 3 we developed a technique for computing the reachable workspace of a mechanism defined by one or more stochastic kinematic parameters. A case study of the human finger as a 3-DOF planar-revolute mechanism (flexion/extension motion) was presented. From this case study, the reachable workspace of all fingers for 90%-99.9% of the adult human population is shown as four contours in Figure 4.2; these contours will form the basis of

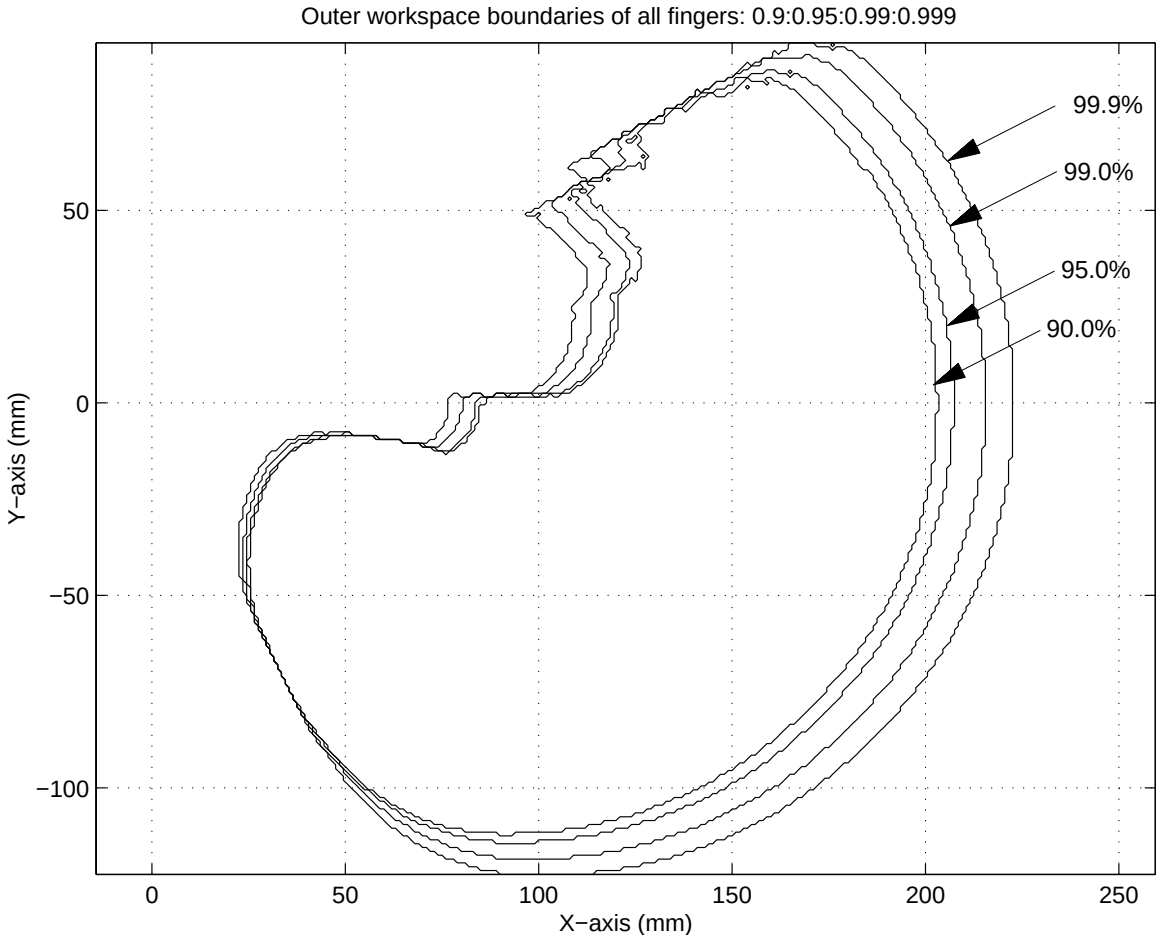

Figure 4.2: Stochastic reachable workspace of the human finger.

our target reachable workspace for the fingertip haptic display (FHD). The 99% contour, for example, bounds the locus of points which are reachable by 99% of the human population, as defined by the finger size distributions shown in Chapter 3.

The extended fivebar kinematic linkage was chosen as the basic linkage type for the FHD; its relatively thin profile allows multiple copies of the mechanism to exist in close proximity. The fivebar linkage is comprised of five rigid links connected by five rotary joints into a closed kinematic chain as shown in Figure 4.3. Since the mechanism forms a closed kinematic chain, the position of the control point (where the fingertip contact will occur) may be controlled by the position of the two ‘‘base’’ joints, J1 and J2. This allows actuators and sensors to be mounted at these two joints, thus minimizing the dynamic performance penalty for actuator and sensor mass.

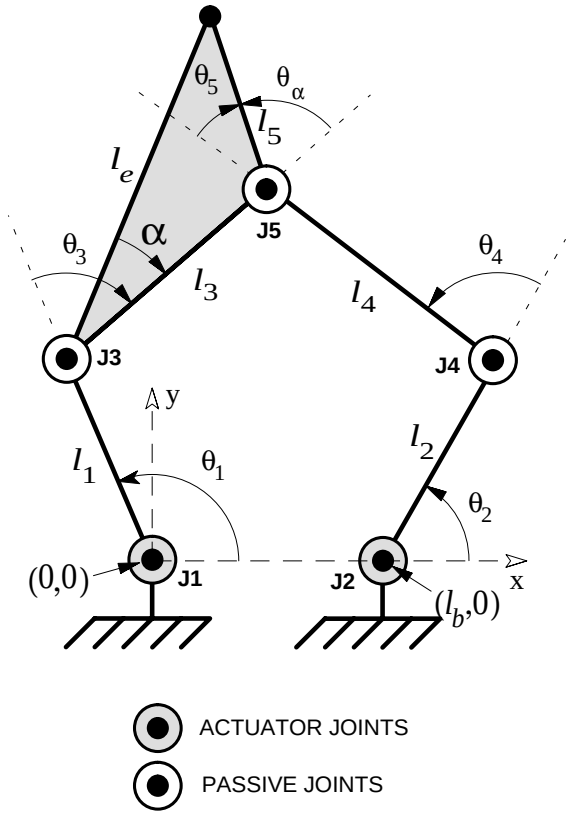

Figure 4.3: Extended fivebar kinematic linkage.

Flat coil actuators were chosen for use with this fivebar linkage. This type of actuator is commonly used in hard disk drives to control the position of the disk read/write head(s); it typically has a very thin profile but also has a very limited motion range (20°-40°) [21]. A new flat coil actuator was developed to allow larger motion range in a smaller volume and improve heat dissipation capability by embedding the coil into the actuated link. Due to design limitations for these actuators, we preselected 90° motion ranges for the flat coil actuated joints (J1 and J2).

4.5 OPTIMIZATION CRITERIA

The choice of a parallel mechanism with direct drive actuators allows the mechanism to have relatively high stiffness with relatively low friction and inertia. We therefore chose to focus our design optimization efforts on workspace size and force output capability over the workspace. In this section, we develop the Jacobian matrix for the extended fivebar mechanism and show how it can be used to determine the force output characteristics of a candidate kinematic design.

4.5.1 Mechanism Jacobian Matrix

The mechanism Jacobian matrix, J(θ) is a configuration dependant matrix which relates the *n*-element actuator joint velocity vector, $\dot{\theta} = [\dot{\theta}_1 \dot{\theta}_2 \ldots \dot{\theta}_n]^T$ to the control point's *m*-element Cartesian velocity vector, $\dot{X} = [\dot{x}_1 \dot{x}_2 \ldots \dot{x}_m]^T$:

$$\dot{X} = J(\theta)\dot{\theta} \tag{4.1}$$

$J(\theta)$ also relates the *n*-element joint torque vector, $\tau = [\tau_1\ \tau_2\ \ldots \tau_n]^T$ to the *m*-element Cartesian force vector at the control point, $F = [f_{x1}\ f_{x2}\ \ldots f_{xm}]^T$:

$$F = [J^T]^{-1}(\theta)\tau \tag{4.2}$$

For the kinematic structure shown in Figure 4.3, the two actuators imply that $n = 2$ and the planar motion means that $m = 2$; the 2×2 Jacobian matrix for this structure is

$$J(\theta) = \begin{bmatrix} J_{11}(\theta) & J_{12}(\theta) \\ J_{21}(\theta) & J_{22}(\theta) \end{bmatrix} = \begin{bmatrix} -l_1 s_1 + \dfrac{l_1 l_e s_{13\alpha} s_{1-24}}{l_3 s_{13-24}} & \dfrac{l_2 l_e s_{13\alpha} s_4}{l_3 s_{13-24}} \\ l_1 s_1 - \dfrac{l_1 l_e c_{13\alpha} s_{1-24}}{l_3 s_{13-24}} & \dfrac{-l_2 l_e c_{13\alpha} s_4}{l_3 s_{13-24}} \end{bmatrix} \tag{4.3}$$

where the notation s_{13-24} denotes $\sin(\theta_1+\theta_3-\theta_2-\theta_4)$, $s_{13\alpha}$ denotes $\sin(\theta_1+\theta_2+\alpha)$, etc.

4.5.2 Singular values of the Jacobian

The singular values, σ of $J(\theta)$ may be computed from the eigenvalues, λ, of $J^T(\theta)J(\theta)$ using [4]

$$\sigma = \sqrt{\lambda\{J^T(\theta)J(\theta)\}}\,. \tag{4.4}$$

The two singular values of the fivebar mechanism shown in Figure 4.3 may be derived in closed form for the 2×2 Jacobian given in (4.3):

$$\sigma_{\max} = \sqrt{0.5C_1 + \sqrt{0.25(C_2{}^2) + C_3{}^2}} \tag{4.5}$$

$$\sigma_{\min} = \sqrt{0.5C_1 - \sqrt{0.25(C_2{}^2) + C_3{}^2}} \tag{4.6}$$

where

$$\begin{aligned} C_1 &= J_{11}^2 + J_{12}^2 + J_{21}^2 + J_{22}^2 \\ C_2 &= J_{11}^2 + J_{21}^2 - J_{12}^2 - J_{22}^2 \\ C_3 &= J_{11}J_{12} + J_{21}J_{22} \end{aligned} \tag{4.7}$$

4.5.3 Dexterity Measures using Singular Values

For the set of all joint torque commands which satisfy the relation, $\|\tau\|_2 = 1$, the best-case [$f_{max}(\theta)$] and worst-case [$f_{min}(\theta)$] force outputs in all directions for this unit torque input at joint configuration θ is known [4] to be

$$f_{min}(\theta) = \frac{1}{\sigma_{max}(\theta)} \tag{4.8}$$

$$f_{max}(\theta) = \frac{1}{\sigma_{min}(\theta)} \tag{4.9}$$

The mechanism isotropy, $I_m(\theta)$ indicates how well it can move or apply forces in any direction at a given location. $I_m(\theta)$ is defined as

$$I_m(\theta) = \frac{\sigma_{min}(\theta)}{\sigma_{max}(\theta)} = \frac{f_{min}(\theta)}{f_{max}(\theta)} \tag{4.10}$$

Isotropy values approaching 1.0 are best for haptic mechanisms since if $I_m(\theta) = 1$, the mechanism can move and apply forces equally well in all directions.

We are interested in maximizing both the reachable workspace and the force output capability of the mechanism since these both have significant effects on the utility of the device as a haptic display. Both the worst-case force output and the isotropy values may be considered as local dexterity measures at a joint position θ. However a more global measure is needed for design optimization since we make no assumptions about where in the mechanism workspace the haptic device will be used for a particular application. For our design optimization, we chose the following global criterion function:

$$\max_{D}\left\{ A(W) \times \min_{W}[f_{min}(\theta)] \right\} \tag{4.11}$$

where D is our design space, W is the mechanism workspace for a given candidate mechanism, $A(W)$ is the workspace area, and $f_{\min}(\theta)$ is as defined in (4.8). To help the optimization yield reasonable isotropy over the workspace, we define the mechanism workspace, W as the set of points which have images in joint space (subject to joint limits) which satisfy the isotropy requirement of $I_m(\theta) \geq 0.75$.

4.6 FHD DESIGN SPACE

The kinematic structure shown in Figure 4.3 has 17 independent design parameters: five link lengths ($l_1,\ldots,l_5$), ten joint motion limits (min and max positions for each of five joints (J1,…,J5), the distance between the actuated joints (l_b) and the angle between l_3 and l_5 (θ_α). The range of these 17 parameters form the design space, D of the mechanism. The optimization process requires that this design space be searched for the best mechanism as defined in (4.11). Before starting the search, however, we need to establish the range of each parameter and attempt to reduce the dimensionality of the design space as much as possible.

4.6.1 Joint Motion Ranges

Since the motion range of the actuators were fixed at 90°, the motion ranges of θ_1 and θ_2 are constrained to a fixed range from some unknown offset. Thus the motion ranges for the actuated joints are:

$$(\theta_{1ofst} - 45°) \leq \theta_1 \leq (\theta_{1ofst} + 45°) \tag{4.12}$$

$$(\theta_{2ofst} - 45°) \leq \theta_2 \leq (\theta_{2ofst} + 45°) \tag{4.13}$$

The fivebar linkage has four possible kinematic configurations−the permutations of ‘‘elbow in’’ and ‘‘elbow out’’ for θ_3 and θ_4 (i.e., each of these joints having positive or negative values). Changing configurations requires the mechanism to become singular

(unable to move in some Cartesian direction) as the associated joint reaches the 0° position. Since these singularities are undesirable in the workspace, we limit our design to the dual elbow out configuration ($\theta_3 \leq 0°$ and $\theta_4 \geq 0°$) as shown in Figure 4.3. This has the added effect of avoiding self collisions between the θ_2 and θ_4 joints and their respective links. By limiting the extreme motion range of these two joints to 160°, we also avoid self collisions between the l_1 and l_3 links as well as between the l_2 and l_4 links. Therefore the motion ranges for these two joints are:

$$-160° \leq \theta_3 \leq 0° \tag{4.14}$$

$$0° \leq \theta_4 \leq 160° \tag{4.15}$$

These four limits reduce our design space, D by an additional 4 parameters, (θ_{3min}, θ_{3max}, θ_{4min}, θ_{3max}).

We also constrain the motion range of range of θ_5 to

$$-160° \leq \theta_5 \leq (\theta_\alpha - 20°). \tag{4.16}$$

to avoid self collisions between the l_4 link and the extension (links l_3 and l_5). This reduces our design space, D by two parameters,(θ_{5min} and θ_{5max}).

4.6.2 Mechanism Scaling

Uniform scaling of a mechanism involves scaling all mechanism link lengths by the same scale factor, k. We can see from (4.3) that each of the elements of $J(\theta)$ has units of length. The singular values of $J(\theta)$, as given in (4.5) and (4.6), also have units of length. Therefore, uniform scaling by the factor k will scale all elements of $J(\theta)$ by k and the values of f_{min} and f_{max}, as defined in (4.8) and (4.9) will also scale by the factor, $1/k$. This same scale factor will cause the workspace area to scale by k^2 while leaving the shape and topology of the workspace unchanged.

Since our design criterion (4.11) depends on the product of workspace area, $A(W)$ and workspace minimum force, $\min_W\{f_{\min}\}$, uniform scaling of the mechanism will cause the criterion to scale by k as well. We generate a scale-independent design optimization by constraining the total reach length of the mechanism to an arbitrary value of K:

$$l_1 + l_3 + l_5 = K \tag{4.17}$$

thereby reducing our design space by an additional parameter (only 4 link lengths instead of 5).

4.6.3 Reduced Design Space

In the previous section we have reduced our 17-parameter design space, D, by 9 parameters. The 8 remaining unconstrained parameters will be searched for an optimal design using the criteria function (4.11).

We define eight control variables for the optimization process, and discretize their values according to a minimum and maximum value as well as a step count, as shown in Table 4.1. These control variables are used to compute the kinematic parameters of each candidate design during the optimization process. Specifically, the link lengths are computed as

Table 4.1: Control Variables for Optimization

Index	Name	Minimum Value	Maximum Value	#Steps	Step Size
1	C_{l_5}	0.10	0.50	5	0.100
2	C_{l_1}	0.25	0.75	5	0.125
3	$C_{l_{24}}$	0.50	1.50	5	0.250
4	C_{l_2}	0.25	0.75	5	0.125
5	$C_{\theta_{1ofst}}$	0°	180°	19	10°
6	$C_{\theta_{2ofst}}$	0°	180°	19	10°
7	C_{l_b}	0	1.0	8	0.143
8	C_{α}	-45°	135°	7	30°

$$l_5 = C_{l_5} \times K, \tag{4.18}$$

$$l_1 = C_{l_1} \times (K - l_5), \tag{4.19}$$

$$l_3 = K - l_5 - l_1, \tag{4.20}$$

$$l_{24} = C_{l_{24}} \times (K - l_5) \tag{4.21}$$

$$l_2 = C_{l_2} \times l_{24}, \tag{4.22}$$

$$l_4 = l_{24} - l_2, \tag{4.23}$$

$$l_b = C_{l_b} \times K, \tag{4.24}$$

and the joint motion ranges are computed as in (4.12)-(4.16).

Equations (4.18)-(4.20) specify the lengths for the l_1, l_3 and l_5 such that $l_1 + l_3 + l_5 = K$, with l_5 getting between 10% and 50% of the total length and with l_1 getting between 25% and 75% of the remaining length $(K - l_5)$, according to the variables C_{l_5} and C_{l_1} respectively. Equations (4.21)-(4.23) specify the lengths of the l_2 and l_4 links such that the total length of these two links ($l_{24} = l_2 + l_4$) has a value between 50% and 150% of the total length of the l_1 and l_3 links $(K - l_5)$ as determined by $C_{l_{24}}$ variable and the length of the l_2 and l_4 links each having values between 25% and 75% of this total length, l_{24} according to the C_{l_2} variable. Equation (4.24) specifies the distance between the two actuators as having a value between 0% and 100% of the total length, K, as determined by the C_b variable. The number of steps for each control variable in Table 4.1 were chosen to make the step sizes similar in terms of units of length. So the step sizes of 10° for $C_{\theta_{1ofst}}$ and $C_{\theta_{2ofst}}$ angular variables are chosen so that a 10° motion at the base of either J1 or J2 (all other joints constant) translates to a arc-length offset of 0.17 for K=1 (arc length is $2\pi K(\theta°)/360°$) which is similar to the step sizes of the other linear variables with the same K value.

4.7 OPTIMAL SEARCH

According to Table 4.1, our design space of 8 variables has

$$5\times5\times5\times5\times19\times19\times8\times7 = 12{,}635{,}000 \tag{4.25}$$

design candidates. Since (4.11) is non-analytic and, in general, will contain an unknown but likely large number of local minima, optimal search techniques such as gradient descent are ill-suited to this design task. Instead, an exhaustive search was performed on the design space.[1]

4.8 RESULTS

For the optimization process, the design candidates were divided among 10 computers with each computer assigned a number of design candidates commensurate to its speed so that all computers would complete the calculation in about the same amount of time.

For each design candidate, a rough workspace region boundary was established according to the maximum reach of the mechanism as defined by (4.17) with K set to an arbitrary value of 1. This region was then divided into a discrete grid of 0.01×0.01 unit squares; an in-memory representation of this grid was used to store the $f_{\min}$ value at that location. Each $f_{\min}$ value was computed from the joint positions associated with that Cartesian position via an inverse kinematics transform. If any of the joint positions were outside of the limits defined for that particular design candidate, or if the isotropy was less than the required 0.75, then a 0 value was recorded at that position instead. The number of grid elements with non-zero values is the workspace area; the product of this area value and the minimum non-zero element of all grid elements is the criterion function (4.11) value for a given design candidate. This value was stored in a file for later comparison against all other candidate designs.

---

[1] A culling algorithm presented in [18] can provide a significant improvement over a purely exhaustive search; unfortunately, it was not published in time to be of help for the work presented in this chapter.

The search process was completed in approximately 48 hours using all 10 computers simultaneously. Post-processing of the search results found that only 70 design candidates were in the top 10% of the best design, as determined by the value of our criterion function. We then determined that an approximate scale factor of K=200mm would allow these various candidate mechanisms to best fit our target workspace, as shown in Figure 4.2.

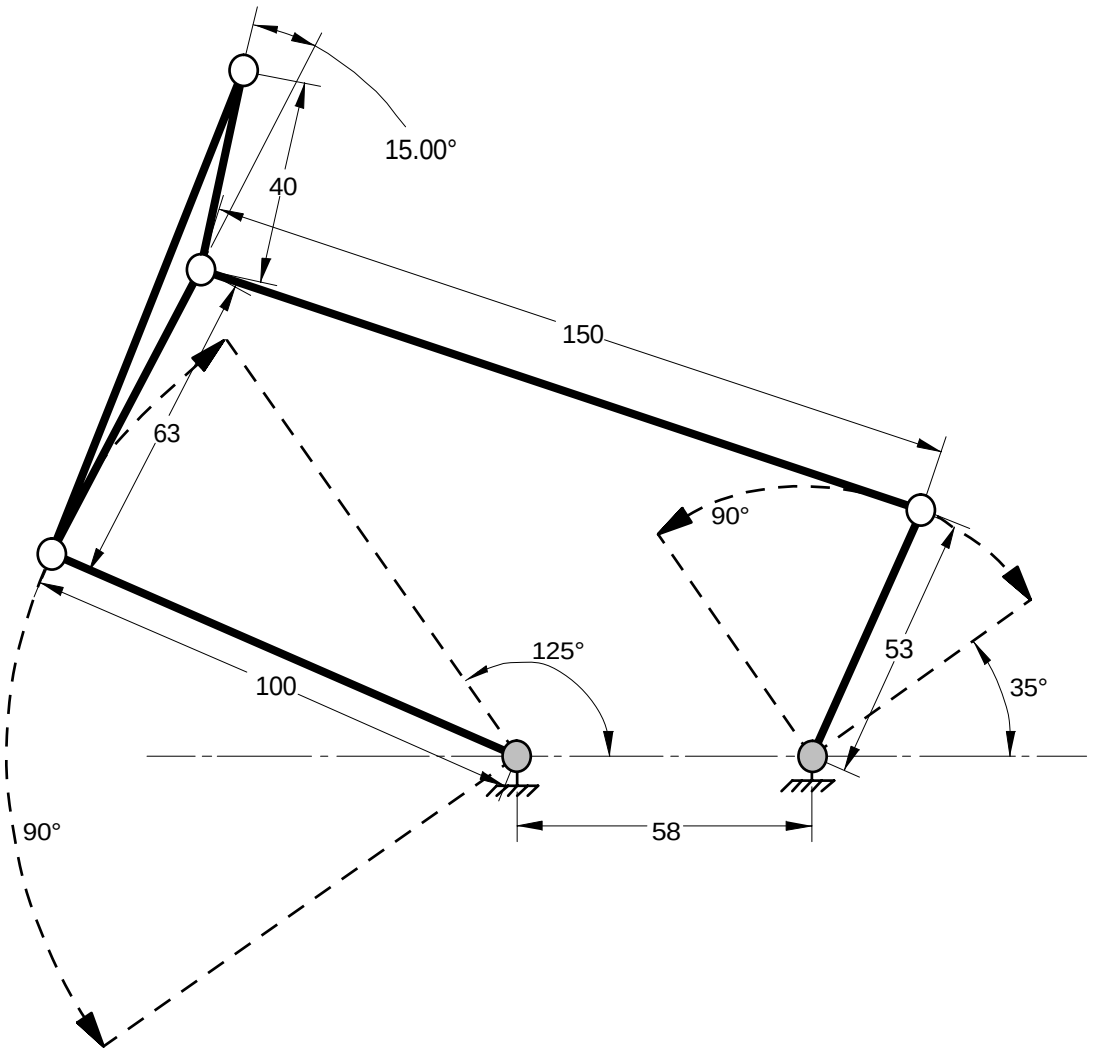

Figure 4.4: Final FHD Kinematic Parameters

In considering the implementation of these various candidate designs, we found that the l_b design parameter (the distance between the actuator axes of rotation) was particularly important. While six of the seven possible values of this parameter were used in the top 70 designs, we found that the value, $C_{l_b} \cong 0.29$ which gives a corresponding value of l_b =58mm for the K=200mm scale factor, was best suited for implementation of our flat coil actuators from a single integrated base unit. We therefore chose the best of the design candidates subject to the $C_{l_b} \cong 0.29$ constraint. The kinematic structure of the chosen design is shown in Figure 4.4; this design has a criterion function value of 67.4 while the overall best of all candidate designs has a corresponding value of 72.7.

Figure 4.5 shows the relations between the finger workspace (95% of population) and the reachable workspace of our chosen mechanism design. A plot of the $f_{\min}$ values over the workspace of our chosen mechanism design is shown in Figure 4.6, where the origin of the plot coincides with the location of the θ_1 joint.

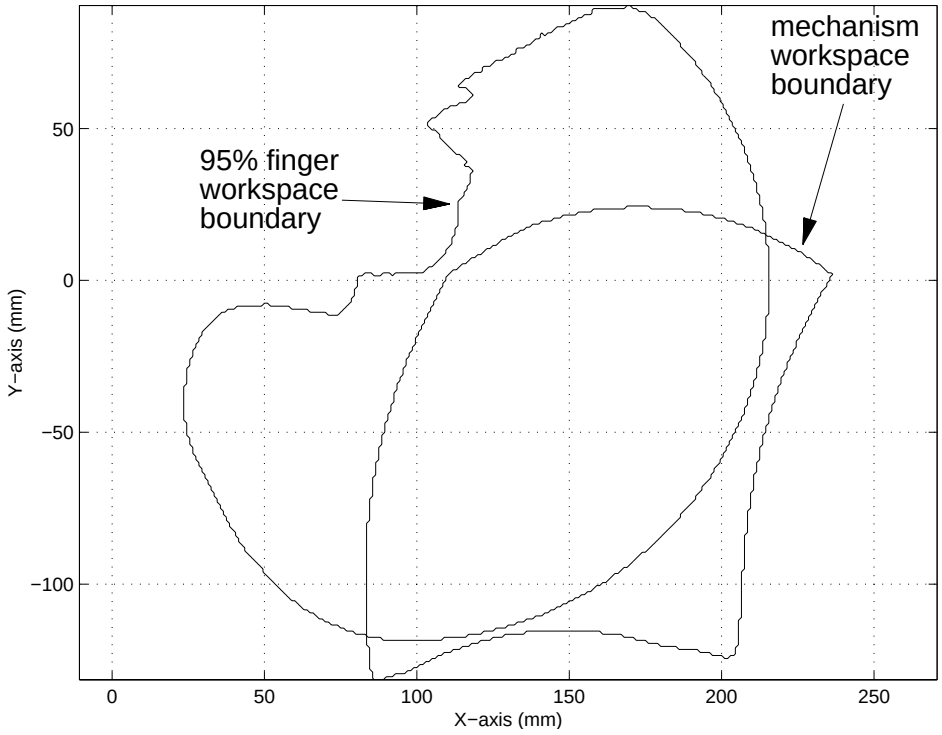

Figure 4.5: Overlay of finger and mechanism workspaces.

4.9 CONCLUSIONS

In this chapter, we have shown the process of kinematic design based on optimization of mechanism workspace and overall minimum force output. The optimization process was based upon a search of a reduced design space of the mechanism, with over 12 million mechanism design candidates being considered. The resulting design of a fingertip haptic display (FHD) has been implemented in our lab and is currently in use in experimental studies of human perception of surface properties using the fingertip. Some details of the implementation of the FHD may be found in Appendix B.

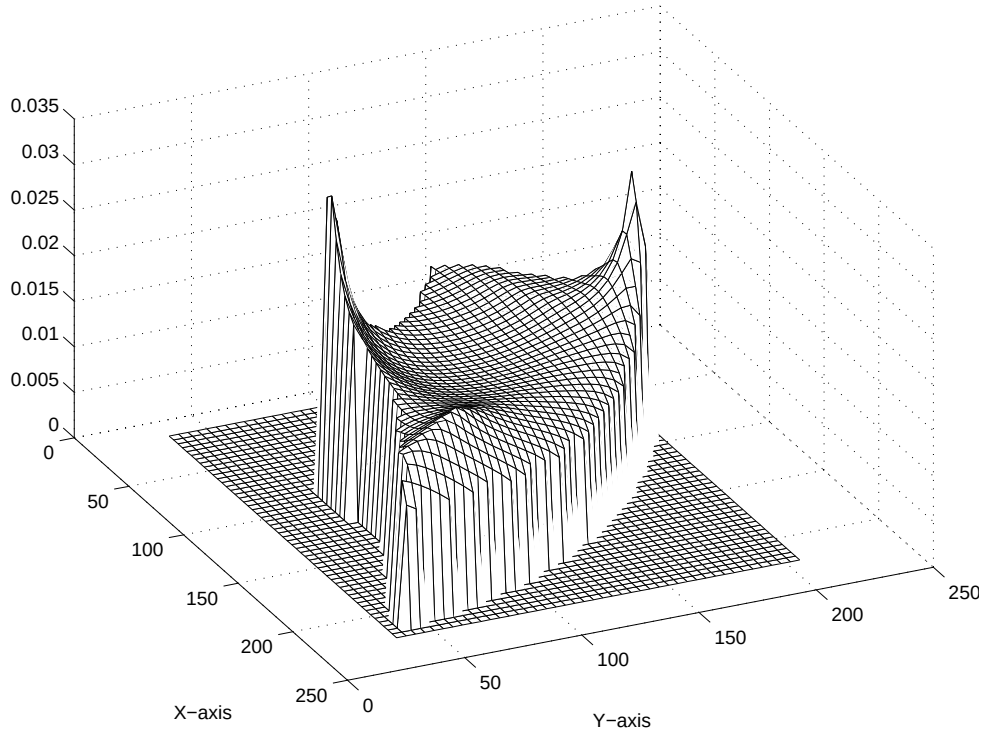

Figure 4.6: Fmin values of FHD mechanism over workspace

Notes to Chapter 4

[1] Hannaford, B. and S.C. Venema, *Kinesthetic Displays for Remote and Virtual Environments*. In W. Barfield and T.A. Furness III, editors, Virtual Environments and Advanced Interface Design, chapter 10. Oxford University Press, 1995.

[2] Fabiani, L., G. Burdea, N. Langrana, and D. Gomez, *Human Interface Using the Rutgers Master II Force Feedback Interface*, Proc. IEEE VRAIS'96, pp. 54-59, 1996.

[3] Craig, John J., *Introduction to Robotics*, Addison-Wesley, Reading, MA, 2nd edition, 1990.

[4] Yoshikawa, T., *Foundations of Robotics*, MIT Press, Cambridge, MA, 1990.

[5] Sugimoto, K. and J. Duffy, *Determination of Extreme Distances of a Robot Hand--Part 1: A General Theory*, Journal of Mechanical Design, 103:631-636, July, 1981.

[6] Selfridge, R.G., *The Reachable Workarea of a Manipulator*, Mechanism and Machine Theory, 18(2):131--137, 1981.

[7] Korien, J.U., *A Geometric Investigation of Reach,* University of Pennsylvania, 1984. Republished with same title by MIT Press, Cambridge, MA 1984.

[8] Kumar, A. and K.J. Waldron, *The Workspaces of a Mechanical Manipulator*, Journal of Mechanical Design, 103:665-672, July 1981.

[9] Wampler, C.W., *Winding Number Analysis of Invertible Workspaces for Redundant Manipulators*, Proceedings of 28th Conference on Decision and Control, pp. 546-569, Los Angeles, CA, Dec. 1990.

[10] Paden, B. and S. Sastry, *Optimal Kinematic Design of 6R Manipulators*, International Journal of Robotics Research, 7(2):43-61, March/April, 1988.

[11] Jau, B.B., *Man-Equivalent Telepresence Through Four Fingered Human-Like Hand System*, Proc. International Conference on Robotics and Automation, San Francisco, USA, pp. 1520-1532, May, 1986.

[12] Buttolo, P. and B. Hannaford, *Pen Based Force Display for Precision Manipulation of Virtual Environments*, Proceedings VRAIS-95, pp. 217-225, Raleigh, NC, March 1995.

[13] Iwata, H., *A Six Degree-of-freedom Pen-based Force Display*, Proc. Fifth International Conference on Human-Computer Interaction, vol, 2, pp. 651-656, Orlando, FL, USA, Aug. 1993.

[14] Hodges, M., *It Just Feels Right*, Computer Graphics World, pp. 48.56, October, 1998.

[15] Massie, T.H. and J.K. Salisbury, *Probing Virtual Objects with the PHANToM Haptic Interface*, Proc. ASME Winter Annual Meetings, Chicago, 1994.

[16] Kurtz, R. and V. Hayward, *Multiple-Goal Kinematic Optimization of a Parallel Shperical Mechanism with Actuator Redundancy*, IEEE Transactions on Robotics and Automation, 8(5):644-651. October, 1992.

[17] Hayward, V., J. Choksi, G. Lanvin and C. Ramstein, *Design and Multi-Objective Optimization of a Linkage for a Haptic Interface*, In J. Lenarcic and B. Ravani, editors, ‘‘Advances in Robot Kinematics and Computational Geometry,’’ pp. 359-368. Kluwer Academic Publishers, 1995.

[18] Kircanski, M., *Kinematic Isotropy and Optimal Kinematic Design of Planar Manipulators and a 3-DOF Spatial Manipulator*, International Journal of Robotics Research, 15(1):61-77, 1996.

[19] Stocco, L.J., S.E. Salcudean and F. Sassani, *Mechanism Design for Global Isotropy with Applications to Haptic Interface*, Proceedings of the ASME Dynamic Systems and Control Division, pp. 115-122, 1997.

[20] Lee, S.H., B-J. Yi and Y.K. Kwak, *Optimal Kinematic Design of an Anthropomorphic Robot Module with Redundant Actuators*, Mechatronics 7(5):443-464, 1997.

[21] Buttolo, P., D.Y. Hwang and B. Hannaford, *Hard Disk Actuators for Mini-Teleoperation*, Proceedings of the SPIE Telemanipulator and Telepresence Technologies Symposium, pp. 55-61, Boston, MA, October 1994.

CHAPTER 5: EXPERIMENTS IN FINGERTIP PERCEPTION OF SURFACE DISCONTINUITIES

5.1 INTRODUCTION

When developing devices which in some way aid or augment our natural senses, an understanding of our sensory limitations plays an important part in how we approach the design of these devices. For example, our inability to sense small, discontinuous visual motions allowed the development of realistic cinema and television by displaying discrete visual frames at ~30 Hz., relying upon the limitations in our visual perception to fuse this discrete display into a perceptually smooth simulated visual environment. Similarly, the development of the early telephone technology was aided by the fact that only 3 kHz bandwidth was necessary for the transmission of intelligible speech.

In the field of haptic simulation, a similar understanding of our haptic perception is needed. While haptic perception has been an active research area for many decades, the pace has increased substantially in the past few years as interest has grown in the area of haptic simulation and as commercial applications of haptics have begun to be deployed. A wide variety of commercial haptic devices with different performance capabilities and costs are available today. Typically, the capabilities of a haptic display are directly related to its cost of fabrication: increasing display quality will cause increasing design and fabrication costs as well as increasing computational requirements. A better understanding of haptic perception may allow better informed answers and decisions related to the question, ‘‘how good is good enough?’’

Just as visual computer simulations of complex surfaces are often approximated by planar facets, so too are haptic simulations. In visual simulation, techniques such as Gouraud shading [18] are used to make the surface appear smoother than it really is. This

is necessary for high-quality visual displays of faceted surfaces because our eyes generate a perceptual emphasis on intensity discontinuities, called Mach banding. With haptic perceptions, no similar mechanism has been observed. However, it is still necessary to consider, for example, how a given granularity of faceted surfaces will be perceived in a haptic simulation. A thorough understanding of these and other perceptual issues in haptic simulation are increasingly important as we begin to see the use of haptic simulation in computer-aided design (CAD), medical training, and computer games in the entertainment industry.

In the following experiments, we will be examining the haptic perception of changes in slope and curvature. Specifically, we will be looking at how well humans can locate discontinuities in both slope and curvature when haptically exploring a curvilinear surface with the fingertip using the UW Fingertip Haptic Display (FHD). We first begin with a review of previous work in haptic perception of curves and surfaces. We then review some formal definitions of discontinuities and discuss the implementation of a haptic environment with the FHD before detailing two separate perceptual experiments performed with a number of test operators using the FHD.

5.2 PREVIOUS WORK

Haptic perception at the fingertip is part of the complex and larger human haptic sensory system. The haptic sense may be subdivided into a kinesthetic sense of joint positions and forces based on muscle spindle and Golgi tendon organ mechanoreceptors [17] and a tactile sense based on (sub)cutaneous mechanoreceptors that respond to localized contact forces, temperatures, etc. [17]. At the lowest level, the neurophysiology of the different types of haptic receptors are fairly well understood--at least in terms of basic stimulus and response behavior (c.f. [36][40][41]) though perhaps less well understood in terms of biomechanics [33]. However, the mechanisms and limitations related to the

cognitive perception of haptic stimuli are still not well understood and are an active research topic. By studying how humans perceive and interact with controlled environments using their haptic sense, a better understanding of these higher-level issues may be gained. This human psychophysical experimentation is the primary tool of the researcher attempting to gain further understanding of human haptic perception.

Psychophysical research in haptic perception is currently a very active research area: more than 40% of the papers reviewed in this section were published in the past five years. A large portion of this research is directed at the cognitive aspects of haptic perception: how we perceive and recognize objects [37][26], what exploration strategies are used in this process [27][28], and how the haptic perception interacts with other senses such as the visual sense [25][47][11]. But a significant portion of the haptics research focuses on the basic limitations of haptic perception. The remainder of this review will focus on haptic perception limitations as it is more most applicable to the experiments presented later in this chapter.

The haptic perception of curvature is particularly interesting in that it is an important requisite to our perception of the shape or form of objects that we touch. Early psychophysical haptics research by Ruben [38] in 1939 and later repeated with variations by Crewdson and Zangwill [7] in 1949 and by Hunter [21] in 1952 studied the perception of curvature as sensed at the fingertips using large-scale arm motion (forearm and/or upper-arm sweeping motions) In these primarily kinesthetic experiments, a thin metal ruler configured with the long edge up and a slight outwardly-bowed shape was perceived to be flat by both blind and sighted (but blindfolded) test subjects seated in front of the ruler. Other researchers have noted similar haptic misperceptions (sometimes called ‘‘haptic illusions’’) for quantities such as length and stiffness when using a palm-referenced haptic display device [20] and also hand-held probing tools (e.g., a long rod [19]). Hogan

[20] showed that the haptic position sense appears to be metrically inconsistent in terms of a geometric model: the experimentally observed distortions in length perception do not fit a geometric model. Some studies have revealed additional haptic illusions such as a perceived asymmetric skew when scanning a symmetrical curve [13]. Additional misperception effects may be due to either receptor adaptation (e.g., cool water feels warm to very cold fingers) or perceptual after-effects, where an earlier stimulus affects the perception of a subsequent stimulus, as Vogels, et al. [45] found for curvature perception of multi-sized spherical surfaces.

Davidson [9] and also Davidson and Whitson [8] found that curvature judgements can also vary by reason of skill. Specifically, he studied the exploration methods that subjects used in exploring a haptic environment similar to the one used by Ruben [38] and found that blind subjects were better at identifying curvature as one of three states (convex, concave, or straight) than blindfolded sighted subjects. Moreover, when the sighted subjects were tutored to use the blind subjects' search techniques, their performance improved significantly.

Gordon and Morison [16] used 20mm wide curved strips (portions of planoconvex lenses) and found that subjects could detect the difference between a flat surface and curved surface with only a 0.09mm base-to-peak height change using only motion of the fingertip and wrist; the difference detection threshold for two different curves was found to be as little as 0.11mm. They also found that radius of curvature was not a good scale-independent predictor of performance, but that the ''gradient,'' defined as the base-to-peak height divided by half the base length, would instead be a very good predictor of performance over different scales in a difference detection experiment.

Goodwin, et al. [15] ''...measured the capacity of humans to scale and discriminate surfaces that differed in curvature when applied passively to the pad of the index finger.''

They found that subjects could, at 75% accuracy, discriminate a flat surface from a convex curvature having 204mm radius and a concave curvature of 185mm radius. In addition, subjects were able to discriminate between paired surfaces having radii of 6.95mm and 6.33mm as well as 2.48mm and 3.13mm with the same level of accuracy in forced choice experiments. A later paper by Goodwin and Wheat [14] showed that pairwise discrimination could be made when keeping finger contact area constant for 13% and 18% increases in curvature for base stimuli of 3.5mm and 6.5mm respectively

Kappers, et al. [24][22] studied unilateral and bilateral whole-hand discrimination of different variations of doubly-curved, mathematically defined surfaces that ranged from spherical paraboloids to hyperbolic paraboloids (single axis domes and double-axis saddles) for constant curvature values in a forced-choice sorting of surfaces according to a predefined shape classification system. They also explored the just-noticeable-difference (JND) values of these surface pairs. Another publication by Kappers, et al. [23] included variable curvature values (including both concave and convex surfaces) as well. They found that unilateral performance (successive examination of two surfaces with one hand) was generally better than bilateral (simultaneous examination of two surfaces with two hands) in JND tests.

Pont, et al. [35] studied the ability of subjects to discriminate a difference in curvature on different portions of both the palmar and dorsal sides of the hand. Thin (2mm) curved strips of varying lengths were applied statically to different parts of the hand and compared to reference strips. The reference strips were 1000mm radii convex and concave arcs while the test strips varied in curvature from flat (infinite radius) to 560mm radius. Their results indicate that the cutaneous receptors on the palmar side of the hand do indeed improve discrimination performance. Additional analysis indicated that the

observed ‘‘...differences in the thresholds for the different positions on the hand were due primarily to the length over which the stimulus was touched.’’

West and Cutkosky [46] reported the results of experiments in detecting the number of cycles in a sinusoidally-shaped 1-dimensional surface. Four different protocols were used: One was a bare fingertip tracing the surface; the remaining three all used a stylus to trace the surface, but in one case the stylus was attached to a haptic device tracing a virtual surface while in the other two cases the stylus itself traced a physical surface--either directly or with a roller bearing to reduce friction. Subjects were asked to count the number of sinusoidal cycles present on a given trial surface which varied from 1-20 cycles over the 85mm surface length with the error rate defined as the percentage of cycles that were uncounted. Using an average error rate of 50% as a ‘‘correct’’ detection threshold, they found that, in general, the bare finger did best, followed by the physical surface tracing, with the virtual tracing performing the worst. There was no significant performance difference between the two levels of friction for the physical surface, but they found that higher stiffness levels would increase the performance in tracing the virtual surface, subject to stability limitations of the virtual device and simulations system.

Tan [43] developed an experiment based on the absolute identification paradigm where subjects were asked to individually identify *k* distinct virtual hemispheres in a vertical virtual wall using a PHANToM™ haptic display. As the number of stimuli, *k* is increased while the range of the stimuli were kept constant at 10mm and 80mm radius respectively for the smallest and largest hemisphere, the ability to correctly identify all *k* stimuli decreases. Tan found that human operators could correctly identify 3 to 4 sphere sizes over this range. The results were also formulated in terms of information transfer (IT), expressed in bits.

Haptic perception of angles is also relevant to our planned experiments. Appelle [2] studied the ability of subjects to compare the relative size of a reference angle to a trial angle; each of the angles were formed out of a pair of hinged wooden arms. Four sub-experiments were performed which consisted of the four permutations of haptic or visual observation of the reference angle and haptic or visual observation of the trial angle. The subjects were asked to state for each trial whether the trial angle had larger, smaller or the same value as the reference angle. In iterated trials the point of subjective equality (PSE) was found for a set of 7 reference angles (30°, 45°, 60°, 90°, 120°, 135° and 150°). Intra-modal judgements were found to be significantly more accurate than crossmodal ones: visual-visual comparisons did best over all angles, while haptic-haptic comparisons tended to be less accurate for larger angles. Crossmodal judgements (haptic-visual and visual-haptic) tended to have significantly worse performance with biases indicating that haptic perception of angle was consistently smaller than the visual perception, which was more accurate to the true angle value. Stanley [42] performed similar experiments with the crossmodal ability to add and average angles. An extensive set of experiments recently published by Lakatos and Marks [30] also tested the visual/haptic perception of angular extent using triangular blocks of differing sizes and angles at the apex. They too noted that ‘‘...haptic underestimations of angle occur in a number of different stimulus contexts...’’ but also noted that visual cues seemed to ‘‘recalibrate’’ the haptic perception under some conditions.

Lederman and Klatzky [31] experimented with the perception of a variety of object properties such as hardness, smoothness, temperature, as well as spatially coded properties such as the presence and direction of ridges on a surface. These ridges form a sort of 0th-order surface discontinuity--however, the focus of this research was on the time

necessary to make accurate detection, not the range of surface features of which detection was possible.

The published research reviewed above addresses a number of interesting and important issues related to haptic perception and its limitations. However, no research to date has begun to explore the area of detection and perception of surface discontinuities. A better understanding of these issues would allow the developers of haptic simulation systems to better know the fidelity to which haptic environments should be rendered.

5.3 DISCONTINUITIES AND CURVES

A function is *n*-th order continuous if the first *n* derivatives of that function exist and are continuous over some given domain. Thus, if we represent a planar curve using the relation, $y = f(x)$, we know that it is first and second order continuous over a given domain if and only if $\mathrm{d}f/\mathrm{d}x$ and $\mathrm{d}^2f/\mathrm{d}x^2$ exist respectively on that domain. Representations of curves and surfaces are quite varied and complex; there are also some different definitions of discontinuity in relation to curves. Veltkamp [44] provides a thorough review of the types of (dis)continuities of curves and surfaces. Barsky and DeRose [3] provided a more focused discussion of geometric continuity for parametric curves. A brief review of the concept of curve continuity based on these papers is provided in the remainder of this section; the reader is referred to texts on geometric modeling (c.f., [32]), differential geometry (c.f., [10]), and computer aided design (c.f., [12]) for more in-depth information on these topics.

Curves are often represented parametrically. For example, a circle in the (x, y) plane may be represented by the equations,

$$x = r\cos(\theta)$$
$$y = r\sin(\theta) \qquad (5.1)$$

where θ is the curve parameter defined over some domain (typically $-\pi \le \theta < \pi$). More generally, the parametric representation of an arbitrary curve in an *n*-dimensional space is an *n*-element vector valued function, $x: \Re \rightarrow \Re^n$,

$$X(t) = \begin{bmatrix} x_1(t) \\ x_2(t) \\ \cdots \\ x_n(t) \end{bmatrix} \tag{5.2}$$

for the parameter *t* over the domain $t_{\min} \le t \le t_{\max}$ [44].

Specifying a curve to fit some complex set of criteria is often very difficult to achieve so curves are often defined in a piecewise manner by partitioning the domain of the parameter *t* into subranges and defining separate curves for each subrange. By allowing overlap of the partitioned subranges of *t* for each piecewise curve, a blending of the curves may be achieved in the overlap areas. Several types of spline functions use this approach to achieve different types of blending effects. See [32] for a thorough discussion of these various spline curves and surfaces. The continuity properties at the intersection of these blended curve segments for various types of parameterizations motivated much of the research and literature on this topic.

Order *n* continuity of a parametric curve is called ‘‘parametric continuity’’ and denoted C^n in the literature. Two intersecting parametric curves, $r(u)$ and $s(v)$ are C^n continuous at their point of intersection, $r(u_o) = s(v_o)$ if and only if their *n*-th derivatives evaluated at u_o and v_o respectively, are equal [44], i.e.,

$$\left. \frac{\mathrm{d}^n r}{\mathrm{d}u^n} \right|_{u = u_o} = \left. \frac{\mathrm{d}^n s}{\mathrm{d}v^n} \right|_{v = v_o} \tag{5.3}$$

However, a given curve may have many different parametric representations which have different parametric continuity properties. A less restrictive definition of continuity, called ‘‘geometric continuity’’ and denoted G^n for an n-th order geometric continuity, is based on intrinsic curve properties such as tangency and curvature. By reparameterizing the curves using arc-length, it can be shown [3] that two curves $r(u)$ and $s(v)$ are n-th order geometric continuous at u_o and v_o if and only if the corresponding arc-length parameterized curves are C^n continuous at these points.

5.4 HAPTIC SIMULATION ENVIRONMENT

For the purposes of experimentation detailed in later sections of this chapter, a planar haptic environment consisting of two intersecting circular arcs as shown in Figure 5.1 was implemented. The geometry of the two arcs, designated *A* and *B*, is specified by their curvature ($1/r_A$ and $1/r_B$ respectively), their angular extent (ext_A and ext_B respectively), the location of the intersection point, (x_i, y_i) and the tangent angles at the intersection point (ϕ_A and ϕ_B respectively). Negative curvature indicates that the associated arc curves

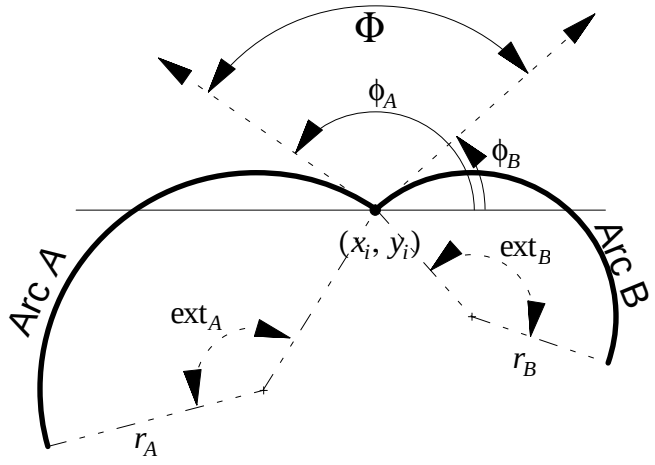

Figure 5.1: Haptic environment for experiments

to the right when moving from the intersection point to the associated arc endpoint; exact zero curvature is not allowed in the model due to computational limitations, but very small curvatures corresponding to radii of 100m were used to approximate flat surfaces as needed[2]. When traveling along the arcs from the extreme end of *A* to the intersection point to the extreme end of *B*, either the left or the right side of this path may be selected as the solid side of the environment.

Parametric representations of these two arcs in this environment are

$$x = x_A + r_A\cos(\theta_A)$$

for arc *A*: $$y = y_A + r_A\sin(\theta_A) \tag{5.4}$$

$$x = x_B + r_B\cos(\theta_B)$$

and for arc *B*: $$y = y_B + r_B\sin(\theta_B) \tag{5.5}$$

where the parametric variables, θ_A and θ_B have the following ranges:

$$(\theta_{Ai} - \text{ext}_A) \le \theta_A \le (\theta_{Ai})$$

$$(\theta_{Bi}) \le \theta_B \le (\theta_{Bi} + \text{ext}_B) \tag{5.6}$$

The parametric representation given by (5.4) and (5.5) are not true arc-length parameterizations. If reparameterized to arc-length, the resulting representation is C^1 continuous if and only if $\phi_A = \phi_B + 180°$, which implies that the representation given by (5.4) and (5.5)is G^1 continuous under the same conditions. This observation is relatively obvious by studying the geometry shown in Figure 5.1: the tangent vectors shown as dashed vectors with origins at (x_i, y_i)must be co-linear and pointing in opposite directions.

---

[2]This approximation generates a worst-case offset error of less than 0.01mm when moving across the entire ~100mm wide workspace--a negligable amount since it is gradual over the entire motion motion range.

5.4.1 Force Simulation Model and Algorithm

The control algorithm for the FHD is based upon a variation of the penalty force method for haptic display detailed by Zilles and Salisbury [48] and Colgate, et al. [5]. During operation, the Cartesian position of the FHD is computed with joint position data available from rotary position encoders mounted on the two FHD base joints. A computed virtual point, (x_v, y_v) tracks the Cartesian location of the FHD device, (x_d, y_d) as long as motion occurs in free space. When the device comes into contact with one of the virtual arcs, the (x_d, y_d) values continue to track the device as it penetrates the virtual surface while the virtual location, (x_v, y_v) is constrained to remain on the virtual surface at the point closest to the device location, (x_d, y_d) as shown in Figure 5.2. Feedback forces to the operator are computed according to an impedance control law using a virtual spring and damper to connect the physical location of the FHD to its virtual location on the surface. The control law is formulated so that the forces resisting surface penetration are along the normal vector, y_N. Forces along the surface tangent vector at the contact point

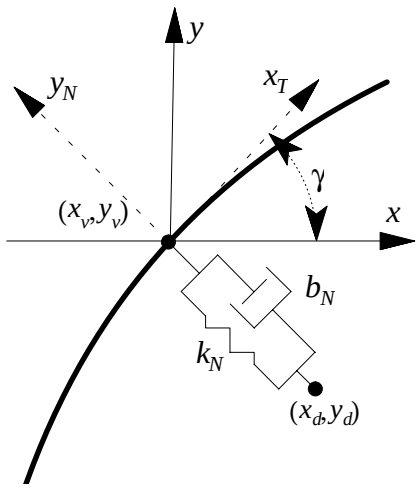

Figure 5.2: Surface normal impedance model

are possible as well, perhaps to simulate surface friction; however, tangential forces were not used in these experiments.

The force output relative to the surface normal is computed as

$$f_N = k_N e_N + b_N \dot{e}_N \tag{5.7}$$

where

$$e_N = \sqrt{(x_d - x_v)^2 + (y_d - y_v)^2} \tag{5.8}$$

is the surface penetration error or penalty function. In the Cartesian reference frame, this force is computed as

$$F = \begin{bmatrix} f_x \\ f_y \end{bmatrix} = \begin{bmatrix} \cos(\gamma) & -\sin(\gamma) \\ \sin(\gamma) & \cos(\gamma) \end{bmatrix} \begin{bmatrix} 0 \\ f_N \end{bmatrix} \tag{5.9}$$

and the associated motor torques are computed from the relation, $\tau = J^T(\theta)F$ where $J(\theta)$ is the FHD Jacobian matrix at joint positions, $[\theta_1, \theta_2]^T$.

The haptic simulation uses four mutually exclusive states to give physically consistent behavior. The disconnected state, S_D represents the free-motion state where there is no contact with any virtual object and thus no forces are fed back to the operator. Two states, called S_A and S_B, represent the cases of being in contact with the *A* and *B* arcs respectively. A special state, S_C indicates contact with the intersection point between the two arcs. It turns out that this state only exists for convex contact configurations. Transitions between states are handled by a set of rules based on the environment geometry and the previous and current virtual positions (x_v, y_v). This virtual position and associated forces and contact states are periodically updated at a 1ms interval.

The quality or ‘‘feel’’ of the haptically simulated surfaces is controlled by the values of the k_N and b_N control parameters for the stiffness and damping of the coupling between

the FHD device and the virtual surfaces. Ideally, we would like to simulate rigid objects using very high stiffness. However, inherent limitations due to the physical inertia and stiffness of the FHD as well as its limited actuator output capability necessitates smaller stiffnesses in order to have stable contact. The damping term helps to reduce the instability for a given stiffness; however, the amount of damping that can be added in the control system is limited by time and position resolution since the damping is based on a computed velocity estimate. Details of these issues as well as trade-offs in parameter values and their relationship to contact stability have been published recently by Adams and Hannaford [1].

5.5 FIRST EXPERIMENT: FIRST-ORDER DISCONTINUITIES

The first experiment measures how well humans perceive G^1 discontinuities with a haptic display. A simplified version of the haptic environment shown in Figure 5.1 was used where the two arcs were flat and the magnitude of the G^1 discontinuity was defined as the value of Φ. The specific values of Φ used in this experiment were

$$\Phi \in \{174°,176°,177°,178°,179°,180°,181°,182°,183°,184°,186°\} \qquad (5.10)$$

At the central value (180°) there was no discontinuity to be perceived, while the smaller values provided a concave ‘‘valley’’ of increasing sharpness and the larger values provided a convex ‘‘peak’’ of increasing sharpness. The extents of the two surfaces were chosen so that the ends of the surfaces were outside of the reachable workspace of the FHD mechanism. The intersection point, (x_v, y_v) was located in the central portion of the FHD workspace with a constant height but a randomly varying horizontal offset (uniform distribution) over a range of ±10mm for each subject trial to avoid any learning effects in the trials.

5.5.1 Stiffness & Damping Control Gain Values

The contact stability of the haptic display is affected by the mechanical parameters of both the haptic display mechanism and the human finger, as well as the software control system parameters. Since the mechanical parameters of the human finger can vary significantly (e.g., muscle co-contraction will increase the finger joint stiffness), the stability properties of the entire system can vary significantly from one moment to the next (c.f., [4]).

When choosing the k_N and b_N control parameters, a trade-off must be made between how stiff or ‘‘crisp’’ a simulated surface will feel and how much contact instability will be generated. Contact instability typically appears as a vibration or chattering when contacting a virtual surface; it disappears as soon as contact is withdrawn and the device enters the free-motion state. The control parameters may adversely affect the ability to sense discontinuities in different ways:

1. If the stiffness, k_N is too small the surface will feel soft or mushy and a discontinuity will presumably be more difficult to detect.
2. Higher damping values have been shown to increase the perceived ‘‘hardness’’ of a surface (initial contact forces) [29] which might improve the ability to detect discontinuities.
3. If the stiffness is too high, or if the damping value, b_N is set incorrectly, vibration due to contact instabilities will presumably tend to mask the discontinuity.

To allow exploration of the effect of the control parameters on the ability to detect/locate discontinuities, a set of different stiffness/damping control parameter pairs were needed. A preliminary experiment testing contact stability for a variety of stiffness/damping control parameter gain pairs was performed, using a very subjective

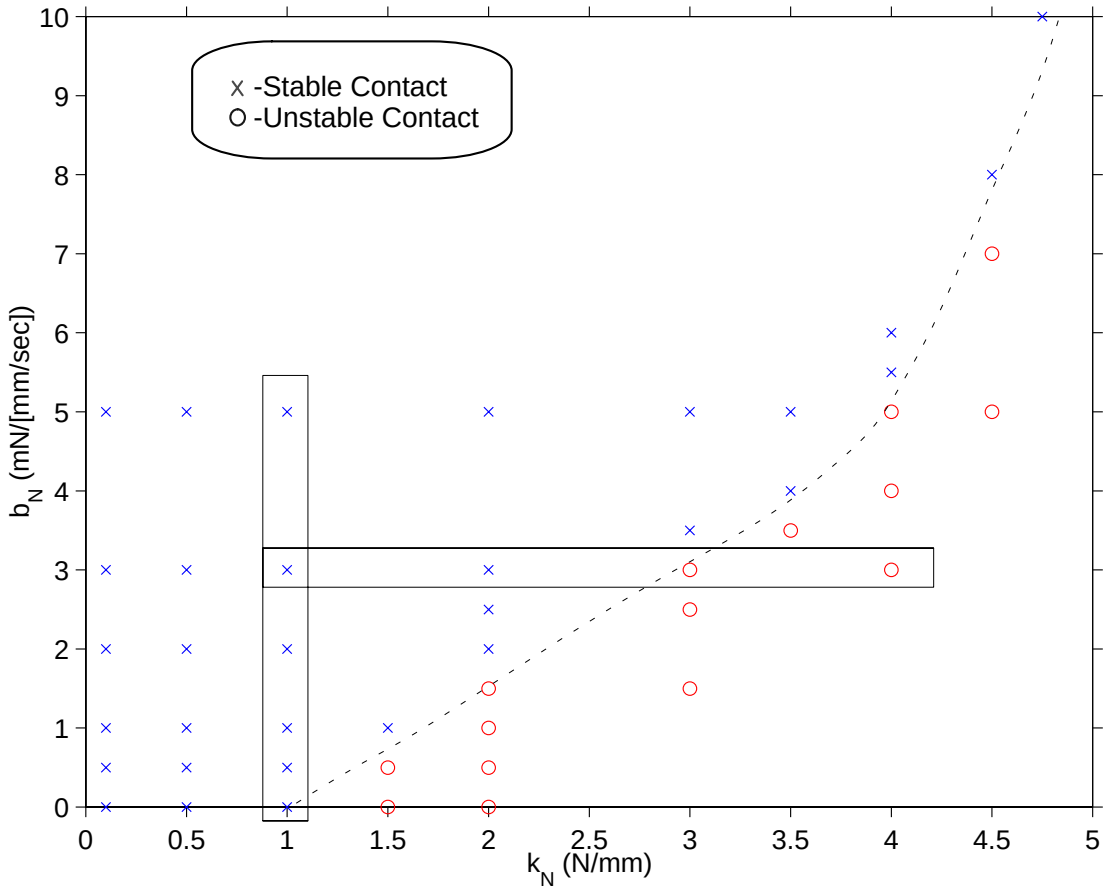

Figure 5.3: Contact (in)stability for various stiffness/damping gains

‘‘stable’’/‘‘unstable’’ binary decision for each gain pair. The results of this experiment are shown in Figure 5.3.

Two types of gain pairs were chosen for more thorough experimentation: one set with constant stiffness (k_N) and variable damping (b_N), the other set with constant damping and variable stiffness. The gain pair values chosen for the G^1 experiment are shown in Figure

Table 5.1: Selected gain pairs for G^1 discontinuity experiment

k_N (N/mm)	1.0	1.0	1.0	1.0	1.0	2.0	2.5	3.0	3.5	4.0
b_N (mN/[mm/sec])	0.0	1.0	2.0	3.0	5.0	3.0	3.0	3.0	3.0	3.0
Constant k_N	×	×	×	×	×					
Constant b_N				×		×	×	×	×	×

5.3 as regions enclosed by either a horizontal or vertical box. The actual gain pair values used are shown in Table 5.1.

5.5.2 Experiment setup

Eleven graduate students (8 male, 3 female) were used as volunteer test operators in the G^1 discontinuity experiment. The performance metric for this experiment was the distance between the true *A/B* intersection location, (x_i, y_i) and the operator's estimated location, (x_v, y_v) on the surface. The operator indicated the estimated location for each trial of the experiment using signaling button held in the opposite hand.

A factorial experiment was constructed which consisted of all possible combinations of the discontinuity magnitude as shown in (5.10) and the gain pairs as shown in Table 5.1. Thus each test operator was presented with (10 gain pairs) × (11 Φ values) = 110 trials, for a total of 1210 trials across 11 test operators. For each operator, the specific ordering of the 110 trials was randomized.

Each operator placed the tip of the index finger of the dominant hand onto the FHD contact point; a small piece of elastic was used to keep the fingertip in contact with the FHD at all times. The signaling button was used twice for each trial: once to start the trial and once to signal that the operator's best estimate of the discontinuity location was at the current fingertip location. A time limit of 30 seconds was placed on each trial. In addition, the operator was instructed to move to an extreme position in the FHD workspace if no discontinuity was perceptible to signal this condition. Extreme positions and the 30-second timeout were treated identically in terms of data analysis. Operators were informed that some of the trials would have undetectable discontinuities. However, no indication was given to them regarding the number expected to be undetectable.

A ‘‘traffic-light’’ display was used during the experiments to indicate the state of the experiment system. A green ‘‘ready’’ light indicated that the system was ready to begin the next trial while a yellow ‘‘in progress’’ light indicated that a trial was in progress and a red ‘‘overload’’ light indicated that the operator was pushing too hard against the haptic surface. Short audio beeps were generated when the state of the system changed (i.e., due to a button press or a timeout) and a continuous tone was generated when an overload condition existed until the applied forces were reduced to preset maximum values. The maximum forces were software limited to 1.1N in all directions due to actuator thermal limitations and gravity preload.

As a test operator traces the surface with a fingertip, a small high-speed change in the force vector occurs at the discontinuity. These changes were observed to produce a very small clicking sound from the actuators under some conditions. For this reason, operators were made to wear sound-reduction headphones to remove the possibility of audio cues for the discontinuity location being given to the operator during the trials.

A five-trial training set was first presented to each operator to familiarize them with the test environment and the operation of the signalling button. This was repeated as necessary until the operator felt comfortable with the test environment. Only then was each operator allowed to begin the set of 110 randomized experiment trials. A visual simulation of the haptic environment was available to the operator during the training set; no visual feedback was given during the actual experiment trials. Each test operator was allowed to rest as desired between experiment trials and short (~1-2 minute) rest periods were required after each 30 trials. Approximately 30-40 minutes was needed for each operator to go through all 110 trials.

We are interested in performance (accuracy in locating the discontinuities) as a function of discontinuity magnitude (Φ) and also the stiffness and damping gain values (k_N

and b_N respectively). Since the test operators were allowed to signal that no discontinuity was perceptible, a second performance measure, called ‘‘confidence’’ is also introduced into our analysis. The confidence value for a given experiment condition is defined as the number of test operators who thought they could perceive a discontinuity under those particular conditions.

The test results may be divided into two groups according to whether the control gain pair of a given trial is one of the constant stiffness or constant damping values. These two groups are considered separate sub-experiments for the purposes of analysis in the following two sections.

5.5.3 Results: Variable Stiffness Sub-Experiment

Figure 5.4 contains a contour plot of the confidence values for various stiffness (k_N) values (see Table 5.1) and discontinuity (Φ) values [see (5.10)] for a single damping value [$b_N = 3.0$ mN/(mm/sec)]. Confidence values could range from 11 (all subjects thought that they perceived a discontinuity) to 0 (no subject thought a discontinuity could be perceived); the actual values ranged from 11 to 4 for this experiment.

The discontinuity angle on the x-axis is the value Φ shown in Figure 5.1. It varies from 174° to 186° as detailed in (5.10). A vertical dashed line at $\Phi = 180°$ indicates where the discontinuity is non-existent. Points in this plot representing relatively small

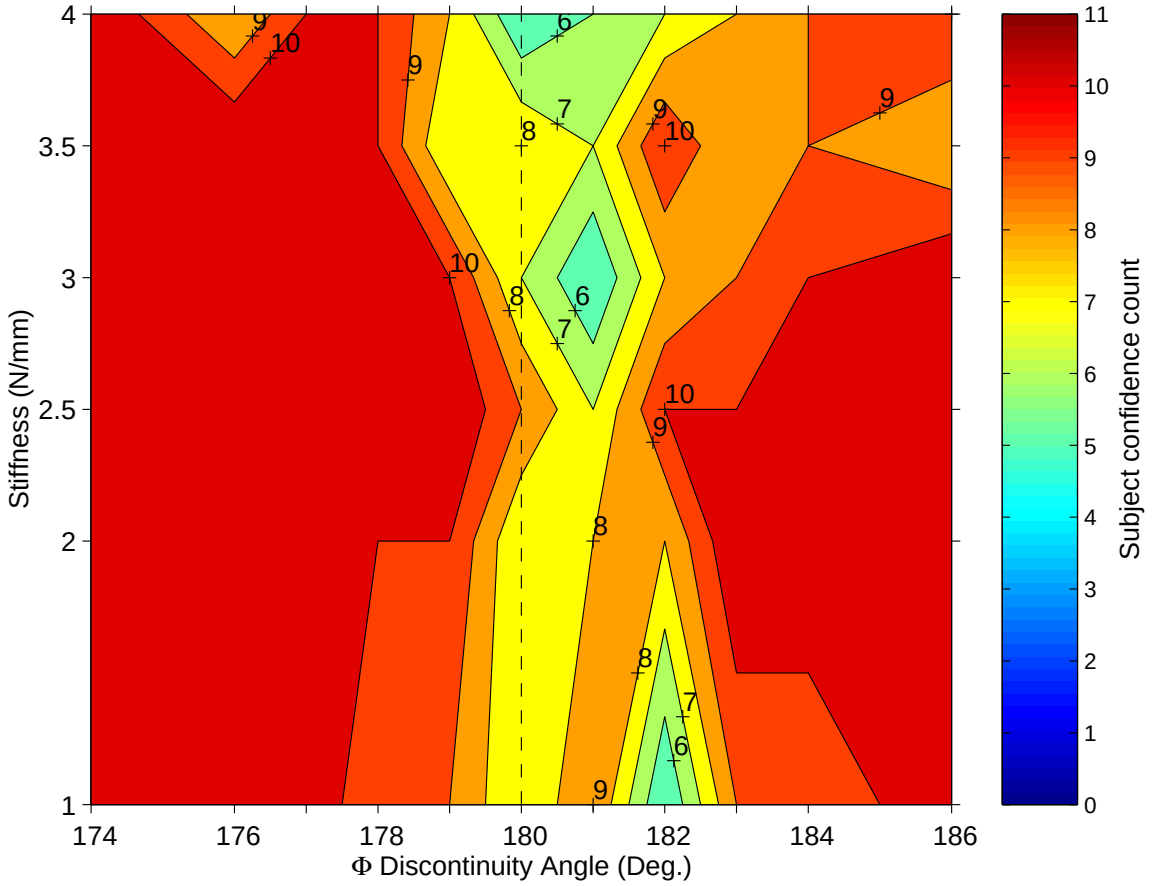

Figure 5.4: Operator confidence for variable stiffness sub-experiment

discontinuities near this 180° line will presumably be harder to detect. Values to the left side of the line are concave while values to the right are convex. For a given stiffness value (y-axis), the confidence has values of 11 (100% confidence) at the more extreme discontinuities (174° and 186°) and decreases to as low as 5 near the non-existent discontinuity at 180°. However, as the stiffness varies from 1 to 4 N/mm, the region of lower confidence is most narrow at the middle stiffness values (near 2.5 N/mm) and is wider at both the lower and higher stiffness values−giving the contour plot somewhat of a vertical, hourglass-like shape. At the highest stiffness values, however, the confidence values never reach 11 even at the most extreme discontinuities--giving the hourglass shape a somewhat vertically asymmetric appearance. The plot shows an interesting horizontal asymmetry as well: the hourglass shape is centered at about 181°, a 1° offset from the 180° position where the discontinuity is nonexistent.

Figure 5.5 contains a contour plot of the mean position error (mm) for all eleven subjects in locating the discontinuities. Note that this data only considers trials where the test operators thought that they were actually perceiving a discontinuity. This plot shows contours at error values of 1 to 10 mm; we consider errors larger than 10 mm to be failed detections since the random location of the actual discontinuity only varied ±10mm in this experiment and since the operators consistently were able to locate discontinuities to an accuracy of less than 3mm at the some of the more extreme discontinuity values (174° and 186°).

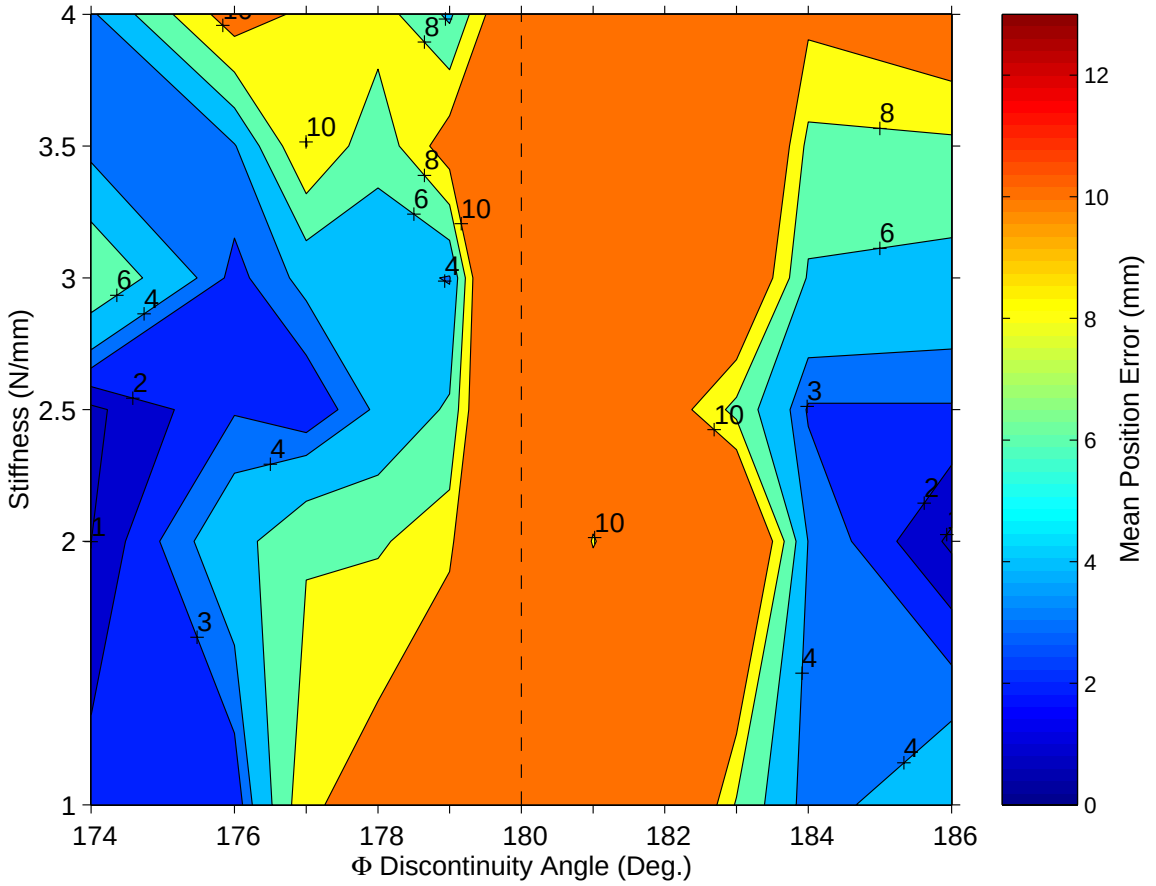

Figure 5.5: Operator mean error for variable stiffness sub-experiment

This plot shows much of same hourglass-like contours as the confidence plot (Figure 5.4) with the entire central region exceeding the 10mm error threshold and performance increasing at the more extreme discontinuity values. At the lower stiffness values (1-2.5 N/mm), the error was 1-4 mm at the extreme discontinuity values; however a clear improvement in accuracy is seen as the stiffness increases from 1 to 2.5 N/mm as the lower valued error contours reach further inwards towards the middle band of consistently high error. As the stiffness continues to increase from 2.5 to 4 N/mm, the accuracy decreases again, but at the higher values near 4 N/mm, the error is quite high (near 10 mm) even at the more extreme discontinuity values--especially at the convex extreme (186°). The

same horizontal bias in mean position error is present as in the previous plot: the region of highest error (≥10mm) is centered at about 181°.

5.5.4 Results: Variable Damping Sub-Experiment

Figure 5.6 contains a contour plot of the confidence values for various damping (b_N) values (see Table 5.1) and discontinuity (Φ) values [see (5.10)] for a single stiffness value [$k_N = 1.0$ N/mm]. The plot shows high confidence values (11) at all damping values where $\Phi \leq 178°$ and nearly as high value (10 or 11) for all $\Phi \geq 183°$. As with the confidence plot from the stiffness sub-experiment (Figure 5.4), a central vertical band of

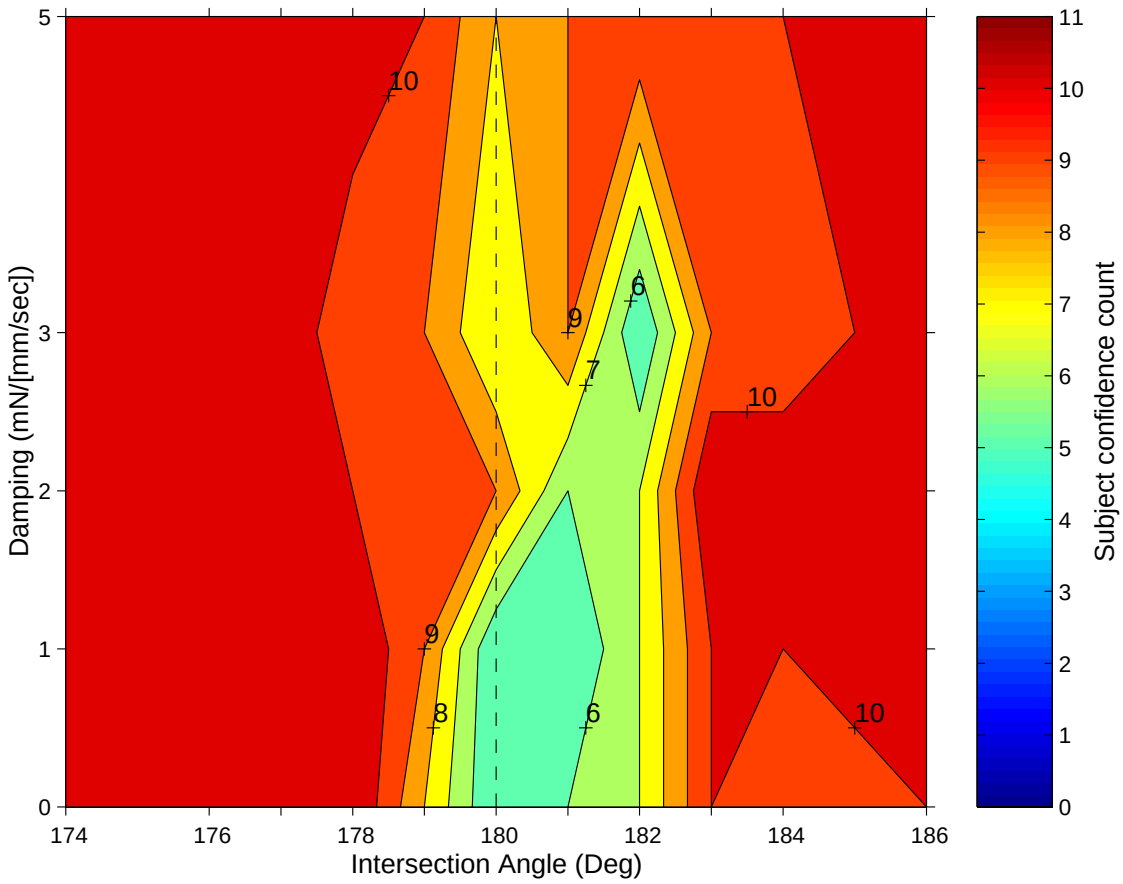

Figure 5.6: Operator confidence for variable damping sub-experiment

lower confidence exists, centered approximately at $\Phi = 181°$; however, this band does not have as clear an hourglass shape as that of Figure 5.4.

Figure 5.7 contains a contour plot of the mean position error (mm) for all eleven subjects in locating the discontinuities, using the same damping (b_N)and discontinuity (Φ) values as the previous confidence plot (Figure 5.6). Like the mean-error plot in the variable stiffness experiment (Figure 5.5), this plot shows contours only at error values between 1 to 10 mm; we consider errors larger than 10 mm to be failed detections since the random location of the actual discontinuity only varied ±10mm in this experiment and since the operators consistently were able to locate discontinuities to an accuracy of less than 3mm at the some of the more extreme discontinuity values (174° and 186°).

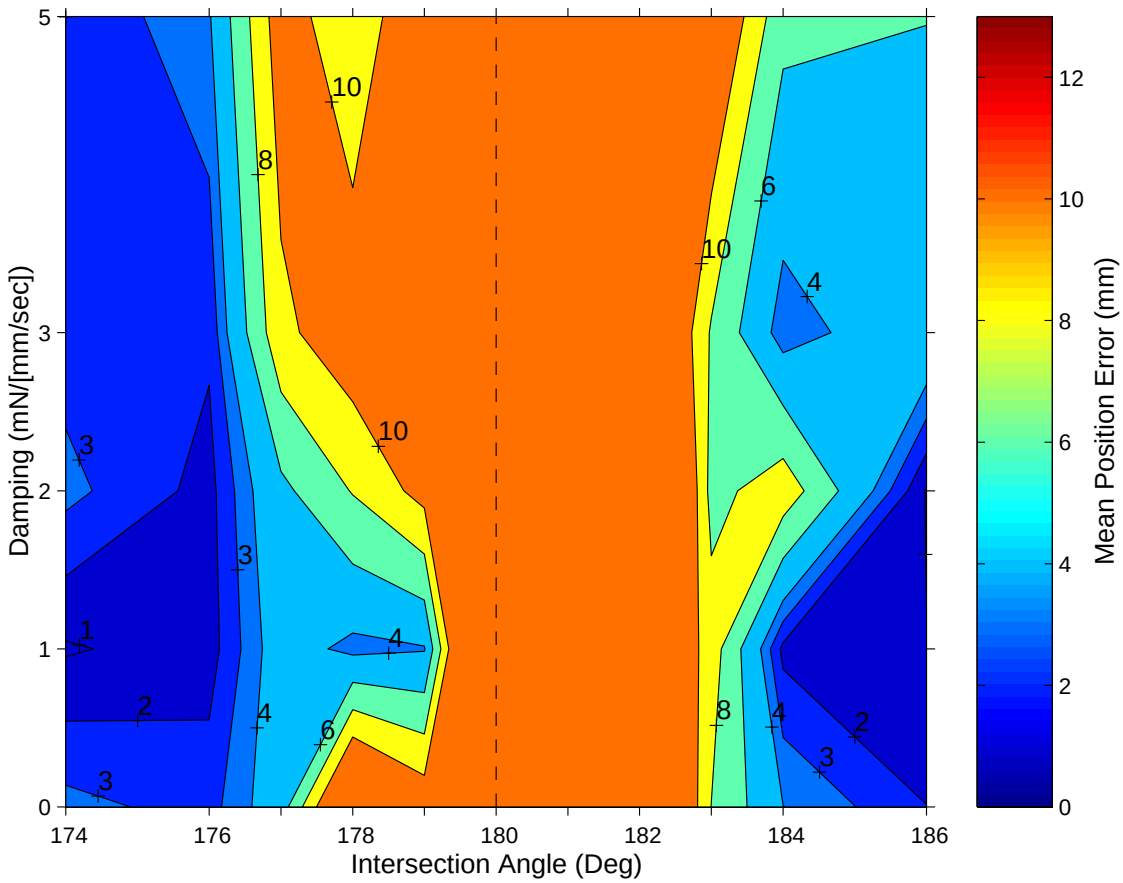

Figure 5.7: Operator mean error for variable damping sub-experiment

As with the variable stiffness sub-experiment, there is an indication that an optimal value exists--this time for the damping parameter--which maximizes the ability to accurately locate small discontinuities. In this case, the best damping value appears to be somewhere between 1.0 and 2.0 mN/(mm/sec). This plot also indicates the operator confidence and mean error have the same bias towards more confidence and accuracy on the concave instead of convex discontinuities.

A central vertical band of high position error is present in this plot for all Φ in the range, $178° \leq \Phi \leq 183°$--except at damping values between 1 and 2 mN/[mm/sec] where the region of high error narrows on the left side to about 179°. For the higher magnitude concave discontinuities at $\Phi \leq 176°$, the error is consistently less than 3mm; errors for higher magnitude convex discontinuities at $\Phi \geq 184°$ have somewhat larger errors (≤ 6 mm) with the exception of the region centered at the damping value of 1mN/[mm/sec].

5.6 SECOND EXPERIMENT: 2ND-ORDER DISCONTINUITIES

Our second experiment studies how well humans perceive G^2 discontinuities with a haptic display on a planar (2D) surface. A G^2 discontinuity in our haptic environment corresponds to an instantaneous change in curvature. Thus, the haptic environment shown in Figure 5.1 was configured so that the two arcs were always tangent (i.e., G^1 continuous) while different curvatures were selected. The angular extent of each arc (ext_A and ext_B in Figure 5.1) was chosen for each trial so that the total length of the two arcs was a constant 75mm. A physical analog of this experiment is a single 75mm piece of wire bent in different shapes for each trial: the total length of the wire remains unchanged, but the shape and location of the wire will vary for each trial.

The arc radii used in this experiment were chosen according to the ratiometric and scale relations shown in Table 5.2. The word, ‘‘scale’’ is used here to indicate the radius

of the smallest of the two arcs; as the scale increases for a constant radius ratio, the radius of both arcs increases, but we indicate this effect using the size of the smallest arc.

Table 5.2: Arc radii ratios and scales used in G^2 discontinuity experiment

	Scale [Radius of smallest arc (mm)]		
Radius Ratio	20	40	80
1:1	–	40:40	–
1:1.5	20:30	40:60	80:120
1:2	20:40	40:80	80:160
1:4	20:80	40:160	80:320
1:8	20:160	40:320	80:640
1:16	20:320	40:640	80:1280

A factorial experiment using these radii and scale values was constructed using the values in Table 5.2 as treatment levels in this two factor experiment. For 15 of the 16 treatments shown in Table 5.2, six trials were conducted for each test operator, using all combinations of the two possible orderings of the arc pair and three different random positions for the intersection point, (x_i, y_i) along the surface. These random positions were grouped into three separate 10mm-wide regions, centered at 1/3, 1/2, and 2/3 of the total length of the surface; these regions are shown as R_1, R_2, and R_3 respectively in Figure 5.8, and a uniform random distribution was used to chose locations in each of these regions. In the 16th treatment, for radius ratio of 1:1, only three trials were conducted for each test operator--one for each of the three regions since the ordering of the two arcs was immaterial. Thus there were $(15\times6)+(1\times3) = 93$ trials per test operator.

For each trial, the tangent angle, ϕ_A was randomly chosen (uniform distribution) over the range of ±30°. The other tangent angle, ϕ_B was constrained by the relation, $\phi_B = \phi_A + 180°$ to enforce the G^1 continuity requirement for this experiment. The intersection point, (x_i, y_i) was also located randomly (uniform distribution) over a limited range

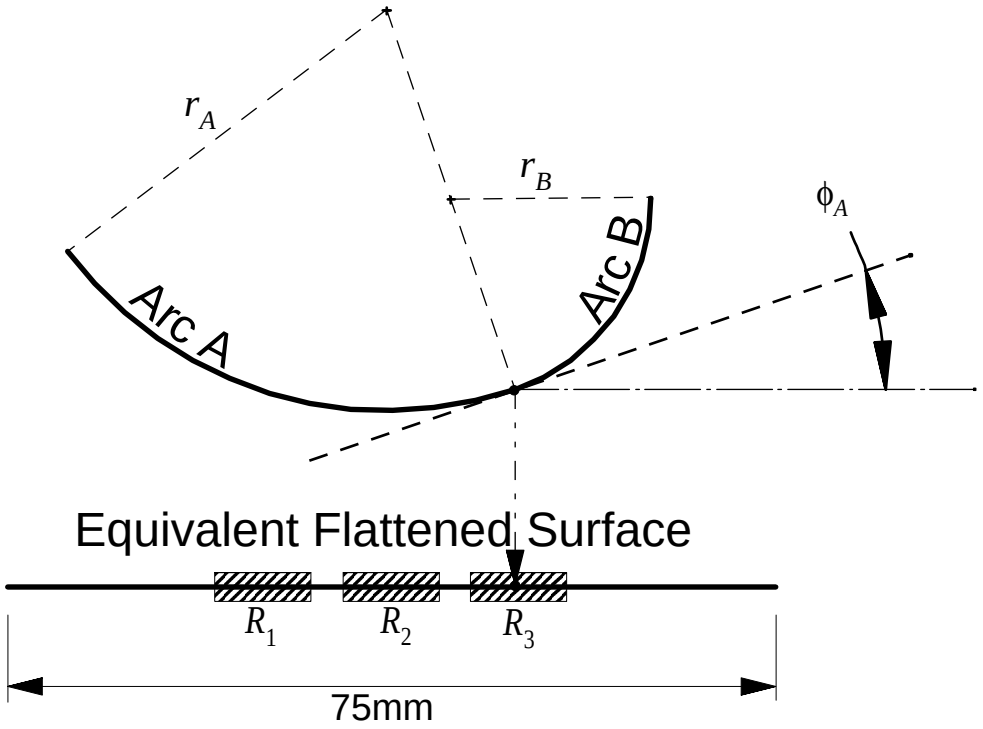

Figure 5.8 Haptic environment for second experiment

in x (±10mm) and y (±5mm) near the center of the FHD reachable workspace. These randomizations were done to avoid giving the operator any positional or slope cues to the G^2 discontinuity.

5.6.1 Experiment setup

Eleven graduate students (9 male, 2 female) were used as volunteer test operators in this G^2 discontinuity experiment. Like the G^1 experiment, the performance metric for this experiment was the distance between the actual and perceived location of the G^2 discontinuity. Again, a signaling button and ‘‘traffic light’’ was used by each test operator as discussed in the previous experiment to start each trial and then end the trial when the discontinuity had been located. The same protocol of enforcing a 30 second timeout and allowing the operator to indicate that no discontinuity could be perceived was used for this experiment.

Each test operator was presented with all 93 trials in a separately randomized order after an 8-trial training sequence to familiarize the operator with the haptic environment and the use of the signalling button. As with the previous experiment, visual simulation feedback was available during the training sequence only.

5.6.2 Results

In this experiment, we are interested in observing how the effects of radii ratio and scale affect the ability of operators to locate the G^2 discontinuity. We begin the results by looking at the operator confidence over the range of 16 treatments. Figure 5.9 shows the operator confidence as a percentage of all 66 trials at each treatment level. A value of 100% indicates that all 11 operators thought they detected a discontinuity on all 6 trials at each level. A plot of confidence vs. curvature ratio (not shown) showed no consistent trend in confidence as the curvature ratio increased from 1.5:1 to 16:1. The plot of confidence vs. scale (smallest radius, Figure 5.9) showed a more distinct trend, however. Five lines are plotted, one for each of the five different ratios. All five lines show a general trend from high confidence values (95% to 100%) at the smallest scale (20mm),

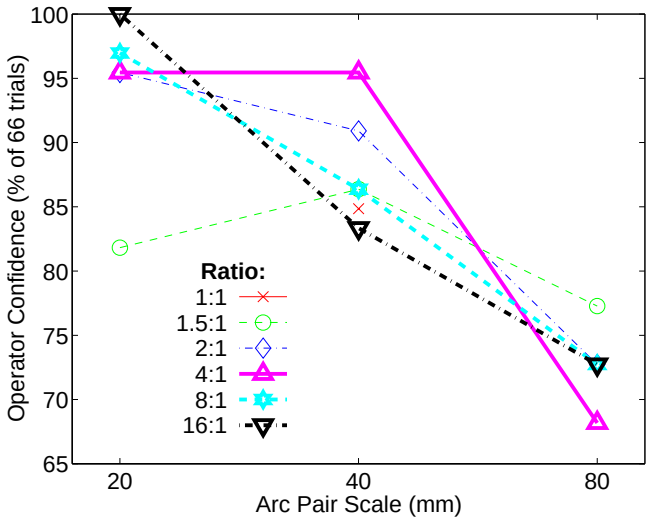

Figure 5.9: Operator confidence values for all treatment levels

decreasing roughly linearly down to 68% to 78% at a scale of 80mm. Some variation is visible however: the confidence for the 1.5:1 ratio (‘o’ points in Figure 5.9) is much lower than the rest (~82%) and the 4:1 ratio (‘Δ’ points, Figure 5.9) shows a nearly flat ~95% confidence at the 20mm and 40mm scales before dropping to 68% at the 80mm scale. Also, the single ‘x’ symbol located on the 40mm scale value shows that operators had a 84% confidence in the presence of a curvature discontinuity when there was no discontinuity to detect! This indicates that significant perceptual bias may be present in this subjective measure (confidence) of discontinuity detection.

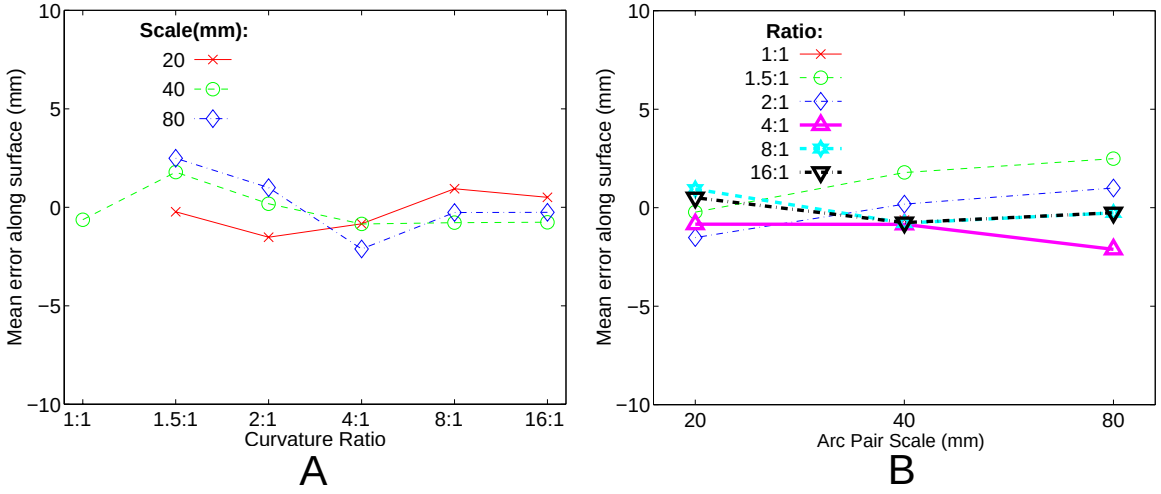

Figure 5.10: Mean position error in detection of discontinuities

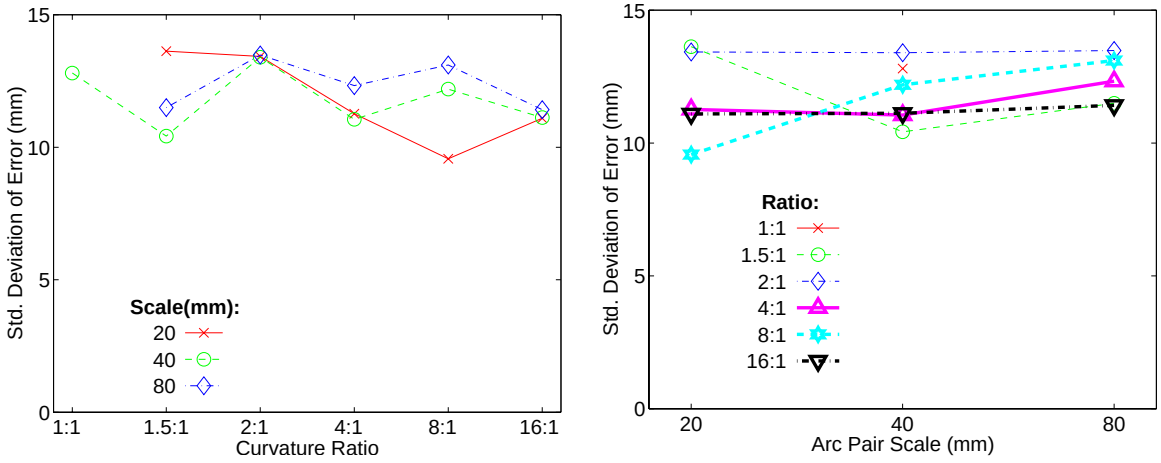

Figure 5.11: Standard Deviation of position detection errors

Figure 5.10A and Figure 5.10B show the mean error values for this experiment. Note that, as with the mean error plots in previous G^1 experiment, only the values where the operator indicated that a discontinuity could be detected were used to compute these means. The first plot (Figure 5.10A) shows mean error vs. curvature ratio while the second one (Figure 5.10B) shows mean error plotted vs. curvature scale. However, in both of these plots, no discernible trend is visible: the mean error for each treatment group was within about ±2mm of zero. The standard error values (standard deviation of the experiment means) for the 66 trials at each treatment level are shown in Figure 5.11A and Figure 5.11B, which use the same X-axes as Figure 5.10A and Figure 5.10B respectively. The variances also show no significant trend over either curvature ratio or curvature scale, ranging from 10 to 14mm.

5.6.2.1 Curvature-biased detection of discontinuities

A more careful study of the data revealed an important bias in the means. A new set of ‘‘curvature-biased’’ error data was computed using a negative value to indicate errors towards the smaller arc and positive values to indicate errors towards the larger radius arc. A histogram of the curvature-biased errors (Figure 5.12) showed that the errors were

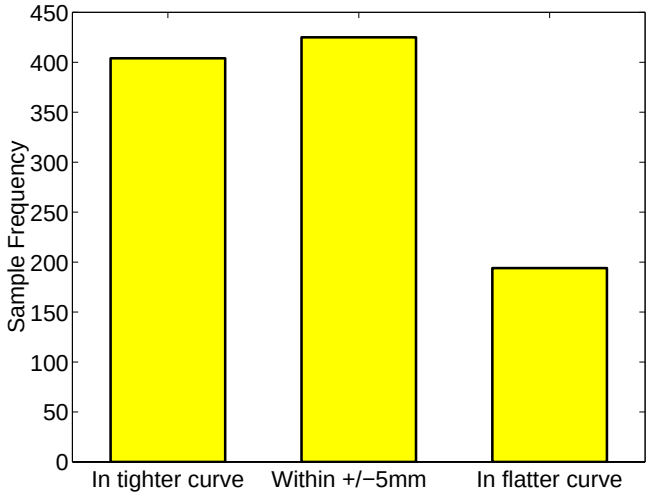

Figure 5.12: Histogram of perceived position relative to discontinuity

biased towards the smaller-radius arcs. This bias was hidden in Figure 5.10 since both arc orderings were used equally for each treatment level.

Figure 5.13A and Figure 5.13B show curvature-biased mean errors for several of the treatment levels. A plot of curvature-biased error vs. curvature ratio (Figure 5.13A) shows a general trend towards an increasing error at larger curvature ratios. This trend is most clear at a scale of 40mm (‘‘o’’ points in Figure 5.13A) with a mean error near 0mm for the 1:1 ratio and decreasing gradually to about -5mm (i.e., 5mm into the smaller radius arc) for the 8:1 and 16:1 curvature ratios. However, it is less obvious for the 80mm and 20mm arc scale values (‘‘×’’ and ‘‘◊’’ points respectively in Figure 5.13A). Figure 5.13B shows the same mean error data plotted vs. arc scale with 5 lines for each of the 5 different arc ratio values tested at all 3 scale values. Here, the trend is less obvious.

It is difficult to visually judge the significance of these trends--i.e., the effects of arc ratio and arc scale on mean error. The apparent bias values range from 0 to -5, but the standard error on these measurements is 10-12 mm, which makes the significance of these effects questionable. Analysis of variance (ANOVA) indicates that neither interaction effects or the main effect of the arc scale are significant to the 95% threshold, but the arc ratio main effect is significant at the 95% threshold.

5.6.3 Discussion

In the G^1 discontinuity experiment, discontinuities of varying magnitude were presented to each test operator for a variety of different haptic display stiffness and damping control parameters. In the variable stiffness sub-experiment, we held damping to a constant value and varied the stiffness parameter over several values. We found that both operator confidence in detecting the discontinuities (Figure 5.4) and the mean operator error in locating the discontinuities (Figure 5.5) show a general pattern of higher confidence and better accuracy at the larger discontinuities (further from the 180° value of Φ). However, the confidence values even at the larger discontinuities are reduced for higher stiffnesses. A likely explanation is that the larger contact instabilities occurring at the higher stiffnesses mask the operator's ability to feel the discontinuity. This explanation is supported by the fact that the FHD exhibited significant contact instabilities at stiffness values greater than 3N/mm (Figure 5.3).

Our impedance model for surface contact (Figure 5.2) generates forces proportional to both surface depth of penetration (spring) and to surface penetration velocity (damper). Thus, as the stiffness, $k_N \rightarrow 0$, we would expect at least some reduction in ability to detect

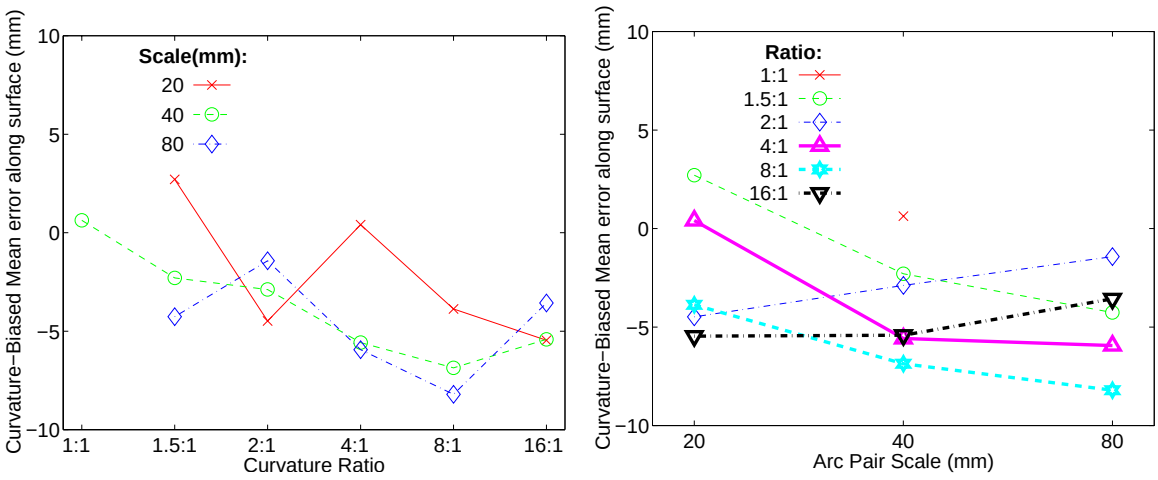

Figure 5.13: Curvature-biased mean position error in detection of discontinuities

discontinuities. It isn't clear that operators would be incapable of detecting *all* discontinuities when $k_N = 0$ since we still have some damping feedback (i.e., $b_N \neq 0$). However, some preliminary experimentation using various damping values with zero stiffness indicated that detection under these conditions would be extremely difficult.

The combination of instability at higher stiffness values and inability to accurately locate the discontinuities at very low stiffness values implies that there may be an optimum stiffness value where these two effects are minimized. In both the confidence and mean error plots (Figure 5.4 and Figure 5.5 respectively) of our constant-damping [$b_N = 3.0$ mN$/$(mm$/$sec)] sub-experiment, the most narrow ''neck'' of both confidence and accuracy occurs at the 2.5 N/mm stiffness value. This value should then be near-optimum for locating these G^1 discontinuities. Presumably, this optimum value will differ for different damping values as well as for different haptic display systems since each system will have its own stability properties.

The apparent horizontal bias in both plots that centers the region of lowest-confidence/highest-error on $\Phi = 181°$ was an unexpected result of these experiments. This bias implies that, on average, the convex discontinuities are slightly more difficult to locate than the concave ones. One potential explanation for this is that the concave discontinuities provide a natural potential energy minimum which tends to hold the finger in the correct position, while the convex discontinuities have the opposite effect. An analogy to this is a marble rolling along the same surface: it is easy to get the marble to stay at a concave discontinuity, but nearly impossible to get it to balance at the peak of a convex discontinuity.

In the variable damping sub-experiments, the same G^1 discontinuities were presented as with the variable stiffness sub-experiment, but the damping parameter was varied

while the stiffness parameter was held constant ($k_N = 1.0\ N/\text{mm}$). In this case, both the confidence plot and the mean-error plot show some effect of varying damping values. The best ability to locate small discontinuities occurs with damping values near 1.0 mN/[mm/sec]. However, this effect does not appear to be as pronounced as that of the variable stiffness sub-experiment. Other published results have shown some improvement in the ‘‘perceptual hardness’’ of a surface when some amount of damping is added [29]. However, high damping values tend to cause high-frequency contact instabilities. As with stiffness, there appears to be there an optimum value for damping from which higher damping causes instabilities that interfere with perception of discontinuities and lower damping reduces the perceived hardness of the surface.

In the G^2 discontinuity experiments, the operators were presented with a variety of surfaces consisting of two intersecting arcs that were G^1 continuous while having different radii of curvature. We discovered that the ability to locate the discontinuity was slightly biased (0-5mm) towards the smaller of the two arcs and that this bias was affected somewhat by curvature ratio (more bias at larger ratios) but not significantly by curvature scale (radius of smallest arc). It is interesting to note that the operator confidence values seem to indicate the opposite: the perception of the presence of a discontinuity was strongly affected by arc scale (Figure 5.9) and not by curvature ratio.

5.7 CONCLUSIONS AND FUTURE WORK

Overall, we found that operators were able locate G^1 discontinuities to an accuracies of 3-4mm at the some of the more extreme discontinuity values ($\Phi \leq 176°$ and $\Phi \geq 185°$) and were able get the same accuracy for even smaller discontinuity values (178° and 184°) if the control parameters were tuned to optimal values. However, since the device performance will affect perception abilities, it is expected that other haptic display devices would exhibit somewhat different ranges of discontinuity values for these levels of

accuracy. In contrast, the ability to sense and locate G^2 discontinuities seems quite poor: while the mean error in locating the discontinuities were typically in the range of -5 to 0 mm (on our curvature-biased scale), the standard error at each treatment level for 45 observations was 10 to 12 mm.

Some of the implications of these observations are:

1. Haptically rendered objects with curved surfaces are often approximated by facets. In order for the surface to be perceived as smooth, the amount of surface gradient change at the facet boundaries should be kept below the G^1 detection threshold (approximately [-1°,+3°] in our experiments). This threshold will most likely vary for different haptic simulation systems but could be determined on a per-device basis with a short one-time test procedure. However, keeping the gradient changes small may imply that an increased number of facets must be used in the simulation model which, in turn, may have a negative impact on the computational performance of the haptic simulation system, requiring a trade-off between these two factors.
2. In an environment containing complex curved surfaces, operators will, in general, have poor performance in detecting and/or locating G^2 discontinuities. This may be an important limitation in a situation like a visual/haptic CAD system where the user is attempting to locate and select the point of intersection of two curves such as the boundary between a surface and a fillet in a typical CAD geometry scenario.
3. In designing and evaluating haptic devices, the ability to perceive G^1 and G^2 discontinuities may be an important part of the design or selection criteria. It may be that the perception of these features is undesirable, putting an upper limit on the haptic simulation system's rendering fidelity. Or it may be that perception of these features are important, motivating the development of even higher performance haptic simulation systems.

Future experiments in the area of discontinuity perception would be helpful in gaining a better understand how this perception varies with different haptic devices. Furthermore, it would be useful to perform similar experiments on the fingertip using physical surfaces instead of haptically rendered surfaces since this would give a better idea of how much of the current performance observations and limitations are due to the limitations of the simulation process and how much are due to perceptual limitations of the human finger-tip.

Notes to Chapter 5

[1] Adams, R.J. and B. Hannaford, *A Two-Port Framework for the Design of Unconditionally Stable Haptic Interfaces*, Proc. 1998 IEEE/RSJ International Conference on Intelligent Robots and Systems (IROS-98), November, 1998.

[2] Appelle, S., *Visual and Haptic Angle Perception in the Matching Task*, American Journal of Psychology, Vol. 84(4), pp. 487-499, 1971.

[3] Barsky, B.A. and T.D. DeRose, *Geometric continuity of parametric curves: Three equivalent characterizations*, Computer Graphics & Applications, Vol 9(6), pp. 60-68, 1989.

[4] Buttolo, P., *Characterization of Human Pen Grasp with Haptic Displays*, Ph.D Dissertation, University of Washington, Dept. of Electrical Engineering, June, 1996.

[5] Colgate, J.E., M.C. Stannley J.M. Brown, *Issues in the Haptic Display of Tool Use*, Proc. 1995 IEEE/RSJ International Conference on Intelligent Robots and Systems (IROS-95), Vol. 3, pp. 140-145, August, 1995.

[6] Collins, J.J., T.T. Imhoff and P. Grigg, *Noise-enhanced tactile sensation*, Nature, Vol 383, p. 770, October, 1996.

[7] Crewdson, J. and O.L. Zangwill, *A Note on Tactual Perception in a Blind Subject*, British Journal of Psychology, Vol. 30, pp. 224-229, 1940.

[8] Davidson, P.W. and T.T. Whitson, *Haptic Equivalence Matching of Curvature by Blind and Sighted Humans*, J. of Experimental Psychology, Vol. 102(4), pp. 687-690, 1974.

[9] Davidson, P.W., *Haptic Judgments of Curvature by Blind and Sighted Humans*, J. of Experimental Psychology, Vol. 93(1), pp. 43-55, 1972.

[10] do Carmo, M.P., *Differential Geometry of Curves and Surfaces*, Prentice-Hall, 1976.

[11] Easton, R.D. and M. Falzett, *Finger pressure during tracking of curved contours: Implications for a visual dominance phenomenon*, Perception & Psychophysics, Vol. 24(2), pp. 145-153, 1978.

[12] Farin, G, *Curves and Surfaces for Computer-Aided Geometric Design*, 4th Ed., Academic Press, Inc., San Diego, 1997.

[13] Goodnow, J.J., B. Baum and P. Davidson, *A haptic error: Skew in a symmetrical curve*, Perception & Psychophysics, Vol 10(4A), pp. 253-256, 1971.

[14] Goodwin, A.W. and H.E. Wheat, *Human tactile discrimination of curvature when contact area with skin remains constant*, Experimental Brain Research, Vol. 88, pp. 446-450, 1992.

[15] Goodwin, A.W., K.T. John and A.H. Marceglia, *Tactile discrimination of curvature by humans using only cutaneous information from the fingerpads*, Experimental Brain Research, Vol 86, pp. 663-672, 1991.

[16] Gordon, I.E. and V. Morison, *The haptic perception of curvature*, Perception & Psychophysics, Vol. 31(5), pp. 446-450, 1982.

[17] Gordon, J and C. Ghez, *Muscle Receptors and Spinal Reflexes: The Stretch Reflex*, in ‘‘Principals of Neural Science,’’ 3rd Ed., E.R. Kandel, J.H. Schwartz, and T.M. Jessell, editors, Printice Hall, 1991.

[18] Gouraud, H, *Continuous Shading of Curved Surfaces*, IEEE Transactions on Computers, Vol. 20(6), pp. 623-628, 1971.

[19] Hanley, C. and D.P. Goff, *Size Constancy in Extended Haptic Space*, Perception & Psychophysics, Vol 15(1), pp. 97-100, 1974.

[20] Hogan, N., Kay-B.A., E.D. Fasse and F.A. Mussa-Ivald, *Haptic Illusions: Experiments on Human Manipulation and Perception of ‘Virtual Objects’*, Cold Spring Harbor Symposia on Quantitative Biology, Volume 55, pp. 925-931, 1990.

[21] Hunter, I.M.L., *Tactile-Kinaesthetic Perception of Straightness in Blind and Sighted Humans*, Quarterly Journal of Experimental Psychology, Vol. 6, pp. 149-154, 1954.

[22] Kappers, A.M.L. and J.J. Koenderink, *Haptic unilateral and bilateral discrimination of curved surfaces*, Perception, Vol 25, pp. 739-749, 1996.

[23] Kappers, A.M.L., J.J. Koenderink and I. Lichtenegger, *Haptic identification of curved surfaces*, Perception & Psychophysics, Vol 56(1), pp. 53-61, 1994.

[24] Kappers, A.M.L., J.J. Koenderink and S.F. tePas, *Haptic discrimination of doubly curved surfaces*, Perception, Vol 23, pp. 1483-1490, 1994.

[25] Klatzky, R.L., S.J. Lederman and D.E. Matula., *Haptic Exploration in the Presence of Vision*, J. of Experimental Psychology: Human Perception and Performance, Vol. 19(4), pp. 726-743, 1993.

[26] Klatzky, R.L., J.M. Loomis, S.J. Lederman, H. Wake and N. Fujita, *Haptic identification of objects and their depictions*, Perception & Psychophysics, Vol. 54(2), pp. 170-178, 1993.

[27] Klatzky, R.L., Lederman-S.J. and J.D. Balakrishnan, *Task-Driven extraction of object contour by human haptics: Part 1*, Robotica, Vol. 9(1), pp. 43-51, 1991.

[28] Klatzky, R.L., S.J. Lederman and J.D. Balakrishnan, *Task-Driven extraction of object contour by human haptics: Part 2*, Robotica, Vol. 9(2), pp. 179-188, 1991.

[29] Lawrence, D.A., L.Y. Pao, M.A. Salada and A.M. Dougherty, *Quantitative Experimental Analysis of Transparency and Stability in Haptic Interfaces*, Proc. Fifth Annual Symposium on Haptic Interfaces for Virtual Environment and Teleoperator Systems, ASME Winter Annual Meeting, Atlanta, GA, November 1996.

[30] Lakatos, S. and L.E. Marks, *Haptic Underestimation of Angular Extent*, Perception, Vol. 27, pp 737-754, 1998.

[31] Lederman, S.J. and R.L. Klatzky, *Relative Availability of Surface and Object Properties During Early Haptic Processing*, Journal of Experimental Psychology: Human Perception and Performance, Vol. 23(6_, pp. 1680-1707, 1997.

[32] Mortenson, M.E., *Geometric Modeling*, 2nd Ed., Wiley Computer Publishing, New York, 1997.

[33] Pawluk, D.T.V. and R.D. Howe, *A Holistic Model of Human Touch*, Proc. of the 5th Annual Computational Neuroscience Society Meeting, Boston, MA, July 1996.

[34] Pont, S.C., A.M.L. Kappers and J.J. Koenderink, *Anisotropy in haptic curvature and shape perception*, Perception, Vol 27(5), pp. 573-589, 1998.

[35] Pont, S.C., A.M.L. Kappers and J.J. Koenderink, *Haptic curvature discrimination at several regions of the hand*, Perception & Psychophysics, Vol. 59(8), pp. 1225-1240, 1997.

[36] Rabischong, P., *Physiology of Sensation*, in ‘‘The Hand,’’ Raoul Tubiana, Ed., Vol. I, pp. 441-467, ISBN 0-7216-8907-8, W.B. Saunders Co., Philadelphia, 1981.

[37] Reed, C.L., *Perceptual dependence for shape and texture during haptic processing*, Perception, Vol. 23(3), pp. 349-366, 1994.

[38] Ruben, E., *Haptische Untersuchungen*, Acta Psychol., Vol 1(3), pp. 285-330, 1936.

[39] Schaeffer, R.L. and J.T. McClave, *Probability and Statistics for Eingineers*, 2nd Ed., Duxbury Press, Boston, 1986.

[40] Shimoga, K.B., *A Survey of Perceptual Feedback Issues in Dexterous Telemanipulation: PartII. Finger Touch Feedback*, Proceedings IEEE Virtual Reality Annual International Symposium (VRAIS), pp. 271-279, Seattle WA, 1993.

[41] Srinivasan, M.A. and R.H. LaMotte, *Encoding of Shape in the Responses of Cutaneous Mechanoreceptors*, in ‘‘Information Processinng in the Somatosensory System,’’ Eds. O. Franzen and J. Westman, Wenner-Gren International Symposium Series, MacMillan Press, 1991.

[42] Stanley, G., *Adding and Averaging Angles: Comparison of Haptic-Visual and Visual-Visual Information Integration*, Acta Psychologica, Vol. 38, pp. 331-336, 1974.

[43] Tan, H.Z., *Identification of Sphere Size using the Phantom: Towards a Set of Building Blocks for Rendering Haptic Environment*, Proc. ASME Dynamic Systems and Control Division, pp. 197-203, 1997.

[44] Veltkamp, R.C., *Survey of Continuities of Curves and Surfaces*, Computer Graphics forum, Vol. 11(2), pp. 93-112, 1992.

[45] Vogels, I.M.L.C., A.M.L. Kappers and J.J. Koenderink, *Haptic aftereffect of curved surfaces*, Perception, Vol. 25, pp. 109-119, 1996.

[46] West, A.M. and M.R. Cutkosky, *Detection of Real and Virtual Fine Surface Features with a Haptic Interface and Stylus*, Proc. ASME Dynamic Systems and Control Division, pp. 159-165, 1997.

[47] Wu, J.L., H. Sasaki and S. Kawamura, *A Tactile Display Using Human Characteristic of Sensory Fusion*, Proc. IEEE Int'l Conference on Robotics & Automation, Leuven, Belgium, May, 1998, pp. 693-698.

[48] Zilles, C.B., and J.K. Salisbury, *A Constraint-based God-object Method for Haptic Display*, Proc. 1995 IEEE/RSJ International Conference on Intelligent Robots and Systems (IROS-95), Vol. 3, pp. 146-151, August, 1995.

CHAPTER 6: CONCLUSION

6.1 SUMMARY OF WORK

This dissertation details the development a fingertip haptic display and its use in perceptual experiments that measured the human ability to detect geometric discontinuities in haptically simulated surfaces. In Chapter 2, a new technique was presented for computing the reachable workspace of a serial mechanism whose kinematic parameters have stochastically defined elements. In this workspace representation, each point is characterized by the probability of that point being in the reachable workspace of the stochastic mechanism. This technique may be used in modeling the reachable workspace of humans to help improve the design of the human interfaces to a wide range of devices such as automobile interiors or haptic display devices.

In Chapter 3, the reachable workspace of the human fingers relative to the metacarpophalangeal (MCP) joint was computed using the technique detailed in Chapter 2, combined with anthropometric survey data on the human hand. This result provides useful information to the designer of a haptic display for the fingertip.

Using the fingertip workspace information presented in Chapter 3, the kinematic design optimization of a fingertip haptic display mechanism was presented in Chapter 4. The optimization process maximized the product of the mechanism reachable workspace and the minimum force over all directions over the entire workspace. This approach provides a scale-independent optimization of the worst-case force output capability of the mechanism which can then be scaled to best fit a target reachable workspace. The kinematic design of an extended fivebar planar mechanism was thus optimized for the reachable workspace of the human fingers. In Appendix A, details are given on the physical

implementation of this kinematic design, which used custom-designed actuators and embedded position sensors. A US patent application regarding several novel features of this design has been filed by the University of Washington and a commercial license of the technology is already in place.

In Chapter 5, psychophysical experiments are presented which explore the human ability to perceive and locate first-order and second-order geometric surface discontinuities. The results indicate that the perception of first order discontinuities and the ability to locate them within a few mm is quite good for discontinuities as small as a few degrees. However, the perception and ability to locate second-order discontinuities is less acute: radius of curvature changes as large as 16:1 had standard errors on the order of 10-12mm. These results will help to better understand the limitations of the human ability to perceive these haptically rendered surface features and may have useful impacts on the design of haptically enabled CAD design tools and other haptic simulation applications.

6.2 FUTURE WORK

For stochastic workspace analysis, interesting challenges remain in the application of this technique to mechanisms whose operational space has dimensionality greater than two. Specifically, data storage and representation, computing requirements, and visualization techniques would need to be developed for larger operational spaces. These techniques would perhaps be most interesting and immediately useful to apply to computing the stochastic reachable workspace of the human arm−perhaps even in conjunction with the entire human torso.

In mechanism design, the technique presented in Chapter 4 optimizes a scale independent criterion which considers the size, but not the shape, of the mechanism reachable workspace. It would be useful to attempt to extend this technique to include shape and thus perhaps produce a design better optimized to some target workspace.

As mentioned at the end of Chapter 4, it would be useful to extend the current geometric discontinuity perception results to other haptic display systems. Also useful would be similar psychophysical experiments that use physical mock-ups of these surfaces, which would improve our understanding where these limitations are incurred: at the haptic simulation system or in the sensory system of the human fingertip, or perhaps some combination of these two alternatives.

BIBLIOGRAPHY

Adams, R.J. and B. Hannaford, *A Two-Port Framework for the Design of Unconditionally Stable Haptic Interfaces*, Proc. 1998 IEEE/RSJ International Conference on Intelligent Robots and Systems (IROS-98), November, 1998.

Alameldin, T., N. Badler, and T. Sobh, *An Adaptive and Efficient System for Computing the 3-D Reachable Workspace*, Proceedings of the IEEE International Conference of System Engineering, pp. 503-506, Pittsburgh, PA, USA, August, 1990.

American Academy of Orthopaedic Surgeons, *Joint Motion: Methods of Measuring and Recording*, American Academy of Orthopaedic Surgeons, Chicago, 1965.

American Medical Association, *Guides to the Evaluation of Permanent Impairment*, ed. 3, American Medical Association, Chicago, 1988.

Appelle, S., *Visual and Haptic Angle Perception in the Matching Task*, American Journal of Psychology, Vol. 84(4), pp. 487-499, 1971.

Barsky, B.A. and T.D. DeRose, *Geometric continuity of parametric curves: Three equivalent characterizations*, Computer Graphics & Applications, Vol 9(6), pp. 60-68, 1989.

Buchholz, B., T.J. Armstrong, and S.A. Goldstein, *Anthropometric data for describing the kinematics of the human hand*, Ergonomics, vol. 35, no. 3, pp. 261-273, 1992

Buttolo, P. and B. Hannaford, *Pen Based Force Display for Precision Manipulation of Virtual Environments*, Proceedings VRAIS-95, pp. 217-225, Raleigh, NC, March 1995.

Buttolo, P., *Characterization of Human Pen Grasp with Haptic Displays*, Ph.D Dissertation, University of Washington, Dept. of Electrical Engineering, June, 1996.

Buttolo, P., D.Y. Hwang and B. Hannaford, *Hard Disk Actuators for Mini-Teleoperation*, Proceedings of the SPIE Telemanipulator and Telepresence Technologies Symposium, pp. 55-61, Boston, MA, October 1994

Case, K. and M. Porter, *SAMMIE can cut out the prototypes in ergonomic design*, Control and Instrumentation, vol. 12, no. 1, pp. 28-29, January, 1980.

Chua, L.O., C.A. Desoer, E.S. Kuh, *Linear and Non-linear Circuits*, McGraw-Hill, New York, 1987.

Colgate, J.E., M.C. Stannley J.M. Brown, *Issues in the Haptic Display of Tool Use*, Proc. 1995 IEEE/RSJ International Conference on Intelligent Robots and Systems (IROS-95), Vol. 3, pp. 140-145, August, 1995.

Collins, J.J., T.T. Imhoff and P. Grigg, *Noise-enhanced tactile sensation*, Nature, Vol 383, p. 770, October, 1996.

Craig, J..J., *Introduction to Robotics Mechanics and Control*, 2nd Edition, Addison-Wesley, Reading Massachusetts, 1989.

Crewdson, J. and O.L. Zangwill, *A Note on Tactual Perception in a Blind Subject*, British Journal of Psychology, Vol. 30, pp. 224-229, 1940.

Davidson, P.W. and T.T. Whitson, *Haptic Equivalence Matching of Curvature by Blind and Sighted Humans*, J. of Experimental Psychology, Vol. 102(4), pp. 687-690, 1974.

Davidson, P.W., *Haptic Judgments of Curvature by Blind and Sighted Humans*, J. of Experimental Psychology, Vol. 93(1), pp. 43-55, 1972.

Derby, S., *The Maximum Reach of a Revolute Jointed Manipulator*, Mechanism and Machine Theory, vol. 16, no. 3, pp. 255-261, 1981.

do Carmo, M.P., *Differential Geometry of Curves and Surfaces*, Prentice-Hall, 1976.

Easton, R.D. and M. Falzett, *Finger pressure during tracking of curved contours: Implications for a visual dominance phenomenon*, Perception & Psychophysics, Vol. 24(2), pp. 145-153, 1978.

Ebert-Uphoff, E. and G.S. Chirikjian, *Efficient Workspace Generation for Binary Manipulators with Many Actuators*, Journal of Robotic Systems, vol. 12, no. 6, pp. 383-400, 1995.

Fabiani, L., G. Burdea, N. Langrana, and D. Gomez, *Human Interface Using the Rutgers Master II Force Feedback Interface*, Proc. IEEE VRAIS'96, pp. 54-59, 1996.

Farin, G, *Curves and Surfaces for Computer-Aided Geometric Design*, 4th Ed., Academic Press, Inc., San Diego, 1997.

Garrett, J.W., *The Adult Human Hand: Some Anthropometric and Biomechanical Considerations*, Human factors, Vol. 13, No. 2, pp. 117-131, 1971.

Goodnow, J.J., B. Baum and P. Davidson, *A haptic error: Skew in a symmetrical curve*, Perception & Psychophysics, Vol 10(4A), pp. 253-256, 1971.

Goodwin, A.W. and H.E. Wheat, *Human tactile discrimination of curvature when contact area with skin remains constant*, Experimental Brain Research, Vol. 88, pp. 446-450, 1992.

Goodwin, A.W., K.T. John and A.H. Marceglia, *Tactile discrimination of curvature by humans using only cutaneous information from the fingerpads*, Experimental Brain Research, Vol 86, pp. 663-672, 1991.

Gordon, I.E. and V. Morison, *The haptic perception of curvature*, Perception & Psychophysics, Vol. 31(5), pp. 446-450, 1982.

Gordon, J and C. Ghez, *Muscle Receptors and Spinal Reflexes: The Stretch Reflex*, in ''Principals of Neural Science,'' 3rd Ed., E.R. Kandel, J.H. Schwartz, and T.M. Jessell, editors, Printice Hall, 1991.

Gouraud, H, *Continuous Shading of Curved Surfaces*, IEEE Transactions on Computers, Vol. 20(6), pp. 623-628, 1971.

Gruenbaum, P.E., W.A. McNeely, H.A. Sowizral, T.L. Overman, and B.W Knutson, *Implementation of Dynamic Robotic Graphics For a Virtual Control Panel*, Presence, Vol. 6(1), pp. 118-126, February, 1997.

Hanley, C. and D.P. Goff, *Size Constancy in Extended Haptic Space*, Perception & Psychophysics, Vol 15(1), pp. 97-100, 1974.

Hannaford, B. and S.C. Venema, *Kinesthetic Displays for Remote and Virtual Environments*. In W. Barfield and T.A. Furness III, editors, Virtual Environments and Advanced Interface Design, chapter 10. Oxford University Press, 1995.

Hansen, J.A., K.C. Gupta and S.M.K. Kazerounian, *Generation and Evaluation of the Workspace of a Manipulator*, International Journal of Robotics Research, vol. 2, no. 3, pp. 22-31, Autumn, 1983.

Hayward, V., J. Choksi, G. Lanvin and C. Ramstein, *Design and Multi-Objective Optimization of a Linkage for a Haptic Interface*, In J. Lenarcic and B. Ravani, editors, ‘‘Advances in Robot Kinematics and Computational Geometry,’’ pp. 359-368. Kluwer Academic Publishers, 1995.

Hodges, M., *It Just Feels Right*, Computer Graphics World, pp. 48.56, October, 1998.

Hogan, N., *Impedance Control: An Approach to Manipulation: Part I - Theory*, Journal of Dynamic Systems, Measurement, and Control, vol. 107, pp. 1-7, 1985.

Hogan, N., Kay-B.A., E.D. Fasse and F.A. Mussa-Ivald, *Haptic Illusions: Experiments on Human Manipulation and Perception of ‘Virtual Objects’*, Cold Spring Harbor Symposia on Quantitative Biology, Volume 55, pp. 925-931, 1990.

Hogan, N., *Part II: Impedance Control: An Approach to Manipulation: Implementation*, Journal of Dynamic Systems, Measurement, and Control, vol. 107, pp. 8-16, 1985.

Hogan, N., *Part III: Impedance Control: An Approach to Manipulation: Applications*, Journal of Dynamic Systems, Measurement, and Control, vol. 107, pp. 17-24, 1985.

Hunter, I.M.L., *Tactile-Kinaesthetic Perception of Straightness in Blind and Sighted Humans*, Quarterly Journal of Experimental Psychology, Vol. 6, pp. 149-154, 1954.

Iwata, H., *A Six Degree-of-freedom Pen-based Force Display*, Proc. Fifth International Conference on Human-Computer Interaction, vol, 2, pp. 651-656, Orlando, FL, USA, Aug. 1993.

Jau, B.B., *Man-Equivalent Telepresence Through Four Fingered Human-Like Hand System*, Proc. International Conference on Robotics and Automation, San Francisco, USA, pp. 1520-1532, May, 1986.

Kappers, A.M.L. and J.J. Koenderink, *Haptic unilateral and bilateral discrimination of curved surfaces*, Perception, Vol 25, pp. 739-749, 1996.

Kappers, A.M.L., J.J. Koenderink and I. Lichtenegger, *Haptic identification of curved surfaces*, Perception & Psychophysics, Vol 56(1), pp. 53-61, 1994.

Kappers, A.M.L., J.J. Koenderink and S.F. tePas, *Haptic discrimination of doubly curved surfaces*, Perception, Vol 23, pp. 1483-1490, 1994.

Kayis, B. and P.A. Iskander, *A three-dimensional human model for the IBM/CATIA system*, Applied Ergonomics, vol. 25, no. 6, pp. 395-397, 1994.

Kingsley, E.C., N.A. Schofield, and K. Case, *SAMMIE: A Computer Aid for Man Machine Modelling*, Computer Graphics, vol. 15, no. 3, pp. 163-169, August, 1981.

Kircanski, M., *Kinematic Isotropy and Optimal Kinematic Design of Planar Manipulators and a 3-DOF Spatial Manipulator*, International Journal of Robotics Research, 15(1):61-77, 1996.

Klatzky, R.L., J.M. Loomis, S.J. Lederman, H. Wake and N. Fujita, *Haptic identification of objects and their depictions*, Perception & Psychophysics, Vol. 54(2), pp. 170-178, 1993.

Klatzky, R.L., Lederman-S.J. and J.D. Balakrishnan, *Task-Driven extraction of object contour by human haptics: Part 1*, Robotica, Vol. 9(1), pp. 43-51, 1991.

Klatzky, R.L., S.J. Lederman and D.E. Matula., *Haptic Exploration in the Presence of Vision*, J. of Experimental Psychology: Human Perception and Performance, Vol. 19(4), pp. 726-743, 1993.

Klatzky, R.L., S.J. Lederman and J.D. Balakrishnan, *Task-Driven extraction of object contour by human haptics: Part 2*, Robotica, Vol. 9(2), pp. 179-188, 1991.

Korien, J.U, *A Geometric Investigation of Reach*, Ph.D Dissertation, Department of Computer Science, University of Pennsylvania, 1984. (Republished under the same title by MIT Press, Cambridge, MA, 1984, ISBN 0-262-11104-7).

Kumar, A. and K.J. Waldron, *The Workspaces of a Mechanical Manipulator*, Journal of Mechanical Design, 103:665-672, July 1981.

Kumar, A. and M.S. Patel, *Mapping the Manipulator Workspace Using Interactive Computer Graphics*, International Journal of Robotics Research, vol, 5, no. 2, pp. 122-130, Summer, 1986.

Kurtz, R. and V. Hayward, *Multiple-Goal Kinematic Optimization of a Parallel Shperical Mechanism with Actuator Redundancy*, IEEE Transactions on Robotics and Automation, 8(5):644-651. October, 1992.

Kwan, S.J., Y. Youm, and W.K. Chung, *General Algorithm for Automatic Generation of the Workspace for n-link Planar Redundant Manipulators*, Journal of Mechanical Design, vol. 116, pp. 967-969, September, 1994.

Lakatos, S. and L.E. Marks, *Haptic Underestimation of Angular Extent*, Perception, Vol. 27, pp 737-754, 1998.

Lawrence, D.A., L.Y. Pao, M.A. Salada and A.M. Dougherty, *Quantitative Experimental Analysis of Transparency and Stability in Haptic Interfaces,* Proc. Fifth Annual Symposium on Haptic Interfaces for Virtual Environment and Teleoperator Systems, ASME Winter Annual Meeting, Atlanta, GA, November 1996.

Lederman, S.J. and R.L. Klatzky, *Designing Haptic Interfaces for Teleoperation and Virtual Environments: Should Spatially Distributed Forces be Displayed to the Fingertip?,* Proceedings ASME Dynamic Systems and Control Division, pp. 11-15, 1997.

Lederman, S.J. and R.L. Klatzky, *Relative Availability of Surface and Object Properties During Early Haptic Processing,* Journal of Experimental Psychology: Human Perception and Performance, Vol. 23(6_, pp. 1680-1707, 1997.

Lee, S.H., B-J. Yi and Y.K. Kwak, *Optimal Kinematic Design of an Anthropomorphic Robot Module with Redundant Actuators,* Mechatronics 7(5):443-464, 1997.

Massie, T.H. and J.K. Salisbury, *Probing Virtual Objects with the PHANToM Haptic Interface*, Proc. ASME Winter Annual Meetings, Chicago, 1994.

Mortenson, M.E., *Geometric Modeling,* 2nd Ed., Wiley Computer Publishing, New York, 1997.

Paden, B. and S. Sastry, *Optimal Kinematic Design of 6R Manipulators*, International Journal of Robotics Research, 7(2):43-61, March/April, 1988.

Pawluk, D.T.V. and R.D. Howe, *A Holistic Model of Human Touch*, Proc. of the 5th Annual Computational Neuroscience Society Meeting, Boston, MA, July 1996.

Paynter, H.M., *Analysis and Design of Engineering Systems*, MIT Press, Cambridge, 1961.

Pedretti, L.W., Zoltan, B., *Occupational Therapy: Practice Skills for Physical Dysfunction*, ed. 3, C.V Mosby Co., St. Louis, 1990.

Peebles, P.Z.Jr., *Probability, Random Variables, and Random Signal Principles,* 3rd Ed., McGraw-Hill, New York, NY, 1993.

Pont, S.C., A.M.L. Kappers and J.J. Koenderink, *Anisotropy in haptic curvature and shape perception*, Perception, Vol 27(5), pp. 573-589, 1998.

Pont, S.C., A.M.L. Kappers and J.J. Koenderink, *Haptic curvature discrimination at several regions of the hand*, Perception & Psychophysics, Vol. 59(8), pp. 1225-1240, 1997.

Rabischong, P., *Physiology of Sensation*, in ‘‘The Hand,’’ Raoul Tubiana, Ed., Vol. I, pp. 441-467, ISBN 0-7216-8907-8, W.B. Saunders Co., Philadelphia, 1981.

Rastegar, J. and D. Perel, *Generation of Manipulator Workspace Boundary Geometry Using the Monte Carlo Method and Interactive Computer Graphics*, Transactions of the ASME, vol. 112, pp. 452-454, September, 1990.

Reed, C.L., *Perceptual dependence for shape and texture during haptic processing*, Perception, Vol. 23(3), pp. 349-366, 1994.

Roebuck, J.A., *Anthropometric Methods: Designing to Fit the Human Body*, Human Factors and Ergonomics Society, Santa Monica, CA, 1995.

Ruben, E., *Haptische Untersuchungen*, Acta Psychol., Vol 1(3), pp. 285-330, 1936.

Schaeffer, R.L. and J.T. McClave, *Probability and Statistics for Eingineers*, 2nd Ed., Duxbury Press, Boston, 1986.

Selfridge, R.G., *The Reachable Workarea of a Manipulator*, Mechanism and Machine Theory, 18(2):131--137, 1981.

Shimoga, K.B., *A Survey of Perceptual Feedback Issues in Dexterous Telemanipulation: PartII. Finger Touch Feedback*, Proceedings IEEE Virtual Reality Annual International Symposium (VRAIS), pp. 271-279, Seattle WA, 1993.

Srinivasan, M.A. and R.H. LaMotte, *Encoding of Shape in the Responses of Cutaneous Mechanoreceptors*, in ''Information Processinng in the Somatosensory System,'' Eds. O. Franzen and J. Westman, Wenner-Gren International Symposium Series, MacMillan Press, 1991.

Stanley, G., *Adding and Averaging Angles: Comparison of Haptic-Visual and Visual-Visual Information Integration*, Acta Psychologica, Vol. 38, pp. 331-336, 1974.

Stocco, L.J., S.E. Salcudean and F. Sassani, *Mechanism Design for Global Isotropy with Applications to Haptic Interface*, Proceedings of the ASME Dynamic Systems and Control Division, pp. 115-122, 1997.

Sugimoto, K. and J. Duffy, *Determination of Extreme Distances of a Robot Hand--Part 1: A General Theory*, Journal of Mechanical Design, 103:631-636, July, 1981.

Sugimoto, K. and J. Duffy, *Determination of Extreme Distances of a Robot Hand—Part 1: A General Theory*, Journal of Mechanical Design, vol. 103, pp. 631-636, July 1981.

Sugimoto, K. and J. Duffy, *Determination of Extreme Distances of a Robot Hand—Part 2: Robot Arms with Special Geometry*, Journal of Mechanical Design, vol. 103, pp. 776-783, July 1981.

Tan, H.Z., *Identification of Sphere Size using the Phantom: Towards a Set of Building Blocks for Rendering Haptic Environment*, Proc. ASME Dynamic Systems and Control Division, pp. 197-203, 1997.

Tsai, Y.C.and A.H. Soni, *An Algorithm for the Workspace of a General n-R Robot*, Transactions of the ASME, vol, 105, p. 52-57, March, 1983.

Veltkamp, R.C., *Survey of Continuities of Curves and Surfaces*, Computer Graphics forum, Vol. 11(2), pp. 93-112, 1992.

Vogels, -I.M.L.C., A.M.L. Kappers and J.J. Koenderink, *Haptic aftereffect of curved surfaces*, Perception, Vol. 25, pp. 109-119, 1996.

Wampler, C.W., *Winding Number Analysis of Invertible Workspaces for Redundant Manipulators*, Proceedings of 28th Conference on Decision and Control, pp. 546-569, Los Angeles, CA, Dec. 1990.

West, A.M. and M.R. Cutkosky, *Detection of Real and Virtual Fine Surface Features with a Haptic Interface and Stylus*, Proc. ASME Dynamic Systems and Control Division, pp. 159-165, 1997.

Wu, J.L., Sasaki-H., S. Kawamura, *A Tactile Display Using Human Characteristic of Sensory Fusion*, Proc. IEEE Int'l Conference on Robotics & Automation, Leuven, Belgium, May, 1998, pp. 693-698.

Yang, D.C.H. and T.W. Lee, *On the Workspace of Mechanical Manipulators*, Transactions of the ASME, vol. 105, pp. 62-69, March 1983.

Yoshikawa, T., *Foundations of Robotics*, MIT Press, Cambridge, MA, 1990.

Zilles, C.B., and J.K. Salisbury, *A Constraint-based God-object Method for Haptic Display*, Proc. 1995 IEEE/RSJ International Conference on Intelligent Robots and Systems (IROS-95), Vol. 3, pp. 146-151, August, 1995.

Appendix A: FHD MECHANISM AND CONTROLLER DESIGN

A.1. FUNCTIONAL REQUIRMENTS

The mechanical design of the UW fingertip haptic display (FHD) was based on the following functional requirements:

- Provide haptic feedback to the human fingertip.
- Allow planar fingertip motion due to flexion and extension motion of the finger joints.
- Have a mechanical form factor that allows multiple FHD's to be used simultaneously−one for each of the four fingers of the hand.

These requirements translate into the need for a design which has a very narrow form factor outside of its plane of motion, supports the reachable workspace of human fingers, and has mechanical characteristics such as high stiffness, low mass, and low friction that allow high fidelity haptic simulation.

A.2. DESIGN APPROACH

We decided to base our mechanical design on the planar extended fivebar linkage configuration shown in Figure A.1. This type of linkage is formed by a closed kinematic chain of five joints. Since the angular position of any two joints in this linkage fully constrain the mechanism, the actuators can be placed at the two ‘‘base’’ joints (the base of links l_1 and l_2) which reduces the amount of inertia of the moving part of the mechanism as compared to a typical serial mechanism design. In addition, closed chain kinamatic linkages have relatively high stiffness compared to their serial chain counterparts.

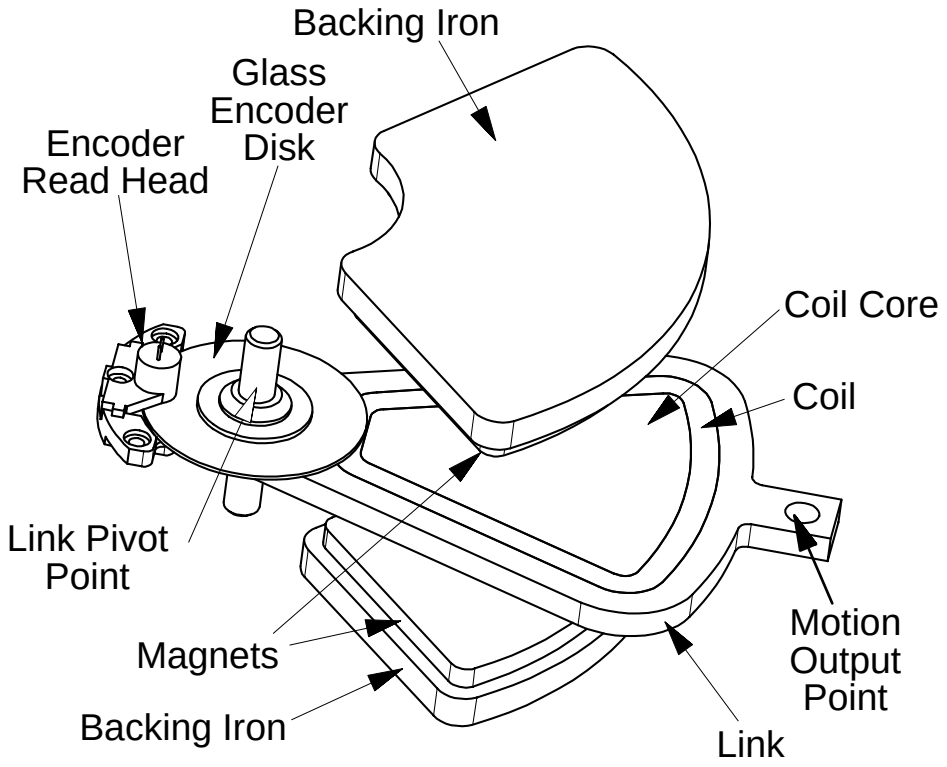

Figure A.3: New Flatcoil Actuator with Embedded Coil and Encoder

Since the embedded coils made some space available behind the bearing, we chose to embed an optical encoder into the link as well. Our approach was to mount the glass encoder disk on the link so that the disk overhangs the back side of the link. This overhanging part of the encoder disk passes through the slot of a encoder read head that may be mounted on the same stationary support structure that supports the link bearings, as shown in Figure A.3. We also chose to use a dual-bearing ‘‘yoke’’ type of design as shown in Figure A.4 for all joints in the fivebar mechanism help improve the stiffness of the mechanism.

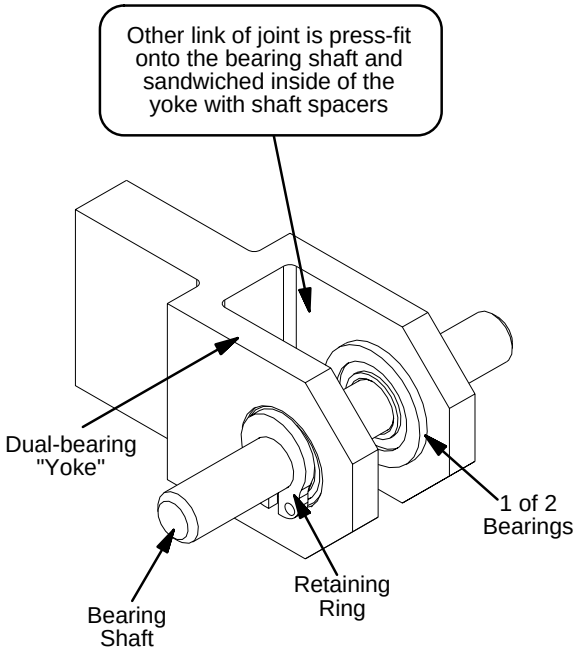

Figure A.4: ‘‘Yoke’’ design for FHD Joints

In summary, the detailed design process was based on four engineering decisions:

1. Use a fivebar linkage with the kinematic design specifications from the optimization process detailed in Chapter 4.
2. Use our new 90° embedded-coil actuators
3. Use an embedded optical encoder for position sensing.
4. Use dual bearing ‘‘yoke’’ configurations for all joints

A.3. DETAILED DESIGN

The detailed design process used the kinematic design parameters shown in Figure 4.4 to implement a compact, dual actuation fivebar mechanism with 90° motion ranges. Most of the detailed mechanical design was performed by a Elgar Matthes, a visiting student from the University of Technology, Dresden. Elger designed the compact base support part which supports the bearings for the l_1 and l_2 links while also supporting the actuator magnets as well as the encoder read heads. He also designed all the remaining links of the

mechanism and selected the off-the-shelf components such as bearings, shafts, spacers, etc.

A line drawing of the complete mechanism is shown in Figure A.6. Most of the custom-designed components of the design were manufactured by a local machine shop (Lebbern Manufacturing, Auburn, WA). The magnets used in this design were custom-manufactured from rare-earth (NeFeB) magnetic material (Crumax 4014) with the help of Crumax Magnetics, Inc. (Elizabethtown, Kentucky). Crumax cut and polished 2-inch squares of the correct thickness (4.0±0.1mm) from a pre-manufactured block of unmag-netized material. These squares were then cut to our curved design profile (see Figure A.5) at the University of Washington using a CNC-based wire-EDM machining process and then shipped back to Crumax to be magnetized.

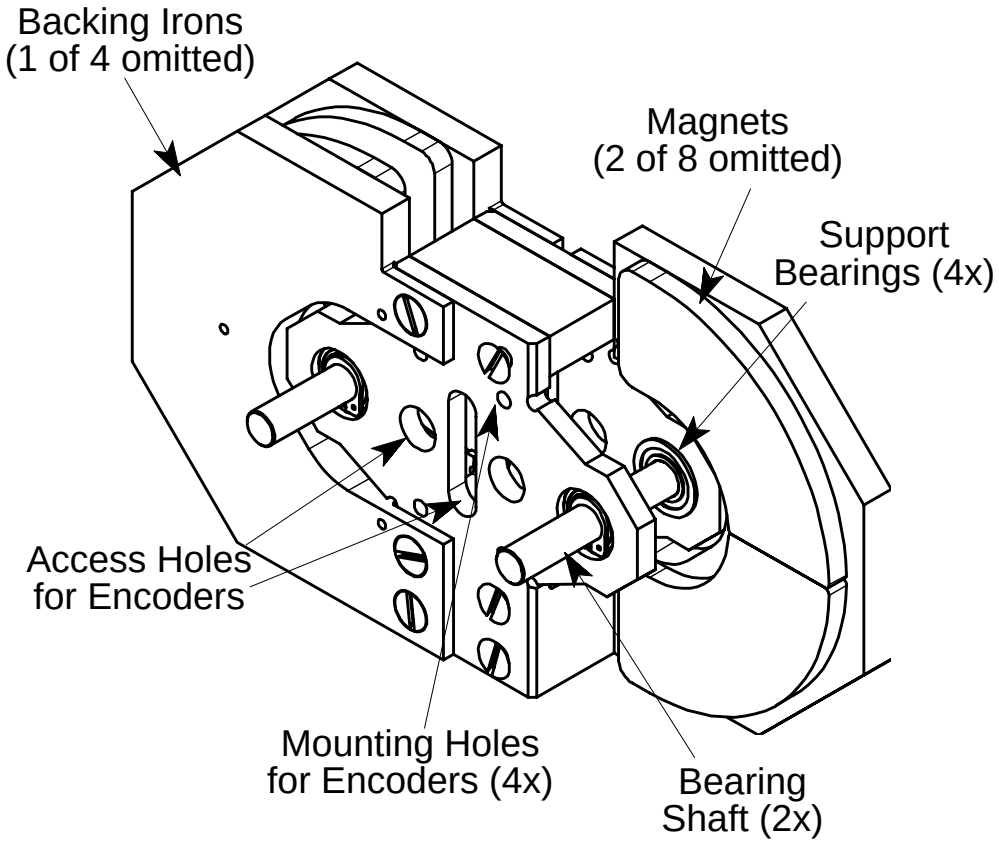

Figure A.5: FHD Main Support Assembly

A.4. ASSEMBLY

The coils were assembled using a special #28-AWG wire (Part# 28-SPT-180 from MWS Wire Industries, Westlake Village, CA) which was coated with an epoxy bond material on top of the enamel normally used to coat magnet wire. After the coils were hand wound on a custom-machined form, they were baked according to the wire specifications to cause the epoxy overcoat to bond the wire into a single solid coil. Each coil was then bonded into its link using a water-activated epoxy cement (Part# OB-600 from Omega Engineering, Stanford, CT) that was selected for both its strength and high termal-conductivity properties.

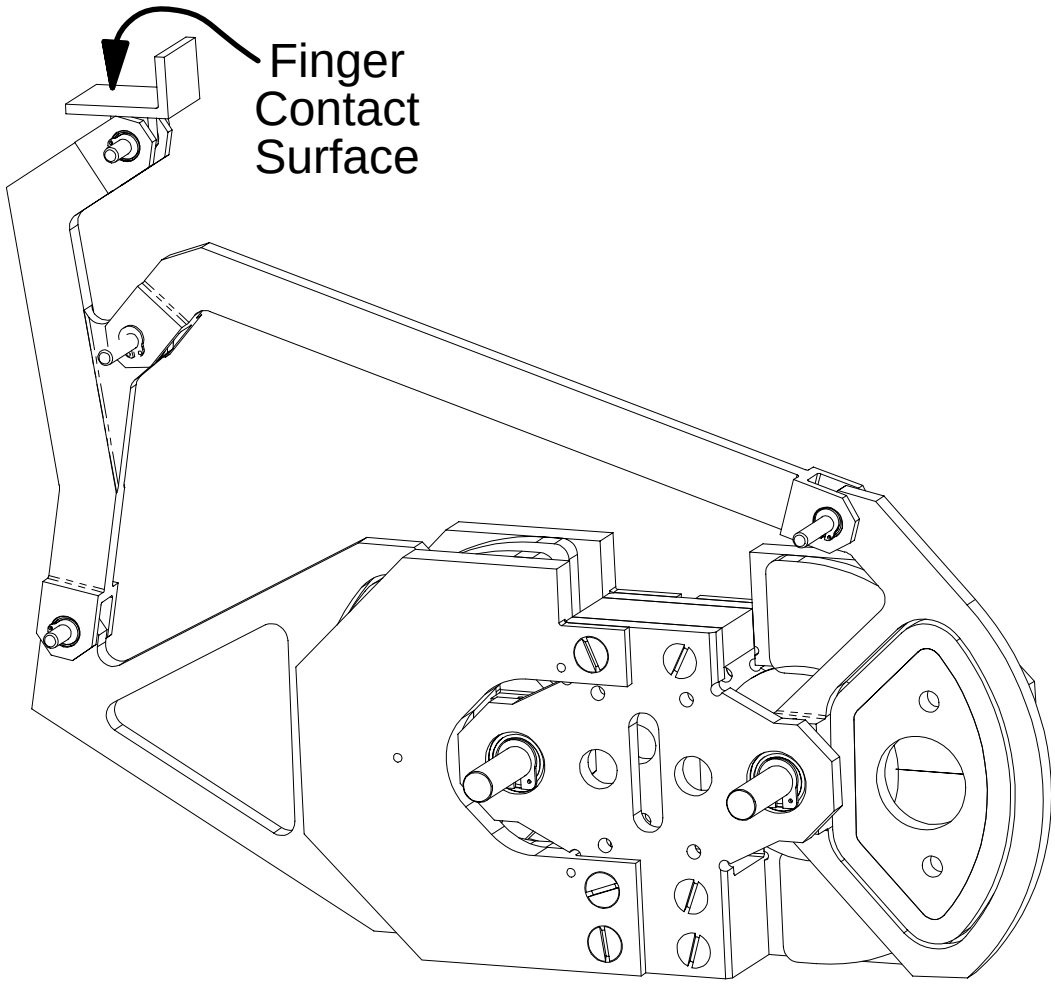

Figure A.6: Complete FHD mechanical assembly

The embedded optical encoders were based on portions of high-resolution (2048-line) analog kit encoders (Part# CP-850 from Computer Optical Products Inc. [COPI], Chatsworth, CA). In our design, we mounted the encoder emitter/read-head assemblies inside of the FHD main support (see Figure A.5) and attached the encoder glass codewheels to each of the two base links as shown in Figure A.3; this design approach turned out the be the most troublesome aspect of the assembly process. The encoder read heads were suspended on a pair of #4-40 screws within a spring-loaded antibacklash setup. We found, however, that this design, as it currently exists, is unable to provide the necessary stability and alignment accuracy (a few 10's of microns) for satisfactory encoder output. Until a different approach can be developed, we decided to instead use externally mounted encoders (COPI Part# CP-200) which connect on the side of the FHD device via an extra-long bearing shaft for each of the two base links.

A.5. CONTROLLER HARDWARE

The FHD controller is implemented using a quad-processor computer system (200MHz Pentium-Pro), as shown in Figure A.7. The analog encoder outputs are used with quadrature-to-digital interpolators (COPI Part# CP-1064) to get high-resolution digital quadrature signals (131072 counts pre revolution or about 364 counts per degree). These encoder signals are passed to an encoder interface IP (''Industry Pak'') module (Model 14 from Tech80, Minneapolis, MN) which, in turn, is mounted on a quad IP module carrier board (Tech80 Model 5641) that is plugged into a standard 16-bit ISA slot in the control computer.

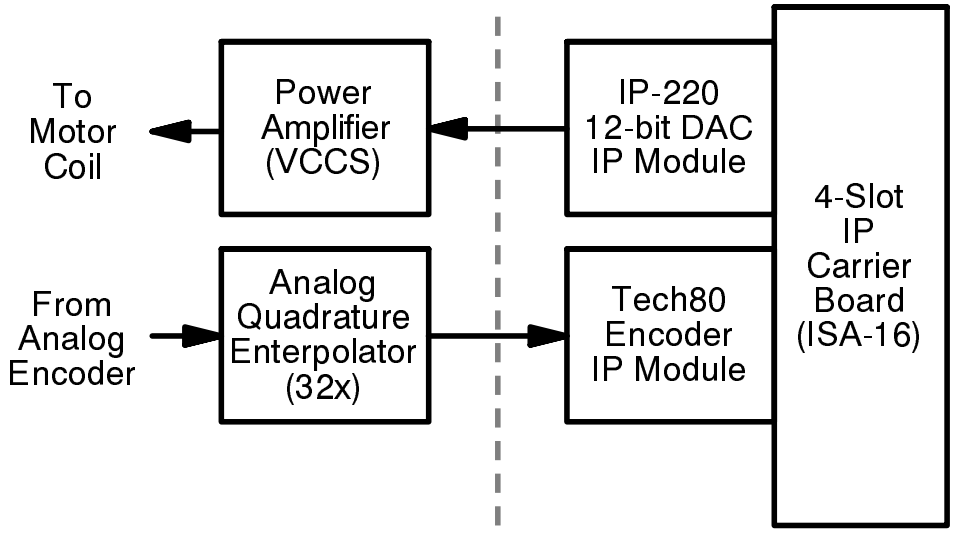

Figure A.7: FHD Controller Block Diagram

A second IP module (Tech80 IP220) contains 12-bit D-to-A converters (DAC's) used to command analog voltages to the FHD motor power amplifiers. These amplifiers are configured as voltage-controlled current sources (VCCS) so that the digitally commanded voltage directly controls motor current (and thus torque) via the DAC's. The power amplifier can drive up to 3 amps through each coil. However, the maximum continuous current that avoids overheating the coils is about 1.5A; fuses with this value are placed in series with the motors, allowing brief higher currents as needed while blowing the fuse before overheating the motors. The actuators have torque constants of about 0.1 Nm/A, which yields 0.15Nm of torque at the maximum continuous current.

A.6. CONTROL SOFTWARE

The controller computer uses the Solaris-2.6-x86 operating system from Sun Microsystems, with a custom device driver that we developed to access the IP carrier board. Realtime extensions in this operating system allow us to run the control loop at the 1000Hz rate necessary to get high-fidelity haptic interaction. The haptic interaction software consists of about 8000 lines of *C* program code which controls the haptic device via

the device driver interface. The software also includes an OpenGL visual simulator of the simple haptic environment used in the experiments detailed in Chapter 5. This visual simulator was used for debugging purposes and was not made available to the test operators during experiments. Operating the haptic simulation software on this control computer essentially saturates two of the four available CPU's, leaving two more CPU's available for user interface, network I/O and other system maintenance tasks.

Data was collected during the experiments in a large in-memory buffer. At the completion of each trial, this data was written to disk in a file specific to both trial number and test operator. Offline processing was done on these files using a set of scripts written for this purpose in MATLAB. Most of the data plots in this document were generated with the MATLAB program.